Draft version August 14, 2026
Typeset using LaTeX twocolumn style in AASTeX7.0.1

arXiv:2608.12699v1 [astro-ph.GA] 13 Aug 2026

SPURS: Massive Stars, Dense Gas, and Lyα Escape in GN-z11 at $z = 10.6$

Zuyi Chen [1,2] Daniel P. Stark [3] Charlotte A. Mason [1,2] Peter Senchyna [4] Mengtao Tang [5,6,7] Keerthi Vasan G. C. [4] Lily Whitler [8,9] Adele Plat [10] and Viola Gelli [1,2]

[1] Cosmic Dawn Center (DAWN)
[2] Niels Bohr Institute, University of Copenhagen, Jagtvej 128, 2200 Copenhagen N, Denmark
[3] Department of Astronomy, University of California, Berkeley, Berkeley, CA 94720, USA
[4] The Observatories of the Carnegie Institution for Science, 813 Santa Barbara Street, Pasadena, CA 91101, USA
[5] Tsung-Dao Lee Institute, Shanghai Jiao Tong University, 1 Lisuo Road, Shanghai 201210, People's Republic of China
[6] School of Physics and Astronomy, Shanghai Jiao Tong University, 800 Dongchuan Road, Shanghai 200240, People's Republic of China
[7] State Key Laboratory of Dark Matter Physics, Shanghai Jiao Tong University, 1 Lisuo Road, Shanghai 201210, People's Republic of China
[8] Kavli Institute for Cosmology, University of Cambridge, Madingley Road, Cambridge, CB3 0HA, UK
[9] Cavendish Laboratory, University of Cambridge, JJ Thomson Avenue, Cambridge, CB3 0US, UK
[10] Institute of Physics, GalSpec Laboratory, Ecole Polytechnique Federale de Lausanne, Observatoire de Sauverny, Chemin Pegasi 51, 1290 Versoix, Switzerland

ABSTRACT

We present ultra-deep *JWST* spectroscopy of GN-z11 ($z = 10.6$) obtained through the SPURS Cycle 4 Large Program, providing the deepest rest-UV view yet obtained of a galaxy at $z > 10$. GN-z11 was previously found to be nitrogen-enhanced with detectable Lyα. The SPURS spectrum reveals P-Cygni stellar wind features and broad He II emission that are jointly reproduced by stellar population models incorporating very massive stars (VMS; $> 100\,M_\odot$) at low metallicity and young ages ($\lesssim 3$ Myr). We also detect a broad (FWHM = 1670 km s^{-1}) component to N IV] λ1486, now seen in several nitrogen emitters, potentially arising from dense WN winds or LBV-like outbursts associated with a population of VMS in a dense environment, though an AGN-driven wind cannot be excluded. In either scenario, this broad component may trace the gas producing GN-z11's nitrogen enhancement. Rest-UV absorption lines reveal a fast (~ 500 km s^{-1}), highly ionized outflow and a negligible neutral gas covering fraction. We resolve the weak Lyα emission (EW=5.6 Å, $f_{\rm esc,Ly\alpha} = 2.7\%$), finding a broad red wing (44% of flux at > 500 km s^{-1}) that should experience reduced IGM damping wing suppression and help explain Lyα visibility at $z > 10$. Fine-structure O I* λ1304 emission indicates dense neutral gas near a subset of the ionizing sources, which may also scatter Lyα to the large observed velocities. The weak low-ionization absorption favors a picture in which this dense neutral gas is confined to a compact nuclear region. Together, these results are consistent with a rapid burst of star formation building up the dense nuclear regions and surrounding clusters in GN-z11.

Keywords: Early universe (435) — Galaxy evolution (594) — Galaxy formation (595) — Massive stars (732) — High-redshift galaxies (734) — Reionization (1383)

1. INTRODUCTION

The launch of the *James Webb Space Telescope* (*JWST*; (J. P. Gardner et al. 2023; J. Rigby et al. 2023) has recently pushed the galaxy redshift frontier back beyond $z \simeq 14$ (see R. S. Ellis 2025; J. Matthee 2025; D. P. Stark et al. 2026 for a review). Prior to *JWST*, many expected the galaxy population at $z \gtrsim 10$ to be predominantly extremely faint, reflecting the redshift evolution seen in UV luminosity functions with the *Hubble Space Telescope* (*HST*) (e.g., R. J. Bouwens et al. 2015, 2021; S. L. Finkelstein et al. 2015; P. A. Oesch et al. 2018; R. A. A. Bowler et al. 2020). One of the biggest surprises from early *JWST* operations has been the discovery that very luminous galaxies ($M_{\rm UV} < -20$) remain abundant out to $z \simeq 14$ (e.g., M. Castellano et al. 2022; R. P. Naidu et al. 2022; N. J. Adams et al. 2023; S. L. Finkelstein et al. 2023; Y. Harikane et al. 2023a; C. T.

Email: zuyi.chen@nbi.ku.dk

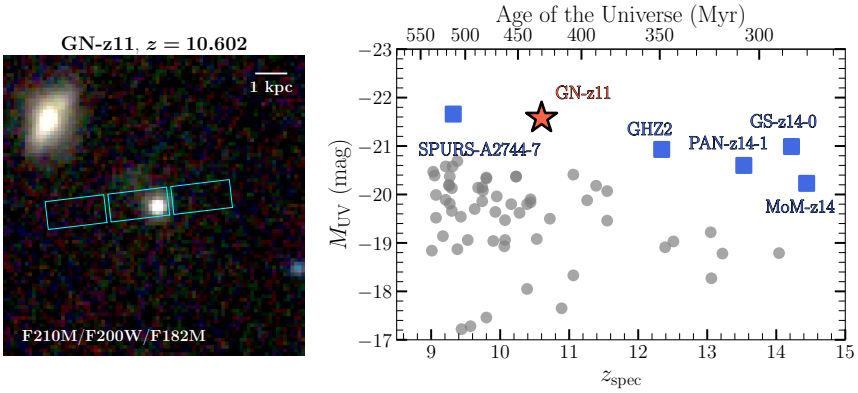

Figure 1. Left: NIRCam RGB image ($2''.5 \times 2''.5$) of GN-z11, with our SPURS NIRSpec shutter in cyan. A scale bar of 1 kpc is also shown. **Right**: UV absolute magnitude of GN-z11 compared to other spectroscopically confirmed galaxies at $z > 9$. We plot the NIRSpec sample compiled in M. Tang et al. (2025) as gray dots and highlight other notably luminous galaxies at these redshifts, including SPURS-A2744-7 (or Gz9p3; K. Boyett et al. 2024; Z. Chen et al. 2026), GHZ2 (M. Castellano et al. 2024), PAN-z14-1 (C. T. Donnan et al. 2026), GS-z14-0 (S. Carniani et al. 2024), and MoM-z14 (R. P. Naidu et al. 2026).

Donnan et al. 2024; B. Robertson et al. 2024; L. Whitler et al. 2025), with the current record holder now spectroscopically confirmed at $z = 14.4$ (R. P. Naidu et al. 2026).

The physics that makes galaxies so luminous at early epochs remains debated. Some argue star formation efficiencies are elevated in the low mass halos that come into view at $z \gtrsim 10$ (e.g., A. Dekel et al. 2023; Y. Qin et al. 2023; R. Feldmann et al. 2025; R. S. Somerville et al. 2025), while others suggest stochasticity in star formation histories adds considerable scatter in the UV luminosity at fixed halo mass, with burstiness enabling low mass halos to be luminous for short periods of time (e.g., C. A. Mason et al. 2023; J. Mirocha & S. R. Furlanetto 2023; X. Shen et al. 2023; A. Kravtsov & V. Belokurov 2024; V. Gelli et al. 2024). Additionally, if dust is preferentially ejected from early galaxies (i.e., due to their large specific star formation rates), the emergent UV luminosities will be further boosted (e.g., A. Ferrara et al. 2025). Finally, the UV output may be further enhanced by a population of early AGN or the presence of top-heavy initial mass functions (e.g., S. Chon et al. 2022; Y. Harikane et al. 2023b; C. L. Steinhardt et al. 2023; S. Hegde et al. 2024; E. M. Ventura et al. 2024; A. Hutter et al. 2025).

Attention is now turning to detailed investigations of the galaxies discovered at these redshifts. One of the first deep $z \gtrsim 10$ galaxy spectra was of GN-z11 (P. A. Oesch et al. 2016), a compact (half-light radius $= 64 \pm 20$ pc; S. Tacchella et al. 2023) UV luminous ($M_{UV} = -21.6$) system at $z = 10.6$, observed for 6.9 hours in the prism and 3.45 hours in each of G140M/F070LP, G235M/F170LP, and G395M/F290LP grating/filter combinations (A. J. Bunker et al. 2023). The GN-z11 spectrum revealed numerous emission lines throughout the rest-UV and rest-optical. Lyα emission was detected, potentially suggesting GN-z11 sits in an early ionized region. The detection of both N III] and N IV] pointed to a nitrogen-enhanced abundance pattern that is similar to globular cluster stars (e.g., A. J. Cameron et al. 2023; P. Senchyna et al. 2024). High ionization lines are detected, revealing the presence of hard ionizing sources, and the various density-sensitive ratios reveal that GN-z11 contains high density gas ($> 10^5$ cm^{-3}; P. Senchyna et al. 2024; R. Maiolino et al. 2024) not often seen in lower redshift galaxies. MIRI MRS spectroscopy has identified narrow emission from [O III] and Hα in the rest-frame optical (J. Álvarez-Márquez et al. 2025), and NIRSpec/IFU observations reveal tentative indications of rotation (Y. Xu et al. 2024). The emission line ratios from NIRSpec and MIRI point to low metallicity gas ($0.13 - 0.17\ Z_\odot$; A. J. Cameron et al. 2023; J. Álvarez-Márquez et al. 2025), suggesting GN-z11 may be a compact starburst in a metal poor galaxy.

However, the nature of GN-z11 remains debated. R. Maiolino et al. (2024) have argued GN-z11 is likely an AGN based on very high ionization nebular emission, fast outflows, and very high gas densities. Additional evidence in favor of an AGN interpretation for GN-z11 was presented in X. Ji et al. (2025). They find a continuum excess at rest-frame $3000 - 3550$ Å in the NIRSpec prism spectrum, potentially corresponding to the small blue bump often seen in lower redshift quasar spectra. On the other hand, an AGN is not required to explain the narrow emission line ratios, and MIRI/MRS spectroscopy reveals that Hα is narrow (albeit not ruling out a fainter broad contribution) (e.g., J. Álvarez-Márquez et al. 2025). MIRI imaging has recently extended the GN-z11 SED to 10 μm (A. Crespo Gómez et al. 2026).

The shape of the rest-optical SED does not support the presence of a Type I AGN, but it does reveal excess emission at rest-frame wavelengths of $6600-8600$ Å, potentially corresponding to hot dust emission that could either be from a Type II AGN or a compact starburst (A. Crespo Gómez et al. 2026). Without deeper spectroscopy, the role of an AGN in establishing the spectral characteristics of GN-z11 remains unsettled.

Since the discovery of GN-z11, other nitrogen-enhanced spectra with hard radiation fields and high density ionized gas have been found at $z \gtrsim 10$ (M. Castellano et al. 2024; R. P. Naidu et al. 2026), suggesting that GN-z11 may be representative of a phase in early galaxy evolution. On the other hand, only one further galaxy at $z \gtrsim 10$ has been found with Lyα emission (GS-z13-1-LA at $z = 13.1$, J. Witstok et al. 2025, 2026). Whether GN-z11 and GS-z13-1-LA have unique physical conditions that facilitate Lyα escape in a highly neutral IGM is not known. Owing to its brightness, GN-z11 is one of the best galaxies for answering questions related to nitrogen enhancements and Lyα transfer through the early IGM. However, current data are not up to either task. The existing rest-UV spectrum of GN-z11 lacks the sensitivity to robustly characterize the stellar wind features (e.g., broad He II, N V, C IV) that would directly identify the massive star population driving its extreme nitrogen enhancement. Similarly, characterizing the gas-phase conditions that permit Lyα escape requires substantially higher signal-to-noise than presently available. A deep rest-UV spectrum reaching sufficient signal-to-noise and resolution is therefore essential to move toward a physical characterization of the detailed nature of GN-z11.

In this paper, we present new observations of GN-z11 obtained as part of the SPURS Large Program in Cycle 4 of *JWST* operations (GO 9214, PIs C. Mason and D. Stark, Z. Chen et al. 2026). The SPURS data deliver the first ultra-deep view of the rest-frame UV spectrum of GN-z11, providing new insights into the massive stars, ISM conditions, and Lyα profile, while also delivering new constraints on the role of an AGN in driving its spectroscopic properties. We note that an independent analysis of the SPURS spectrum of GN-z11 is presented in Nakane et al. 2026. The paper is organized as follows. In § 2, we describe the new SPURS observations and our measurements of the emission lines in the NIRSpec spectrum. We then characterize the rest-frame UV and optical emission lines of GN-z11 in § 3 and place constraints on the interstellar absorption lines in § 4. The physical properties inferred from the emission lines are presented in § 5. We model the stellar continuum of the far-UV spectrum in § 6. We discuss the implications for the physical nature of GN-z11 in § 7 and summarize our conclusions in § 8. Throughout this paper, we adopt a flat ΛCDM cosmology with $H_0 = 70$ km s^{-1} Mpc^{-1}, $\Omega_{\rm m} = 0.3$, and $\Omega_\Lambda = 0.7$. All magnitudes are measured in the AB system (J. B. Oke & J. E. Gunn 1983). The line equivalent widths are calculated in the rest frame, with positive values corresponding to emission lines and negative values to absorption lines.

2. OBSERVATIONS AND ANALYSIS

2.1. *SPURS Spectroscopy*

Here we present new spectra of GN-z11 obtained as part of the SPURS program. The full description of the SPURS observations will be presented in a future paper, and we briefly summarize the relevant observations and spectra. GN-z11 was observed in the SPURS GOODS-N pointing taken over May 12–14, 2026. Data were acquired in a single pointing using the Multi-Object Spectroscopy (MOS) mode (aperture position angle PA = 276.5°), adopting the standard three-shutter nodding pattern. We use three grating/filter pairs at medium resolution ($R \sim 1000$): G140M/F100LP, G235M/F170LP, and G395M/F290LP, with integration times of 29.18, 7.90, and 2.92 hours in each grating, respectively. In Figure 1, we show the NIRCam image of GN-z11, overlaid with the NIRSpec shutter position of our SPURS observation.

We reduce the spectra using the `msaexp`[11] package (`v0.9.14`; G. Brammer 2023), based on the official *JWST* pipeline version 1.16.1 and reference file mapping `jwst_1464.pmap`, following the same procedures described in Z. Chen et al. (2026) (also see A. de Graaff et al. 2025; K. E. Heintz et al. 2025; F. Valentino et al. 2025). Briefly, we obtain the stage-1 data products (`*_rate.fits`) of the standard *JWST* pipeline from the MAST archive, and subsequently use `msaexp` to apply $1/f$ correction and read noise array scaling based on empty regions of each image. The resulting files are then processed through the stage-2 pipeline to assign the world coordinate system, flag open microshutters, cut out individual 2D spectra from each exposure of every source, apply flat-field correction, correct for vignetting of the MSA bars, and apply the absolute photometric calibration. For each source, we subtract the background using the difference spectra taken at the three nod offset positions. We then rectify and combine individual background-subtracted 2D cutouts on a common wavelength grid to produce the final 2D spectrum of each source. The final 1D spectra used in our

[11] https://github.com/gbrammer/msaexp/

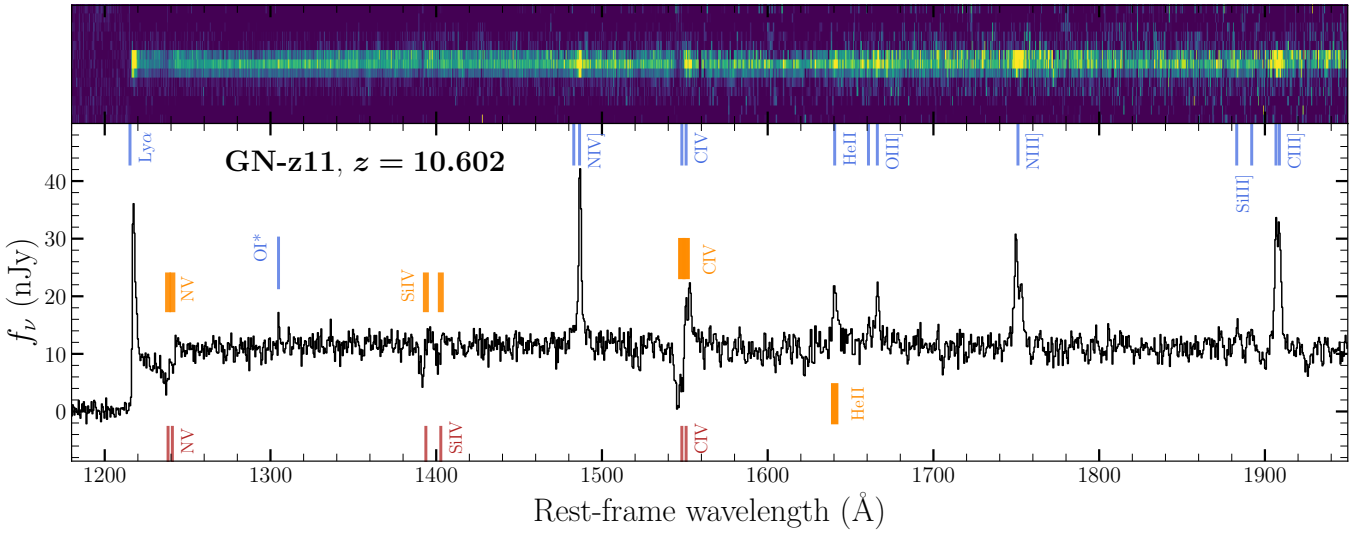

Figure 2. Rest-frame far-UV (1180 – 1950 Å) spectrum of GN-z11. The main panel shows the final 1D spectrum used in this work, created by stacking the SPURS and JADES observations. The top panel shows the 2D spectrum from the SPURS observations, which dominate the total exposure time. We mark the detected emission lines with blue vertical lines. The interstellar absorption lines and stellar wind features are highlighted by red and orange vertical lines, respectively.

analysis are extracted using a boxcar aperture with the extraction window chosen to match the spatial profile of each source. Throughout this reduction, we utilize the extended wavelength extraction available as part of `msaexp` (F. Valentino et al. 2025) to achieve coverage beyond the nominal limits of each grating by extracting the full wavelength range covered by the detector, which is based on the extended flats and photometric calibration derived by `msaexp`. While this extended wavelength coverage is susceptible to second-order spectral contamination, in our analysis below, we will exclude the affected spectral regions from our continuum measurements but will consider them for emission line measurements. We assume a point source pathloss correction, consistent with the compact morphology seen from the NIRCam images of GN-z11.

To maximize the signal-to-noise ratio, we create a composite spectrum for GN-z11 by stacking the SPURS and JADES $R \sim 1000$ grating spectra (A. J. Bunker et al. 2023; R. Maiolino et al. 2024). We utilize the JADES G140M/F070LP, G235M/F170LP, and G395M/F290LP spectra taken by the program GTO 1181 (PI: D. Eisenstein) and released by the DAWN *JWST* Archive[12] (DJA; G. Brammer 2023; A. de Graaff et al. 2024; K. E. Heintz et al. 2025), which were also reduced using the `msaexp` package with the same procedures described above by the DJA team. Before stacking, for each spectrum, we first make sure the error spectrum matches the observed continuum fluctuation, derived as the standard deviations in bins of 20 pixels, similar to the approach adopted in previous works (e.g., P. Senchyna et al. 2022; A. de Graaff et al. 2025). We model the resulting ratio as a function of wavelength with an iteratively fit, outlier-rejected third-order polynomial, which we then apply as a multiplicative correction to the error spectrum. We then coadd individual SPURS and JADES spectra with inverse variance weighting (i.e., weighted by $1/\sigma^2$ where σ is the error spectrum of the individual spectra). This adds an additional 5.96 hours to each grating, leading to total integration times of 35.14, 13.86, and 8.88 hours in G140M, G235M, and G395M, respectively. Finally, we recalibrate the absolute flux of the coadded spectrum to match that of NIRCam by applying a second-order polynomial correction factor as a function of wavelength. We derive this correction by fitting the ratio of the NIRCam photometry, where we adopt the CIRC1 photometry available from the JADES DR5 photometric catalog (B. E. Robertson et al. 2026), to that synthesized from the coadded spectrum in broad NIRCam filters (from F150W to F444W). In what follows, we will primarily use this final spectrum for our analysis, but we will also separately examine the low-SNR emission lines in the SPURS spectrum alone for comparison with JADES. As shown in A. J. Bunker et al. (2023), the JADES spectrum extracted with the 3-pixel (0″.3) window also matches the NIRCam CIRC1 photometry, so our comparison will primarily focus on their values based on the 3-pixel extraction.

[12] https://dawn-cph.github.io/dja/

Figure 2 presents the far-UV spectrum of GN-z11, using the redshift determined in § 2.2. The continuum is well detected in the combined G140M grating spectrum, with an SNR of 8.5 per pixel (corresponding to 6 Å) at the observed-frame wavelength of 1.5 μm, significantly higher than what was achieved with the earlier JADES spectrum alone (SNR = 2.6 per pixel). The typical 3σ emission line flux limit is 8.1×10^{-20} erg s^{-1} cm^{-2}, assuming an integration window of 600 km s^{-1} ($\sim$ 2 resolution elements). This translates to a 3σ rest-frame line EW limit of 0.4 Å in GN-z11 at rest-frame 1400 Å. We estimate typical 3σ line flux limits of 7.8×10^{-20} erg s^{-1} cm^{-2} in G235M and 7.6×10^{-20} erg s^{-1} cm^{-2} in G395M, corresponding to EW limits of 1.2 Å in G235M and 3.4 Å in G395M for GN-z11.

2.2. *Emission Line Measurements*

We first derive the systemic redshift by simultaneously fitting the centroids of the available strong narrow rest-frame optical emission lines. Since the strong optical lines (Hβ, [O III]) are shifted out of the NIRSpec spectrum, we utilize the [Ne III] λ3869 and Hδ emission lines. The derived systemic redshift ($z_{\rm sys} = 10.6016$) is consistent with the redshift reported in A. J. Bunker et al. (2023).

Emission lines are characterized as follows. For well-detected lines (S/N $>$ 5), we measure the line flux, centroid, width, and EW by fitting the line profile and nearby continuum with a Gaussian function. For each line, we visually examine whether there are broad wings that are not captured by our derived profile. We report the small number of lines where this is the case in Section § 3. For emission lines that are close in wavelength or that show complex profiles, we fit with multiple Gaussians simultaneously. We will describe measurements for these lines in more detail in § 3. If an emission line is detected with lower S/N ($<$ 5), we compute the line flux using direct integration. Finally, the uncertainties of line fluxes, widths, and EWs are evaluated as follows. We resample the flux densities of each spectrum 1000 times by taking the observed value as the mean and the error as the standard deviation. Then we compute the line fluxes, widths, and EWs from the resampled spectra of each source using the same approach described above. We take the standard deviation of these measurements as the uncertainty. When fitting broad emission lines, we convolve the Gaussian models with the instrument resolution ($R = 1000$, corresponding to 300 km s^{-1}). We obtain consistent results if we adopt the wavelength-dependent line spread function from the JDox, rescaled by a factor of 1.3 to match in-flight estimates of the resolution (Y. Isobe et al. 2023; A. de Graaff et al. 2024; A. J. Shajib et al. 2025).

Table 1. Rest-frame far-UV emission line observed-frame wavelengths (Å), fluxes (10^{-19} erg s^{-1} cm^{-2}), EWs (Å), and observed FWHMs (km s^{-1}) of GN-z11. Upper limits are provided at the 3σ level.

Line	$\lambda_{\rm obs}$	Flux	EW	FWHM
Ly$\alpha_{\rm t}$	14120.5	$12.8^{+0.4}_{-0.3}$	$5.6^{+0.2}_{-0.2}$	–
Ly$\alpha_{\rm n}$	14120.4	$5.1^{+2.3}_{-2.5}$	$2.3^{+0.8}_{-0.7}$	315^{+9}_{-20}
Ly$\alpha_{\rm b}$	14126.9	$7.9^{+2.2}_{-2.7}$	$3.2^{+0.7}_{-0.9}$	592^{+78}_{-79}
N V λ1240[a]	14440.3	$1.9^{+0.3}_{-0.3}$	$1.0^{+0.2}_{-0.2}$	754^{+253}_{-253}
O I* λ1304	15140.8	$1.0^{+0.3}_{-0.2}$	$0.5^{+0.2}_{-0.1}$	< 300
N IV]$_{\rm t}$	–	$12.2^{+0.6}_{-0.6}$	$7.9^{+0.4}_{-0.4}$	–
[N IV] $\lambda1483_{\rm n}$	–	< 0.8	< 0.5	–
N IV] $\lambda1486_{\rm n}$	17248.8	$6.3^{+0.6}_{-0.6}$	$4.0^{+0.4}_{-0.4}$	319^{+24}_{-24}
[N IV] $\lambda1483_{\rm b}$	–	< 2.0	< 1.3	–
N IV] $\lambda1486_{\rm b}$	17248.8	$6.0^{+1.8}_{-1.8}$	$3.8^{+1.1}_{-1.1}$	1670^{+292}_{-292}[b]
C IV$_{\rm t}$	–	$4.5^{+0.5}_{-0.5}$	$3.3^{+0.3}_{-0.3}$	–
C IV λ1548	17990.1	$1.8^{+0.3}_{-0.3}$	$1.3^{+0.2}_{-0.2}$	347^{+31}_{-31}
C IV λ1550	18020.3	$2.8^{+0.4}_{-0.4}$	$2.0^{+0.3}_{-0.3}$	347^{+31}_{-31}
He II λ1640	19033.6	$4.1^{+0.7}_{-0.8}$	$3.3^{+0.6}_{-0.7}$	671^{+175}_{-178}
O III] λ1661	19269.3	$0.8^{+0.2}_{-0.2}$	$0.6^{+0.2}_{-0.2}$	386^{+45}_{-45}
O III] λ1666	19331.9	$2.4^{+0.4}_{-0.4}$	$1.9^{+0.3}_{-0.3}$	386^{+45}_{-45}
N III]$_{\rm t}$	–	$7.9^{+0.5}_{-0.5}$	$7.3^{+0.4}_{-0.4}$	–
N III] λ1746	20269.2	$0.3^{+0.0}_{-0.0}$	$0.3^{+0.0}_{-0.0}$	347^{+22}_{-22}
N III] λ1748	20290.0	$0.8^{+0.2}_{-0.2}$	$0.8^{+0.2}_{-0.2}$	347^{+22}_{-22}
N III] λ1750	20302.8	$3.7^{+0.3}_{-0.3}$	$3.4^{+0.3}_{-0.3}$	347^{+22}_{-22}
N III] λ1752	20331.8	$2.2^{+0.3}_{-0.3}$	$2.0^{+0.3}_{-0.3}$	347^{+22}_{-22}
N III] λ1754	20352.7	$0.9^{+0.2}_{-0.2}$	$0.8^{+0.2}_{-0.2}$	347^{+22}_{-22}
Si III] λ1883	21843.1	$1.0^{+0.3}_{-0.3}$	$1.1^{+0.4}_{-0.4}$	413^{+116}_{-116}
Si III] λ1892	21951.0	$0.7^{+0.3}_{-0.3}$	$0.8^{+0.3}_{-0.3}$	413^{+116}_{-116}
C III]$_{\rm t}$	–	$7.9^{+0.5}_{-0.5}$	$8.8^{+0.4}_{-0.4}$	–
[C III] λ1907	22121.5	$3.8^{+0.4}_{-0.4}$	$4.3^{+0.5}_{-0.5}$	442^{+32}_{-32}
C III] λ1909	22144.7	$4.0^{+0.4}_{-0.4}$	$4.5^{+0.5}_{-0.5}$	442^{+32}_{-32}

Note—Lines with subscript 't' show the total fluxes and EWs of multiple components. Lines with subscript 'n' and 'b' show the narrow and broad components, respectively.

[a] Unresolved N V $\lambda\lambda$1238, 1242 emission.

[b] Intrinsic FWHM for broad N IV] corrected for instrument resolution assuming $R = 1000$.

3. SPECTROSCOPIC MEASUREMENTS

3.1. *Lyα Emission*

GN-z11 is one of only two galaxies above $z \simeq 10$ detected with Lyα emission (see also J. Witstok et al. 2025). The line was first identified in the JADES dis-

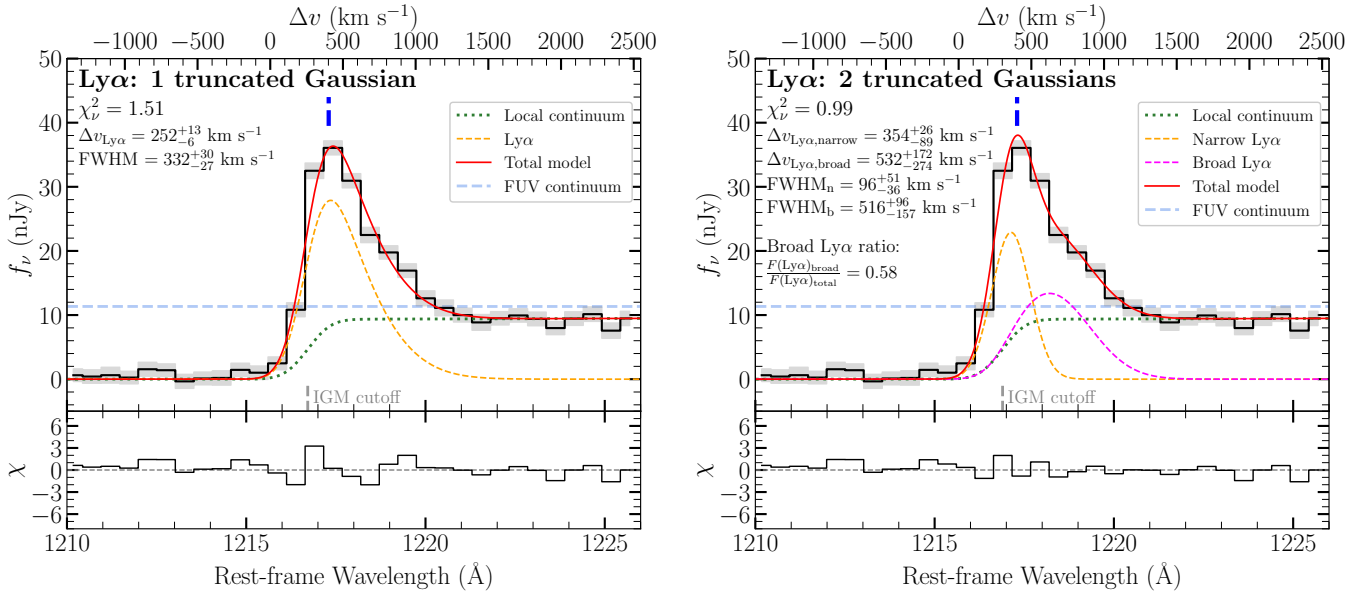

Figure 3. Lyα of GN-z11 with best-fit model (red) to the line profile (black). We present both the fit assuming a single truncated Gaussian (left panel) and that assuming a double truncated Gaussian (right panel). In both cases, we additionally include a constant component as the continuum. Both the continuum and the line profile (single or double Gaussians) are truncated at the same IGM cutoff velocity, which is a free parameter in our fit. We plot the model convolved with instrument resolution for each truncated Gaussian (orange and magenta dashed lines) as well as for the continuum (green dotted line). We also plot the continuum extrapolated from our fit over $1300 - 1600$ Å (light blue dashed lines), which we use for our EW estimate. In each fit, we also plot the residual of the observed spectrum subtracted by the best-fit model. The residual is shown by $\chi \equiv (f - m)/\sigma$, where f is the observed flux density, m is the best-fit model, and σ is the uncertainty. We also show the peak velocity offset and FWHM derived from our intrinsic model (i.e., before convolving with the instrument resolution) in each panel.

covery spectrum (A. J. Bunker et al. 2023) and subsequently observed with NIRSpec IFU (J. Scholtz et al. 2024). With the new SPURS observations, we recover Lyα with improved significance (S/N=24), enabling better characterization of the line properties. The observed Lyα profile (Figure 3) is asymmetric, reaches peak intensity at 418^{+12}_{-14} km s^{-1} redward of the systemic velocity (uncertainties estimated by resampling the flux densities based on the error spectrum 1000 times), and shows both a narrow core and a broad red wing. Asymmetric and redshifted Lyα lines are commonly seen in $z \gtrsim 5$ galaxies due to resonant scattering by neutral hydrogen in the ISM and IGM (e.g., L. Pentericci et al. 2018; M. J. Hayes et al. 2021; M. Tang et al. 2024b; G. Prieto-Lyon et al. 2025). However, given the $R \approx 1000$ resolution of the G140M spectrum, the observed peak velocity may overestimate the intrinsic velocity offset of Lyα from systemic (as has been noted in sources with both G140H and G140M Lyα spectroscopy, L. Whitler et al. 2026).

To characterize the line properties, we thus consider fits to the spectrum with a truncated Gaussian, which we convolve to the instrument resolution, following the approach in previous works (e.g., R. Endsley & D. P. Stark 2022; M. Tang et al. 2026). In our fits, we truncate the emission below a velocity of $v_{\rm cutoff}$ (a free parameter) and we assume a fixed continuum level redwards of the cutoff velocity, using the median flux just redward of the emission line ([1222, 1226] Å, 1.89×10^{-19} erg s^{-1} cm^{-2} Å^{-1}). We fit over the rest-frame wavelength window of [1212, 1226] Å, corresponding to [−1000, 2500] km s^{-1} relative to the systemic wavelength of Lyα. The free parameters are thus the amplitude, centroid, and width of the Gaussian component, as well as the cutoff velocity.

We show the resulting Lyα model, convolved to the instrument resolution, in Figure 3. The truncated Gaussian profile (left panel) reproduces the peak and the extended red wing of the observed Lyα emission ($\chi^2_{\nu,\rm single} = 1.5$). The model profile reaches its intrinsic peak intensity at a redshifted velocity of $v_{\rm peak} = 252^{+13}_{-6}$ km s^{-1}, significantly lower than its value once convolved with the instrumental resolution (417^{+1}_{-6} km s^{-1}). The intrinsic FWHM of the model profile is 312^{+29}_{-25} km s^{-1}, or 511^{+17}_{-17} km s^{-1} including the instrumental resolution. We find the asymmetric profile is fit with a truncation velocity of $v_{\rm cutoff} = 250^{+8}_{-9}$ km s^{-1}, comparable to the velocity offset. One interpretation of such a high truncation velocity is resonant scatter-

ing by neutral hydrogen from IGM gas infalling towards the galaxy, which should produce a sharp cut-off on the blue side of the line (predicted at velocities around $100-300$ km s^{-1} M. R. Santos 2004; C. A. Mason et al. 2018a; H. Park et al. 2021), though it may also reflect resonant scattering in the ISM (e.g., D. A. Neufeld 1990; A. Verhamme et al. 2006, 2008). A higher resolution spectrum should be able to better resolve a sharp cut-off due to IGM resonant scattering. Integrating the line profile, we measure a total Lyα flux of $1.28^{+0.04}_{-0.03}\times10^{-18}$ erg s^{-1} cm^{-2}. Importantly, we find that 44% of the line flux arises from very large velocities (>500 km s^{-1} relative to line center), where this number is computed from the intrinsic profile, before convolution with the instrumental profile.

Given the very high SNR of the SPURS spectrum, we are now able to better resolve the asymmetric profile of Lyα. This results in some differences in our inferred line properties relative to those reported from the earlier JADES spectrum by A. J. Bunker et al. (2023) and J. Scholtz et al. (2024), which we will now describe. The *observed* line profile peaks at a velocity consistent with the shallower JADES spectrum (≈ 420 km s^{-1} A. J. Bunker et al. 2023), and has a consistent observed linewidth (FWHM$= 511^{+17}_{-17}$ km s^{-1}, relative to 566 ± 61 km s^{-1} in the JADES spectrum). However, estimates of the *intrinsic* velocity offset and FWHM are sensitive to the shape of the line profile. Based on our truncated Gaussian fits we recover a lower deconvolved peak velocity offset ($v_{\rm peak}=252^{+13}_{-6}$ km s^{-1}) and FWHM (312^{+29}_{-25} km s^{-1}) than reported by A. J. Bunker et al. (2023) ($v_{\rm peak}=520$–555 km s^{-1}, FWHM $=530\pm65$ km s^{-1} accounting for the resolution). We attribute these differences primarily to the assumed line profiles. A. J. Bunker et al. (2023) found a single full (i.e. not truncated) Gaussian profile, without continuum, was a good fit to the Lyα profile in the JADES spectrum. Fitting the SPURS spectrum with a full Gaussian produces much closer agreement with the results of A. J. Bunker et al. (2023): a full Gaussian fit shifts the inferred peak to higher velocities and requires a broader line profile, relative to our truncated Gaussian model (Figure 3), to fit the asymmetric profile (and continuum at $\approx 1220-1225$Å). However, we find that the full Gaussian fits to the SPURS spectrum are substantially worse ($\chi^2_\nu>3$) than the truncated Gaussian ($\chi^2_\nu=1.5$), as expected given the asymmetry of the line. A smaller contribution to the difference in intrinsic FWHM comes from the assumed instrumental resolution: A. J. Bunker et al. (2023) adopted $R\approx1500$, whereas we adopt $R=1000$ (see Section 2.2), which slightly increases our intrinsic FWHM measurement relative to their reported value. Our results indicate that accounting for asymmetric lineshapes is important for interpreting Lyα in G140M spectra. Ultimately, a G140H spectrum would provide the most precise estimate of the Lyα velocity offset in GN-z11.

We measure the Lyα EW, which is a well-established tracer for neutral hydrogen in the reionizing IGM (e.g., D. P. Stark et al. 2010, 2011; T. Treu et al. 2012; L. Pentericci et al. 2014; C. A. Mason et al. 2018a). Our goal is to characterize how the ratio of Lyα flux relative to the FUV continuum evolves with redshift, as the Lyα damping wing due to neutral hydrogen in the IGM can significantly depress both Lyα emission and the continuum redwards of Lyα, out to ~1300 Å (e.g., C. A. Mason et al. 2026). Thus, to measure the EW, we compute the continuum by fitting a power law ($f_\lambda\propto\lambda^\beta$) to the observed UV continuum over the rest-frame range 1300–1800 Å, masking regions affected by any emission and absorption features (described in the Sections below). This range also avoids the strong N V P-Cygni absorption and emission at wavelengths 1226–1240 Å seen in Figure 2 and described below in Section 3.6. We extrapolate from the fit to derive the continuum at the Lyα wavelength ($2.30\pm0.02\times10^{-19}$ erg s^{-1} cm^{-2} Å^{-1}), yielding an integrated EW of $5.6^{+0.2}_{-0.2}$ Å. We note that this value is lower than that reported by A. J. Bunker et al. (2023), which is 12 Å, assuming their line flux determined from the 3-pixel, or $0''.3$, extraction aperture. As our line flux measurement is only slightly smaller than their value from 3-pixel extraction, we attribute the higher EW reported by A. J. Bunker et al. (2023) primarily to differences in the adopted continuum estimate. A. J. Bunker et al. (2023) estimate the continuum directly at the Lyα wavelength (priv. comm.) from the JADES prism spectrum, where the lower spectral resolution blends the continuum with both the Lyα break and the N V P-Cygni absorption (e.g., L. C. Keating et al. 2024; C. A. Mason et al. 2026), resulting in a lower observed continuum value relative to our estimate from the high SNR grating spectrum. Such a low Lyα EW is $\approx3-4\times$ smaller than the median EW in Lyman-break galaxies at $z\sim5-6$ (M. Tang et al. 2024b; G. Prieto-Lyon et al. 2025), but comparable values have been reported in similarly UV luminous galaxies at slightly lower redshifts ($z\simeq8$–9; e.g., L. Whitler et al. 2026), and may suggest significant IGM attenuation (M. Tang et al. 2024a; Y. Kageura et al. 2025). We return to the effect of the IGM in § 6.3, where we independently model its effect as part of the full UV continuum spectrum fitting.

Finally, motivated by the high fraction of flux at >500 km s^{-1}, we also consider whether the Lyα emis-

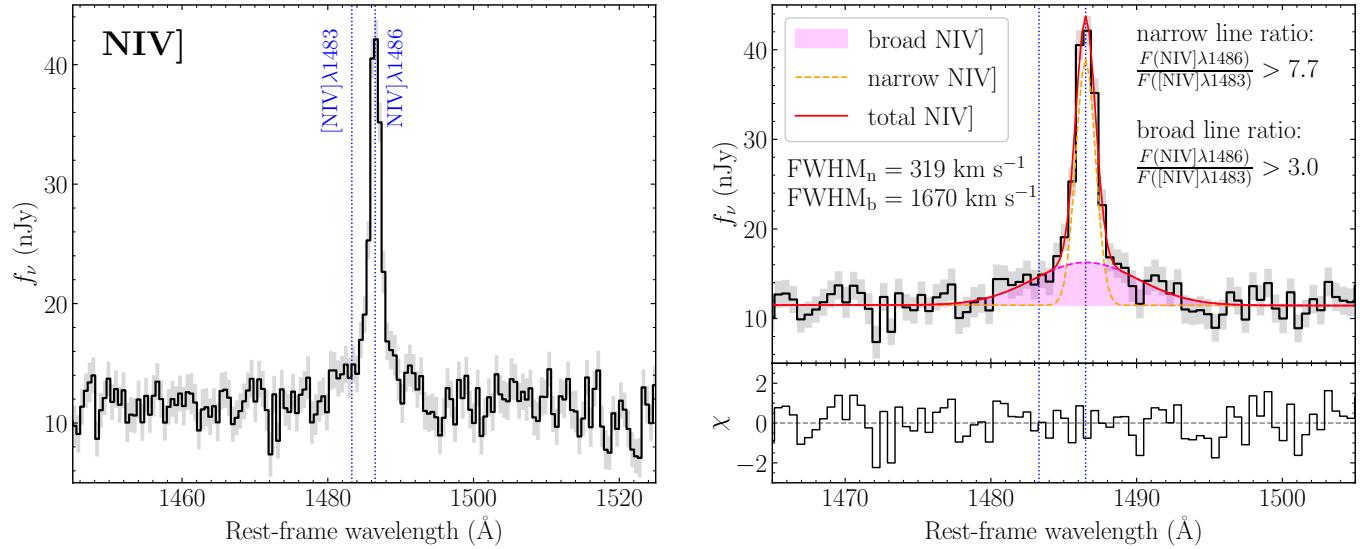

Figure 4. Left panel: N IV] emission line of GN-z11. Right panel: Fits to the N IV] profile. Rest-frame wavelength of each individual component of N IV] is marked by blue dotted line. The N IV] profile is best-fitted by a narrow (FWHM = 319 km s^{-1}; orange dashed line) and a broad (FWHM = 1670 km s^{-1}; magenta shaded region) N IV]λ1486 component, while the [N IV]λ1483 component remains undetected. The red curves show the sum of fits to individual components. In the right panel, we also plot the residual of the observed spectrum subtracted by the best-fit model (χ).

sion can be better fit including a broad component, to help establish the potential presence of outflows and/or an AGN broad line region which may broaden Lyα without significant resonant scattering. We thus also fit the Lyα profile with a double-truncated Gaussian model, which we present in the right panel of Figure 3. We find the double-truncated Gaussian model provides a slightly better fit to the data compared to the single-truncated Gaussian model, as it better reproduces the core of the line $\approx 200 - 400$ km s and the red tail at $\approx 800 - 1000$ km s, as seen in the residuals in Figure 3 ($\chi^2_{\nu,\mathrm{double}} = 1.0$ compared to $\chi^2_{\nu,\mathrm{single}} = 1.5$ at rest-frame wavelengths 1215–1220 Å). In the double-truncated Gaussian, the narrow core is peaked at $v_{\mathrm{peak,narrow}} = 360^{+26}_{-45}$ km s^{-1} with intrinsic FWHM $= 95^{+60}_{-28}$ km s^{-1}, while the broad wing is more redshifted ($v_{\mathrm{peak,broad}} = 538^{+165}_{-255}$ km s^{-1}), with intrinsic FWHM $= 526^{+98}_{-155}$ km s^{-1}. We note the total Lyα flux ($1.30^{+0.05}_{-0.06} \times 10^{-18}$ erg s^{-1} cm^{-2}) and large fraction (40%) of flux at > 500 km s^{-1} are unchanged relative to the single truncated Gaussian model, and these results are unchanged if we fix the broad component centroid to that of the narrow peak. We will discuss the implications of a potential broad component in Lyα in more detail in Section 7.

3.2. *N IV] Emission*

The next strongest emission line in the rest-UV is the N IV]$\lambda\lambda$1483,1486 doublet (Fig. 4). Emission from the red component of N IV] (λ1486) was detected by A. J. Bunker et al. (2023), and it was pointed out that the line ratios of the doublet (i.e., the absence of λ1483 emission) imply that the nitrogen-emitting gas is very high density ($\gtrsim 10^5$ cm^{-3}) (P. Senchyna et al. 2024; R. Maiolino et al. 2024). The SPURS measurements reveal a strong λ1486 line but do not unambiguously detect the λ1483 component. One of the key findings of the deeper spectrum is the potential detection of a broad N IV] component, which visually appears centered on the red side of the doublet (see Fig. 4).

We fit the N IV] complex with a number of model profiles. We first consider only two narrow lines, then we add in one and two broad components. The results are described in Appendix A. This investigation shows that fits including two narrow components and a broad component are preferred to those including only two narrow components. Our main results are not strongly dependent on the chosen profile, but we will adopt the model that allows two narrow lines (centered on λ1483 and λ1486) and a broad line (centered on λ1486). Additional information about the fitting process is provided in Appendix A.

The N IV] fit is shown in the right panel of Figure 4, and the line measurements are listed in Table 1. The narrow lines are found with a FWHM of 319^{+24}_{-24} km s^{-1}, similar to that found in other nebular emission lines in GN-z11. The broad line is fit with a FWHM of 1670^{+292}_{-292} km s^{-1}, implying a fast-moving nitrogen-emitting component in GN-z11. The narrow N IV]λ1486 line is very strong (S/N = 10, EW = $4.0^{+0.4}_{-0.4}$ Å). We

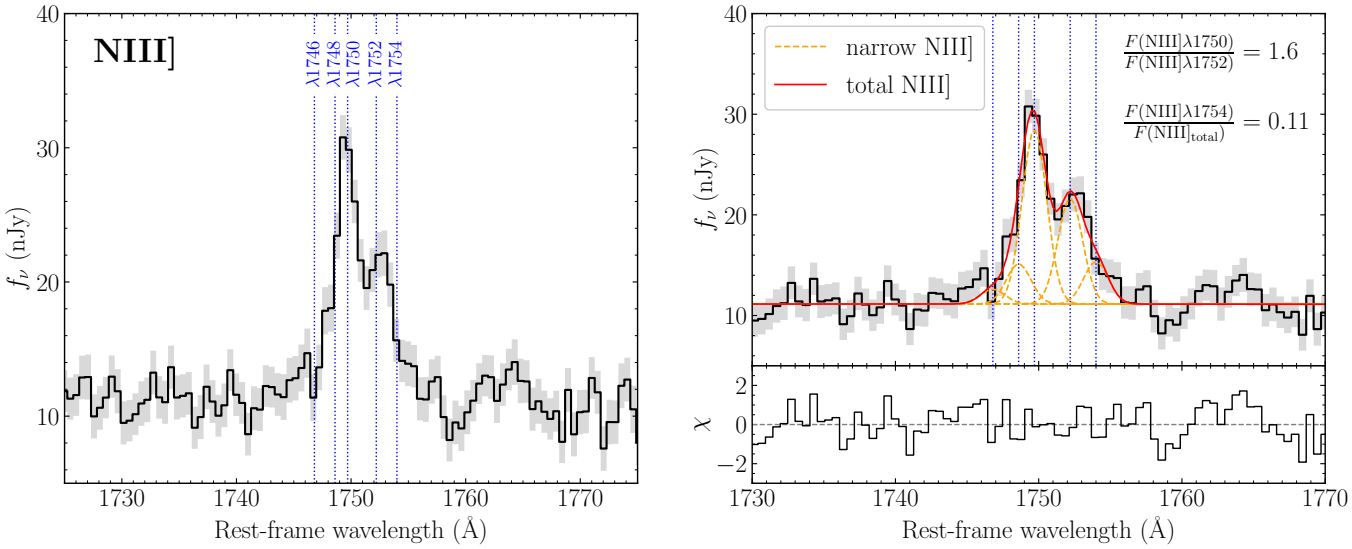

Figure 5. Left panel: N III] emission line of GN-z11. Right panel: Fits to the N III] profile of GN-z11. The figure is shown in the same way as Figure 4. The N III] profile is best-fitted by five narrow (FWHM = 347 km s^{-1}; orange dashed line) Gaussians without a broad component.

place an upper limit on the narrow [N IV]λ1483 flux, indicating a large N IV]λ1486/[N IV]λ1483 flux ratio ($>$ 7.7 at 3σ). The broad N IV] component (S/N = 3, EW = $3.8^{+1.1}_{-1.1}$ Å) comprises 49% of the total N IV] flux, corresponding to a luminosity of $8.8^{+2.6}_{-2.6} \times 10^{41}$ erg s^{-1}. The absence of a broad component centered at [N IV]λ1483 suggests an N IV]λ1486/[N IV]λ1483 ratio of $>$ 3.0 in the broad line emitting region.

One potential explanation of the broad N IV]λ1486 component is fast-moving gas associated with stellar winds. The most prominent N IV] wind line in Wolf-Rayet stars is typically N IV]λ1719 (e.g. R. Hainich et al. 2014), so if the broad N IV]λ1486 line is powered by stellar winds, we should expect to see even stronger broad N IV]λ1719 emission. However, the SPURS observations do not detect any emission at the wavelength of N IV]λ1719 (Fig. 2). Assuming a line width the same as the broad N IV] λ1486 (FWHM = 1670 km s^{-1}), we place a 3σ limiting flux of $< 1.6 \times 10^{-19}$ erg s^{-1} cm^{-2}, corresponding to a broad N IV]λ1486/N IV]λ1719 flux ratio of $>$ 3.7. We thus conclude that the stellar winds typically seen in WR stars of the local universe are unlikely to be responsible for the broad N IV]λ1486 emission, but we will discuss in §7.2 that this could be nevertheless produced in a dense WR-like wind.

3.3. *N III] Emission*

GN-z11 also powers strong emission from the N III]λ1750 quintuplet. This feature was detected in the JADES spectrum (A. J. Bunker et al. 2023). The relative quintuplet ratios provide a constraint on the electron density traced by nitrogen-emitting gas in GN-z11 (e.g., R. Maiolino et al. 2024). In particular, the N III]λ1750/λ1752 ratio is very density sensitive, increasing from 1.0 − 1.7 at low gas densities ($10^2 - 10^4$ cm^{-3}) to 2.5 at extremely high gas densities (10^9 cm^{-3}). The SPURS spectrum improves the significance of the N III] line (S/N = 17; left panel of Figure 5) relative to the earlier data. The total N III] flux is $7.9^{+0.5}_{-0.5} \times 10^{-19}$ erg s^{-1} cm^{-2}, implying a luminosity of $1.17^{+0.07}_{-0.07} \times 10^{42}$ erg s^{-1}. Unlike N IV], we do not see concrete evidence for a broad profile in N III] (see Appendix A). However, it is plausible a broad component may be detected with a deeper spectrum: assuming the same broad/narrow flux ratio as in N IV], a broad component in N III] would be detected at SNR$\leq$ 3 in our spectrum.

To assess the relative fluxes of the individual N III] components, we fit the observed line profile with five Gaussian functions, each centered at the rest-wavelengths of the different quintuplet lines, assuming all five components have the same line width. We fix the N III]λ1746/N III]λ1752 and N III]λ1748/N III]λ1754 flux ratios to the respective theoretical values ($f_{\mathrm{NIII}]\lambda1746}/f_{\mathrm{NIII}]\lambda1752} = 0.14$, $f_{\mathrm{NIII}]\lambda1748}/f_{\mathrm{NIII}]\lambda1754} = 0.95$). The N III] fit is shown in the right panel of Figure 5. The derived λ1750/λ1752 flux ratio is $1.6^{+0.3}_{-0.3}$. As we will discuss in more detail in Section 5.3, this ratio lies in a regime that is consistent with a wide range of gas densities. The N III] λ1754 to total N III] flux ratio is also sensitive to electron density. Using JADES spectrum, R. Maiolino et al. (2024) reported a N III]λ1754/N III] flux ratio of 0.25 ± 0.04, consistent with an extremely high density ($\gtrsim 10^9$ cm^{-3}).

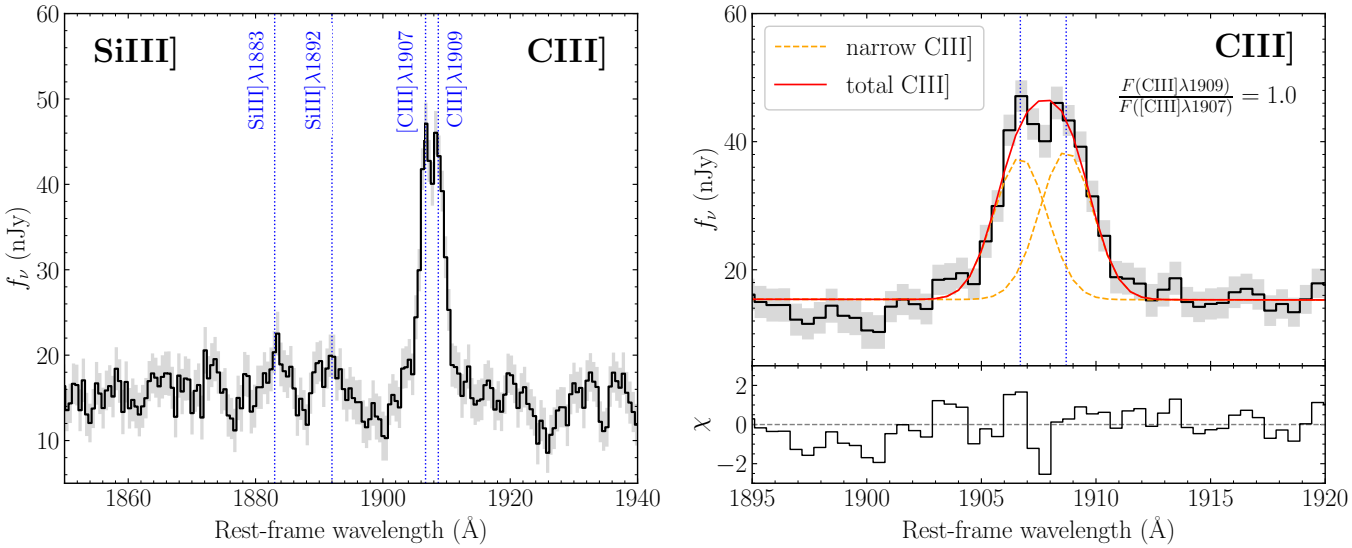

Figure 6. Left panel: Si III] and C III] emission lines of GN-z11. Right panel: Fits to the C III] profile of GN-z11. The figure is shown in the same way as Figure 5. The C III] emission line is best-fitted by two narrow (FWHM = 442 km s^{-1}) Gaussians centered at the rest-frame wavelengths of [C III] λ1907 and C III] λ1909.

We find a N III] λ1754/N III] flux ratio of $0.11^{+0.02}_{-0.02}$, which is lower than that reported in R. Maiolino et al. (2024). This ratio is also consistent with a broad range of densities (see Section 5.3).

3.4. *C III], O III], and Si III] Emission*

The [C III]λ1907, C III]λ1909 doublet is very prominent in the spectrum of GN-z11, providing an important anchor for relative chemical abundance ratios (C/O, N/C) and an additional check on the gas-phase density. Both [C III]λ1907 and C III]λ1909 are detected in the spectrum (Figure 6), with the sum of both components implying a total C III] EW of $8.8^{+0.4}_{-0.4}$ Å. The C III]λ1909/[C III]λ1907 flux ratio varies from 0.6 in the low density limit ($< 10^2$ cm^{-3}) to 2 at high densities ($\simeq 10^5$ cm^{-3}) (e.g., D. E. Osterbrock & G. J. Ferland 2006; L. J. Kewley et al. 2019). The derived λ1909/λ1907 flux ratio in our spectrum ($1.0^{+0.2}_{-0.2}$; right panel of Figure 6) suggests that C III] probes moderately large electron densities in GN-z11. This is consistent with what was concluded based on the lower S/N JADES spectrum (P. Senchyna et al. 2024).

We also detect Si III] λ1883 (S/N = 3.1) and Si III] λ1892 (S/N = 2.6) emission (left panel of Figure 6). We measure a line flux of $1.0^{+0.3}_{-0.3} \times 10^{-19}$ erg s^{-1} cm^{-2} ($7.4^{+2.8}_{-2.8} \times 10^{-20}$ erg s^{-1} cm^{-2}) for Si III] λ1883 (Si III] λ1892), indicating an EW of $1.1^{+0.4}_{-0.4}$ Å ($0.8^{+0.3}_{-0.3}$ Å). While the doublet is also sensitive to electron density, the S/N of the lines is not large enough for a robust calculation.

The auroral O III]λ1666 emission line (S/N = 6, EW = $1.9^{+0.3}_{-0.3}$ Å) is well-detected in the SPURS spectrum

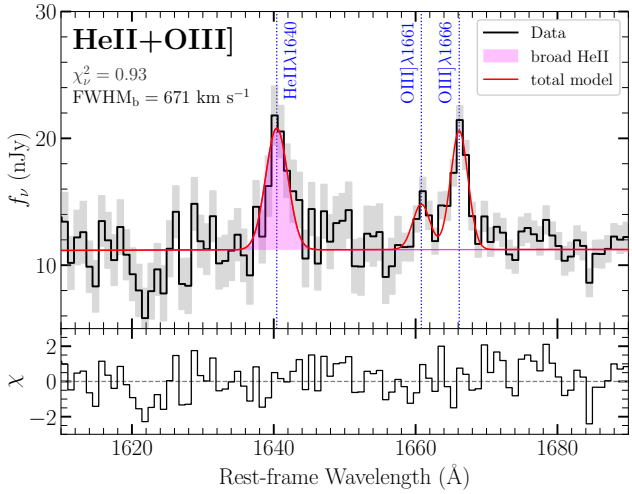

Figure 7. He II and O III] emission lines of GN-z11 and the best-fit model to the line profiles. The spectrum is shown in the same way as Figure 5.

(Figure 7). When combined with [O III]λ5007 (from MIRI, J. Álvarez-Márquez et al. 2025), the UV auroral line provides a constraint on the electron temperature. We also detect the O III]λ1661 emission line (S/N = 3.5, EW = $0.6^{+0.2}_{-0.2}$ Å). This implies an O III]λ1661/O III]λ1666 flux ratio of $0.34^{+0.11}_{-0.11}$, consistent with that calculated from theoretical transition probabilities ($\simeq 0.4$; C. Froese Fischer & H. P. Saha 1985). We will derive the electron temperature and compute a direct method oxygen abundance in section § 5.4.

3.5. *He II Emission*

The He IIλ1640 line was detected (S/N = 4) in the discovery spectrum of GN-z11. He II is a superposition of stellar and nebular emission. The nebular emission is expected to be narrow, with line widths similar to other nebular lines ($\simeq 300 - 400$ km s^{-1}, in the case of GN-z11). In contrast, the stellar wind contribution may be significantly broader (> 500 km s^{-1}), powered by strong winds of WR or VMS populations (e.g., D. Schaerer 1996; R. Chandar et al. 2004; J. Brinchmann et al. 2008; T. Nanayakkara et al. 2019; P. Senchyna et al. 2021). While He II falls in the detector gap of our deepest G140M grating, the SPURS G235M observation covers this line, so the stacked spectrum still has more than double the previous integration time at this wavelength (13.86 hours in our stack). To quantify the line width of the observed feature, we fit He II with a single Gaussian, which is shown in Figure 7. The measured FWHM (671^{+175}_{-178} km s^{-1}, or 600^{+191}_{-209} km s^{-1} after correcting for instrument resolution) is broader than the isolated nebular lines in the rest-UV, consistent with a significant contribution of stellar winds, though we note the FWHM is still consistent with that of other UV nebular lines within 1σ. We find a total He II line flux of $4.1^{+0.7}_{-0.8} \times 10^{-19}$ erg s^{-1} cm^{-2}, corresponding to an EW of $3.3^{+0.6}_{-0.7}$ Å.

3.6. *C IV, N V, and Si IV Emission and Absorption*

The resonant P-Cygni absorption in N V, Si IV, and C IV is a key stellar wind diagnostic from young massive stars (e.g., C. Leitherer et al. 1995; J. Chisholm et al. 2019; P. Senchyna et al. 2021). One challenge in characterizing these features is the blending with the narrow interstellar absorption lines. Here, we describe their profiles qualitatively, while leaving quantitative measurements of interstellar absorption contribution to § 4 and the comparison to stellar population models in § 6.

The C IV $\lambda\lambda$1548,1550 complex provides additional diagnostic power on the nature of the ionizing sources. The JADES discovery spectrum provided tentative evidence for a stellar P-Cygni profile for C IV, but the S/N was not adequate to characterize the profile. SPURS observations provide a more robust view of C IV (see right panel of Figure 8). We see interstellar absorption lines from both components of the doublet, each blueshifted by ≈ -500 km s^{-1} (Figure 12). There is also a broad blueshifted tail of absorption, extending to $\simeq -1000$ km s^{-1}. This is consistent with expectations for strong stellar wind absorption, although we cannot rule out an additional component of fast-moving gas associated with an outflow (e.g., R. Maiolino et al. 2024).

The C IV emission is separated into two peaks, one appearing at rest-frame 1550.7 Å and the other at 1553.3 Å, both redshifted $\simeq +484$ km s^{-1} from the resonance wavelengths of the doublet, which could be consistent with resonant scattering in a fast ($\gtrsim 500$ km s^{-1}), optically thick outflow (e.g., Lim et al. in prep). The total line flux of the C IV emission is $4.5^{+0.5}_{-0.5} \times 10^{-19}$ erg s^{-1} cm^{-2}, and the implied EW is $3.3^{+0.3}_{-0.3}$ Å. The C IV emission is likely a combination of emission from nebular gas and stellar winds. We will estimate the stellar contribution using continuum fitting in section § 6.

The N V$\lambda\lambda$1238, 1242 doublet is also detected in the GN-z11 spectrum, revealing a strong P-Cygni profile (left panel of Figure 8). We detect a broad (FWHM 754^{+253}_{-253} km s^{-1}) and redshifted emission component, with a blueshifted absorption wing extending to $\simeq -3000$ km s^{-1}. The peak flux of the emission line occurs at rest-frame 1244.7 Å, and the implied EW is $1.0^{+0.2}_{-0.2}$ Å. We also detect two narrow absorption components at rest-frame 1237.1 and 1241.2 Å, both blueshifted by ≈ -400 km s^{-1} from resonance. We note that the N V P-Cygni profile can also be suppressed by the IGM damping wing, which we discuss in more detail in Section 6.

Finally, the Si IV resonant doublet ($\lambda\lambda$1393, 1402) also shows a broad P-Cygni profile, consistent with an origin in stellar winds (middle panel of Figure 8), as well as narrower strong interstellar absorption lines. We will explore and quantify the ISM absorption in N V, Si IV and C IV profiles in more detail in section § 4, and the implications for the stellar populations in § 6.

3.7. *O I* fine structure emission*

We detect a faint emission feature (S/N = 3.6) at the observed wavelength of 15140.8 Å, translating to a rest-frame wavelength of 1304.8 Å. This emission feature is just redshifted of the O Iλ1302 and Si IIλ1304 low ionization absorption lines, however we detect no significant absorption (see Section 4 below). This wavelength range includes a blend of several potential emission features: resonant Si II at 1304.37 Å – which may be seen in emission rather than absorption if resonantly scattered photons escape along an optically thin sightline; and O I* fine structure emission at 1304.86 Å and 1306.03 Å. As we show in Figure 9, given the systemic redshift, the emission feature we detect is most consistent with O I* fine structure emission at 1304.86 Å. By fitting a Gaussian profile along with a linear function as the continuum, we derive an observed flux of $1.03^{+0.33}_{-0.24} \times 10^{-19}$ erg s^{-1} cm^{-2}, corresponding to a rest-frame EW of $0.52^{+0.17}_{-0.12}$ Å.

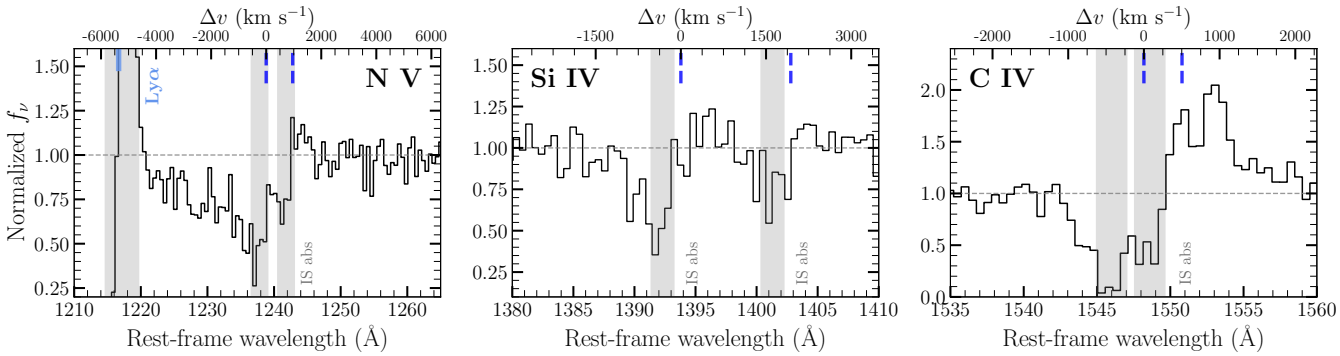

Figure 8. Stellar wind P-Cygni features of GN-z11 (left panel: N V; middle panel: Si IV; right panel: C IV). In each panel, we mark the line center of each component of N V, Si IV, or C IV as blue dashed vertical line. The regions that are impacted by interstellar absorption are masked by grey shades.

O I*λ1304 emission is rarely detected in galaxies at lower redshifts, but is prominently seen in AGN and has recently been reported in several LRDs (R. Tripodi et al. 2025a; M. Tang et al. 2026). In these sources, as well as the Sunburst arc, which shows rest-frame optical O I* emission (M. Pascale & L. Dai 2024; S. Choe et al. 2025), O I* flux is thought to be boosted in very neutral dense gas via Lyβ (Bowen) fluorescence of the $3d^3\,D^0$ excited state of O I (J. Kwan & J. H. Krolik 1981; Y. Matsuoka et al. 2007). If the line is primarily driven by Lyβ fluorescence, we may also expect to see O Iλ1302 in emission: our non-detection suggests the emitting gas is likely optically thick to O Iλ1302. We should also expect O Iλ11287,λ8446 emission, though these are beyond the wavelength range of NIRSpec. O I*λ1304 can also be produced by continuum pumping of O Iλ1302 and subsequent re-emission via fine-structure cascades, analogous to fine-structure lines such as Si II*, C II* and Fe II* commonly seen in $z \sim 2-4$ star-forming galaxies (e.g., A. E. Shapley et al. 2003; D. K. Erb et al. 2012; K. A. Kornei et al. 2013; B. Wang et al. 2020), however we do not detect the low-ionization absorption features which would indicate continuum absorption, nor any other fine-structure emission lines at high significance in GN-z11. This suggests Lyβ pumping may dominate the O I*λ1304 production in GN-z11.

3.8. *[Ne IV] and [Ne V] Emission*

The near-UV is host to several high ionization lines which offer additional diagnostic power on the presence of an AGN. The JADES spectrum revealed a tentative detection of [Ne IV] $\lambda\lambda$2422, 2424 (R. Maiolino et al. 2024; M. Tang et al. 2025). We do not find [Ne IV] in the deeper SPURS spectrum (top panel of Figure 10), placing a 3σ limiting flux of $< 8 \times 10^{-20}$ erg s^{-1} cm^{-2} (EW < 1.6 Å) for each component. This is smaller than the value of the tentative feature in the JADES spectrum ($3.14 \pm 0.65 \times 10^{-19}$ erg s^{-1} cm^{-2}). Either the line is variable, or it is weaker than implied by the tentative feature in the earlier spectrum.

Table 2. Rest-frame near-UV emission line observed-frame wavelengths (Å), fluxes (10^{-19} erg s^{-1} cm^{-2}), EWs (Å), and FWHMs (km s^{-1}) of GN-z11. Upper limits are provided at the 3σ level.

Line	$\lambda_{\rm obs}$	Flux	EW	FWHM
[Ne IV] λ2422	–	< 0.8	< 1.6	–
[Ne IV] λ2424	–	< 0.8	< 1.6	–
Mg II λ2796	32446.6	$2.1^{+0.3}_{-0.3}$	$5.8^{+0.8}_{-0.8}$	366^{+34}_{-34}
Mg II λ2803	32529.0	$1.2^{+0.3}_{-0.3}$	$3.5^{+0.9}_{-0.9}$	366^{+34}_{-34}
[Ne V] λ3427	–	< 0.7	< 3.2	–

We also do not detect the [Ne V] emission line, placing a 3σ limiting line flux of $< 7 \times 10^{-20}$ erg s^{-1} cm^{-2}. This pushes the limit placed in the JADES spectrum ($< 1.5 \times 10^{-19}$ erg s^{-1} cm^{-2}; R. Maiolino et al. 2024) to a deeper sensitivity. The corresponding 3σ upper limit of [Ne V] EW of GN-z11 is < 3.2 Å. We summarize the measurements for these NUV lines in Table 2.

3.9. *Mg II Emission*

We also detect the Mg II $\lambda\lambda$2796, 2803 doublet in emission in the near UV (bottom panel of Figure 10), providing an indication of the neutral gas conditions in GN-z11. Mg II is a resonant transition tracing cool, $T \sim 10^4$ K gas, and its nebular emission doublet ratio is sensitive to gas kinematics, dust attenuation and the Mg II column density (e.g., S.-J. Chang & M. Gronke 2024). Empirically, sources with the Mg II λ2796/Mg II λ2803 emission flux ratio close to the theoretical value (2:1) have been shown to have high Lyα escape fractions (A.

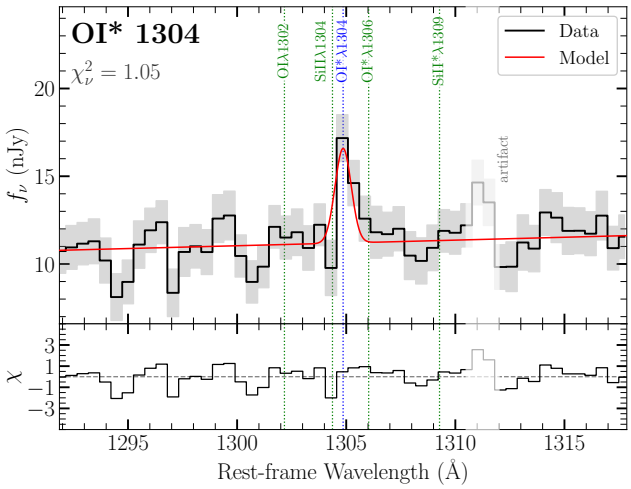

Figure 9. Detection of fine structure emission in O I* λ1304. We present the observed spectrum along with the Gaussian fit, shown in the same way as Figure 5. We also mark the wavelengths of other emission lines around this region, with the detected emission feature best aligning with that of O I* λ1304. We note a feature at ≈ 1311 Å corresponds to an artifact in a single exposure.

Henry et al. 2018) and Lyman continuum escape fractions (J. Chisholm et al. 2020; X. Xu et al. 2023). Dust attenuation, fast outflows (> 700 km s^{-1}), and scattering of the stellar continuum can all preferentially suppress the Mg II λ2796 line relative to Mg II λ2803, reducing the flux ratio below its intrinsic value of 2 (S.-J. Chang & M. Gronke 2024).

We detect both components (combined S/N = 6) in the GN-z11 spectrum, with velocity centroids consistent with line center, implying a total Mg II EW of $9.3^{+1.2}_{-1.2}$ Å, in agreement with previous measurements from the JADES spectrum (A. J. Bunker et al. 2023; R. Maiolino et al. 2024). We measure a Mg II λ2796/Mg II λ2803 flux ratio of $1.7^{+0.5}_{-0.5}$, which is consistent with the theoretically expected value, indicating optically thin neutral gas, though does not rule out lower values. This is consistent with the ratio reported by R. Maiolino et al. (2024), but with improved precision.

3.10. *Rest-Optical Emission Lines*

We identify several rest-frame optical emission lines ([O II], [Ne III]λ3869, He Iλ3889+H8, [Ne III]λ3968+Hϵ, Hδ, Hγ, [O III]λ4363) in the stacked G395M spectrum of SPURS and JADES (Figure 11). We present the rest-frame optical emission line fluxes and EWs in Table 3. The line fluxes are generally consistent with those measured from the JADES spectrum (A. J. Bunker et al. 2023; R. Maiolino et al. 2024). The Ne3O2 ratio is large ($1.2^{+0.1}_{-0.1}$), indicating extreme ionization conditions in the gas of GN-z11. The Hδ/Hγ flux ratio ($0.66^{+0.10}_{-0.10}$) is con-

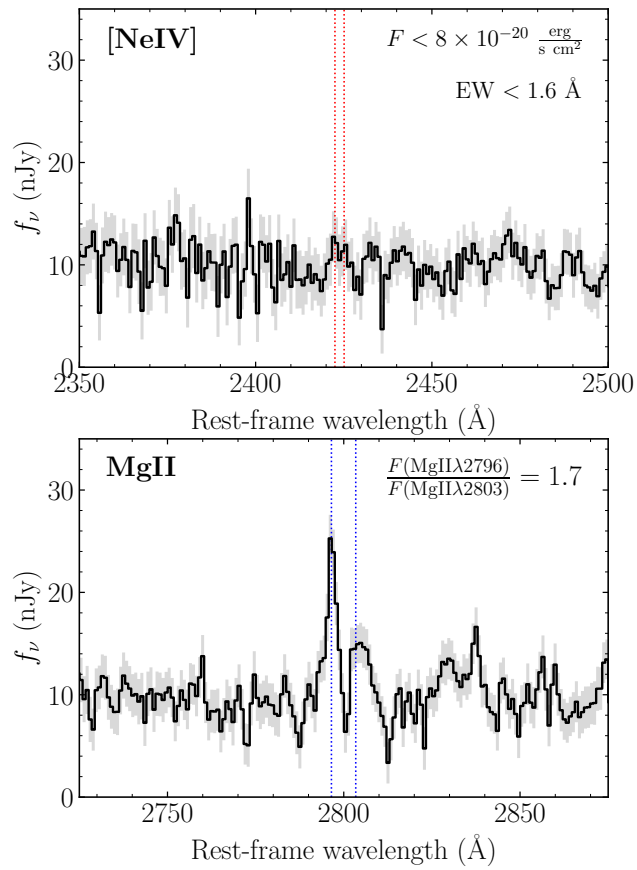

Figure 10. **Top** panel: Non-detection (red dashed lines) of [Ne IV] λ2422, 2424 emission lines of GN-z11. **Bottom** panel: Mg II λ2796, 2803 emission line detections (blue dashed lines) of GN-z11.

Table 3. Rest-frame optical emission line observed-frame wavelengths (Å), fluxes (10^{-19} erg s^{-1} cm^{-2}), EWs (Å), and FWHMs (km s^{-1}) of GN-z11. Upper limits are provided at the 3σ level.

Line	$\lambda_{\rm obs}$	Flux	EW	FWHM
[O II] λ3728[a]	43254.2	$8.0^{+0.4}_{-0.4}$	44^{+2}_{-2}	394^{+24}_{-24}
[Ne III] λ3869	44895.9	$9.7^{+0.4}_{-0.4}$	58^{+2}_{-2}	384^{+15}_{-15}
He I λ3889+H8	45126.9	$2.9^{+0.4}_{-0.4}$	18^{+2}_{-2}	468^{+68}_{-68}
[Ne III] λ3968+Hϵ	46055.3	$5.4^{+0.4}_{-0.4}$	35^{+3}_{-3}	367^{+42}_{-42}
Hδ	47603.3	$4.6^{+0.6}_{-0.6}$	32^{+4}_{-4}	409^{+43}_{-43}
Hγ	50370.4	$7.0^{+0.7}_{-0.7}$	55^{+6}_{-6}	317^{+29}_{-29}
[O III] λ4363	50645.7	$3.0^{+0.8}_{-0.8}$	24^{+6}_{-6}	459^{+43}_{-43}

[a] Unresolved [O II] λλ3727, 3729 doublet.

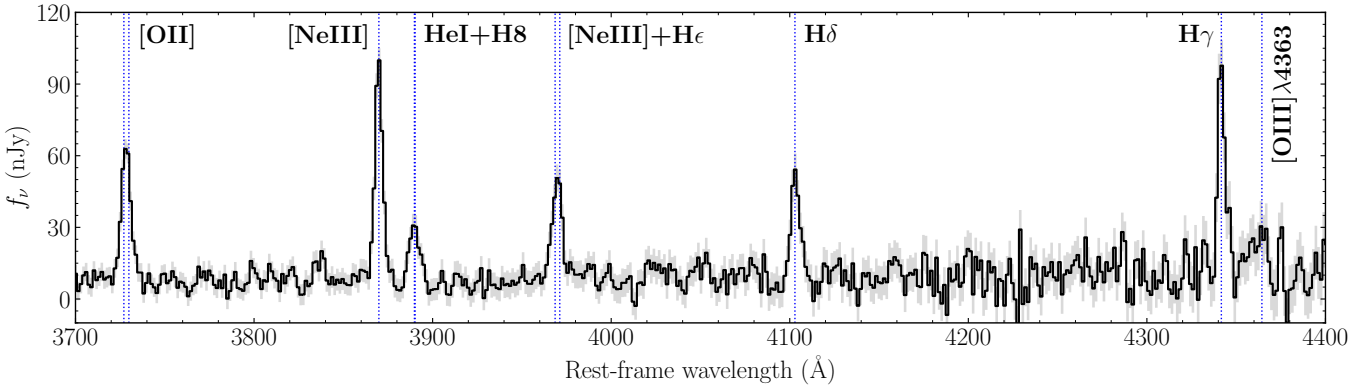

Figure 11. Rest-frame optical (G395M) spectrum of GN-z11. The spectrum is created by stacking both SPURS and JADES observations. We detect a suite of rest-frame optical emission lines ([O II], [Ne III], He I, Hδ, Hγ, [O III] λ4363).

sistent with that expected from case B recombination, suggesting minimal dust attenuation (see § 5.1).

We examine whether the Balmer emission lines present broad components. Visually, no broad emission components are clearly detected in Hγ or Hδ, and their linewidths are consistent with other optical emission lines. However, it is possible a broad component exists below our SNR limit. Assuming the broad line width of N IV] (FWHM = 1670 km s^{-1}), we find the 3σ limiting broad Hγ line flux is $< 3.0\times10^{-19}$ erg s^{-1} cm^{-2}. We consider whether a broad Hγ component would be detected in our data assuming a range of broad-to-total flux ratios given the narrow line flux we measure. We first assume a broad Hγ flux ratio similar to that of N IV] (49%), and find an expected broad Hγ flux of 6.7×10^{-19} erg s^{-1} cm^{-2}. This is above the 3σ limiting flux, indicating a broad component in Hγ as strong as that seen in N IV] is ruled out. We also consider a smaller broad Hγ flux ratio similar to what is found for Hβ in EGSY8p7 ($\simeq$ 0.2; R. L. Larson et al. 2023; S. Zamora et al. 2025). In this case, we expect the broad Hγ flux to be 1.2×10^{-19} erg s^{-1} cm^{-2}, which is comparable to the 3σ limiting flux, indicating we cannot rule out the presence of a broad Hγ component at this level. We note that the same is true for Hα, where a similarly broad component is not ruled out by the current MIRI MRS observation of GN-z11 (J. Álvarez-Márquez et al. 2025)[13].

[13] Using Hα flux measured from the MIRI MRS spectrum (J. Álvarez-Márquez et al. 2025), we would expect the broad Hα line flux in GN-z11 to be 1.3×10^{-18} erg s^{-1} cm^{-2} assuming the broad-to-narrow ratio similar to that in EGSY8p7. Assuming the broad line width is the same as that of broad N IV] (FWHM$_{\rm broad}$ = 1670 km s^{-1}) we place a 3σ flux limit of $< 4.8 \times 10^{-18}$ erg s^{-1} cm^{-2} for broad Hα in the current MIRI MRS spectrum (J. Álvarez-Márquez et al. 2025) – higher than the expected broad line fluxes.

4. INTERSTELLAR ABSORPTION LINES

The SPURS rest-UV spectrum also enables the detection of multiple metal absorption lines, tracing enriched ISM and CGM gas along the line-of-sight to the UV-emitting region in GN-z11, and providing a critical probe of the kinematics and covering fraction of multiphase gas (e.g., M. Pettini et al. 2000, 2002; A. E. Shapley et al. 2003; C. C. Steidel et al. 2010). A key new result from the SPURS spectrum is that the absorbing gas is dominated by highly ionized, outflowing gas.

In Figure 12 we show the spectral regions around low-ionization and high-ionization lines with high oscillator strengths, which are typically observed in bright, star-forming galaxies (e.g., A. E. Shapley et al. 2003; C. C. Steidel et al. 2016). We detect no significant absorption in the low-ionization lines (LIS; Si IIλ1260, O Iλ1302, Si IIλ1304, C IIλ1334, Si IIλ1526, Al IIλ1670), implying a low covering fraction of metal-enriched neutral gas. By contrast, we detect clear absorption in the high-ionization lines (HIS; Si IV$\lambda\lambda$1393, 1402, C IV$\lambda\lambda$1548, 1550) at blueshifted velocities, indicating a highly ionized outflow. We also detect narrow absorption features consistent with blueshifted N V$\lambda\lambda$1238, 1242 absorption, at velocities similar to the other high-ionization absorption lines. Narrow N V absorption is rarely detected at lower redshifts (A. E. Shapley et al. 2003; C. C. Steidel et al. 2016; D. A. Berg et al. 2022), but was recently reported in another bright $z > 9$ galaxy observed by SPURS (Z. Chen et al. 2026). This could have an interstellar origin, but we will also discuss in §7 that it may be a feature of unusual stellar winds.

To quantify the differences between the absorption profiles and the outflow kinematics we fit both the individual line profiles, as well as stacks of the mean low- and high-ionization line profiles. We follow the approach of Vasan G. C. et al. (2026) and refer readers there for a detailed description of our methodology. Briefly, we first

normalize the absorption profiles by the continuum. To account for stellar wind features in the high ionization lines, we consider both of the continuum models presented in Section 6.4 below (CB19 and $M25_{\dot{M}\propto Z}$). To generate stacks of the low- and high-ionization absorption profiles we interpolate the individual spectral regions shown in Figure 12 onto a common velocity grid of $100\,\mathrm{km\,s^{-1}}$ and combine them using an inverse-variance weighted mean. To create the mean profiles, utilize the spectral regions adopted Vasan G. C. et al. (2026) for $z \simeq 5-9$ galaxies. We mask wavelength ranges corresponding to rest-UV emission lines (e.g. C IV nebular emission), and in the case of nearby and potentially blended absorption features (e.g. O Iλ1302, Si IIλ1304, C IV$\lambda\lambda$1548,50) we mask wavelength ranges expected to be contaminated by the other transition. The mean profiles are shown in the top panels of Figure 12. Consistent with the individual lines, we detect no significant absorption in the low-ionization stack, while the high-ionization stack shows clear blueshifted absorption.

To characterize the line profiles, we use a single Gaussian fit to the individual and mean normalized line profiles, measuring the velocity centroid ($v_{\rm cent}$), equivalent width (EW), and intrinsic deconvolved line width, accounting for the spectral resolution (assuming $R = 1000$, see § 2.2). We find the high-ionization absorption line EWs are strong, though the exact values are slightly sensitive to the choice of continuum model. We find the mean EW of the HIS lines is -1.65 Å assuming the CB19 model, and -1.60 Å assuming the $M25_{\dot{M}\propto Z}$ model. In contrast, for the low-ionization lines, assuming unresolved lines, we measure stringent limits of $\gtrsim -0.34$ to -0.28 Å on the absorption EW, significantly weaker than values typically reported at lower redshifts, and in other bright $z \sim 5-9$ galaxies observed by SPURS (≈ -0.9 Å to -1.5 Å, A. E. Shapley et al. 2003; X. Du et al. 2018; A. J. Pahl et al. 2020; Vasan G. C. et al. 2026). Comparably low LIS absorption EWs are typically seen in strong Lyα-emitters, where they have been interpreted as tracing sightlines with a low covering fraction of neutral gas, facilitating Lyα transmission through the ISM and CGM (A. E. Shapley et al. 2003; R. F. Trainor et al. 2015, 2019; X. Du et al. 2018; N. A. Reddy et al. 2022; K. S. Glazer et al. 2025). We report all the inferred line properties for the individual high ionization lines and the mean profile, and the EW upper limits on the individual low-ionization lines in Table 4.

The high-ionization lines are systematically blueshifted, indicating outflowing ionized gas. We measure a velocity centroid of $-492 \pm 15\,\mathrm{km\,s^{-1}}$ from the mean high-ionization profile, assuming the CB19 continuum model. Adopting the $M25_{\dot{M}\propto Z}$ model results in a marginally lower velocity centroid of $-466 \pm 15\,\mathrm{km\,s^{-1}}$. We note these velocities are also consistent with the high outflow velocity suggested by the redshifted C IV emission ($\approx 500\,\mathrm{km\,s^{-1}}$; Section 3). The peak outflow velocities in GN-z11 are significantly faster than the median of the $z \simeq 5-9$ sample reported by Vasan G. C. et al. (2026) ($-211 \pm 63\,\mathrm{km\,s^{-1}}$). We note similarly high peak outflow velocities have been seen in a handful of low redshift galaxies with star formation rates and star formation rate surface densities comparable to GN-z11 (J. Chisholm et al. 2015; T. M. Heckman & S. Borthakur 2016; X. Xu et al. 2022), as well as AGN (K. N. Hainline et al. 2011). In summary, the combination of blueshifted high-ionization absorption and the non-detection of low-ionization species indicates that the absorbing medium in GN-z11 is dominated by outflowing, highly ionized gas.

Table 4. High-ionization and low-ionization absorption line properties. Equivalent widths (EW; Å), centroid velocities ($v_{\rm cent}$; km s^{-1}), and velocity dispersions corrected for instrumental resolution ($\sigma_{\rm deconv}$; km s^{-1}). For high--ionization lines, we report values based on the absorption profiles considering normalization by two different stellar continuum models (CB19 and $M25_{\dot{M}\propto Z}$; see § 6.4).

Line	EW	$v_{\rm cent}$	$\sigma_{\rm deconv}$
High-ionization lines (CB19)			
Si IV λ1393	$-1.3^{+0.2}_{-0.2}$	-500^{+51}_{-51}	214^{+43}_{-43}
Si IV λ1402	$-0.5^{+0.2}_{-0.2}$	-387^{+70}_{-70}	157^{+54}_{-54}
C IV λ1548[a]	$-3.0^{+0.2}_{-0.2}$	-479^{+22}_{-22}	243^{+20}_{-20}
C IV λ1550[a]	$-1.8^{+0.5}_{-0.5}$	-503^{+51}_{-51}	235^{+89}_{-89}
Mean profile	–	-492^{+15}_{-15}	195^{+21}_{-21}
High-ionization lines ($M25_{\dot{M}\propto Z}$)			
Si IV λ1393	$-1.3^{+0.2}_{-0.2}$	-441^{+36}_{-36}	194^{+61}_{-61}
Si IV λ1402	$-0.6^{+0.1}_{-0.1}$	-332^{+72}_{-72}	182^{+36}_{-36}
C IV λ1548[a]	$-2.7^{+0.2}_{-0.2}$	-469^{+19}_{-19}	212^{+21}_{-21}
C IV λ1550[a]	$-1.8^{+0.4}_{-0.4}$	-501^{+40}_{-40}	217^{+70}_{-70}
Mean profile	–	-466^{+15}_{-15}	188^{+20}_{-20}
Low-ionization lines			
Si II λ1260	> -0.31	–	–
O I λ1302	> -0.29	–	–
Si II λ1304	> -0.33	–	–
C II λ1334	> -0.28	–	–
Si II λ1526	> -0.33	–	–
Al II λ1670	> -0.34	–	–

[a] Only the unblended portion of the absorption line was used in the fit. Low-ionization lines are non-detections; limits are 3σ rest-frame equivalent width lower limits.

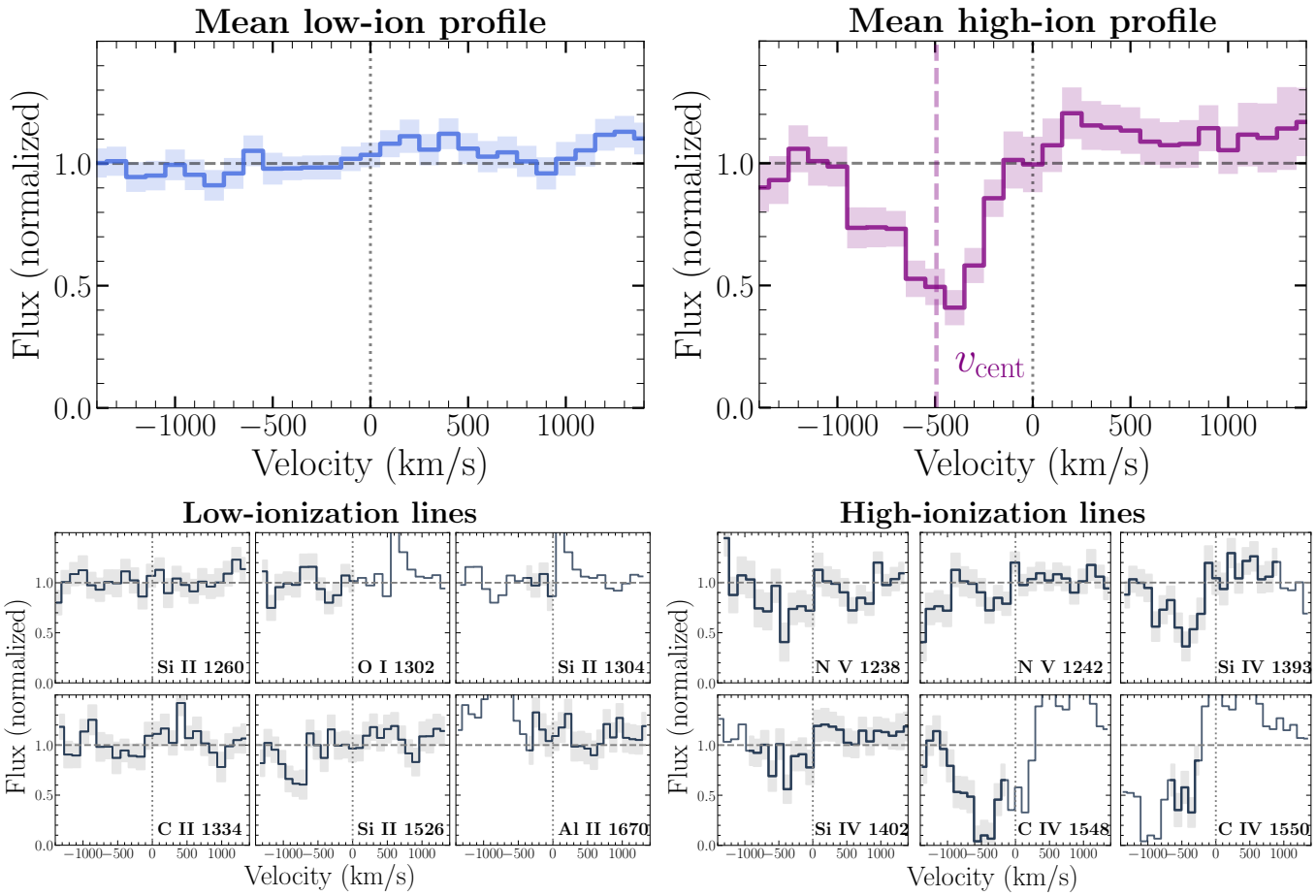

Figure 12. *Top panels*: Mean low- and high-ionization ISM absorption line profiles for GN-z11. The colored shaded region in each panel denotes the 1σ uncertainties. The dotted gray vertical line marks the systemic velocity. The velocity centroid ($v_{\rm cent}$) of the high-ionization mean profile is denoted as purple dashed line. *Bottom panels*: Individual low- and high-ionization line profiles used to construct the mean profiles. In each panel, the gray shaded region denotes the 1σ uncertainties and regions without the uncertainties are masked before combining the lines. For the high-ionization lines, we only use the Si IV and C IV lines but note that the N V shares a similar velocity structure. We show the absorption line profiles normalized based on the CB19 stellar continuum model presented in § 6.4, but we note that the main features, i.e., the strength and the velocity centroid, remain unchanged if using the $\rm M25_{\dot{M}\propto Z}$ continuum model also considered in § 6.4.

5. INFERRED PHYSICAL PROPERTIES

The deeper spectrum motivates updated measurements of several GN-z11 properties, several of which depend sensitively on the assumed physical conditions of the emitting gas. In this section, we quantify the Balmer decrements, the Lyα escape fraction, the electron density and temperature, and the gas-phase oxygen abundance and N/O ratio. We summarize the line ratios and inferred physical properties in Table 5 and 6.

5.1. *Dust attenuation*

To interpret emission lines, we must first constrain the impact of dust reddening on the spectrum. We therefore consider the Balmer decrement. In our stacked spectrum, the Hδ/Hγ ratio ($0.66^{+0.10}_{-0.10}$) provides our best constraint on the Balmer decrement, with both line fluxes measured from the same G395M grating. While the observed Balmer decrement is slightly elevated above the Case B value at an electron temperature of 10^4 K (0.55; D. E. Osterbrock & G. J. Ferland 2006), the measurement is consistent with the intrinsic value within just over 1σ. This suggests negligible dust attenuation, consistent with the blue UV slope ($\beta = -2.4$) reported in A. J. Bunker et al. (2023) using the prism spectrum. This is further supported by the Hα flux measurement from MIRI. If we take the Hδ flux and assume case B recombination without dust, we derive a Hα flux of $5.1 \pm 0.6 \times 10^{-18}$ erg s^{-1} cm^{-2}. This is consistent with that measured from MIRI within 1.6σ ($6.8 \pm 0.9 \times 10^{-18}$ erg s^{-1} cm^{-2}; J. Álvarez-Márquez et al. 2025). As we will show in § 5.6, the absence of dust attenuation is also supported by our joint photoion-

Table 5. Emission line flux ratios of GN-z11. Upper limits and lower limits are provided at the 3σ level.

Line ratio	Value
N IV] λ1486/[N IV] λ1483 (narrow)	> 7.7
N IV] λ1486/[N IV] λ1483 (broad)	> 3.0
N III] λ1750/[N III] λ1752	$1.6^{+0.3}_{-0.3}$
N III] λ1754/[N III]$_{\rm total}$	$0.11^{+0.02}_{-0.02}$
C III] λ1909/[C III] λ1907	$1.0^{+0.2}_{-0.2}$
O III] λ1666/[O III] λ5007	$0.018^{+0.003}_{-0.003}$
[O III] λ4363/[O III] λ5007	$0.022^{+0.006}_{-0.006}$
Hδ/Hγ	$0.66^{+0.10}_{-0.10}$
Ne3O2	$1.2^{+0.1}_{-0.1}$
O32	23^{+3}_{-3}

Note—Line ratios are calculated from narrow line fluxes. The O III] λ1666/[O III] λ5007, [O III] λ4363/[O III] λ5007, and O32 ratios of GN-z11 are calculated using the [O III] λ5007 flux measured from MIRI spectrum reported in J. Álvarez-Márquez et al. (2025) and assuming $f_{\rm [OIII]\lambda4959} : f_{\rm [OIII]\lambda5007} = 1:3$.

Table 6. Physical properties of GN-z11.

Properties	Value
$\tau_{\rm V}$	$0.01^{+0.01}_{-0.01}$
$\Delta v_{\rm Ly\alpha}$/km s^{-1}	252^{+13}_{-6}
$f_{\rm esc,Ly\alpha}$	$0.027^{+0.003}_{-0.003}$
$n_{\rm e}$(N IV])$_{\rm narrow}$/cm^{-3}	$> 7.9 \times 10^5$
$n_{\rm e}$(N IV])$_{\rm broad}$/cm^{-3}	$> 2.5 \times 10^5$
$n_{\rm e}$(N III])/cm^{-3}	$1.1 \times 10^3 - 1.1 \times 10^8$
$n_{\rm e}$(C III])/cm^{-3}	$2.5^{+0.7}_{-0.9} \times 10^4$
$T_{\rm e}$(O^{2+})/K	$1.3^{+0.1}_{-0.1} \times 10^4$
$12 + \log$ (O/H)	$7.94^{+0.14}_{-0.14}$
N/O$_{\rm narrow}$	$0.54^{+0.10}_{-0.08}$
(N/O)$_{\rm narrow}$/(N/O)$_\odot$	$3.9^{+0.8}_{-0.5}$

Note—The electron temperature and gas-phase oxygen abundance of GN-z11 are calculated using the [O III] λ5007 flux measured from MIRI spectrum reported in J. Álvarez-Márquez et al. (2025). The dust optical depth in the V-band (τ_V) is inferred from photoionization modeling with Beagle.

ization modeling of the rest-optical emission lines with BEAGLE.

5.2. *Lyα Escape Fraction*

The escape fraction of Lyα ($f_{\rm esc,Ly\alpha}$) can be computed using dust-corrected Balmer line fluxes. We use the measured Hγ emission line flux assuming no dust correction, consistent with our measurement of the Balmer decrement. Under the assumption of Case B recombination (assuming $T_e = 1.3\times10^4$ K and $n_e = 2.5\times10^4$ cm^{-3} as derived in Section 5.3 and 5.4), we expect an intrinsic Lyα luminosity that is 69$\times$ stronger than Hγ. The observed ratio (Lyα/Hγ = $1.87^{+0.19}_{-0.20}$) implies that GN-z11 has a very low Lyα escape fraction ($f_{\rm esc,Ly\alpha} = 0.027^{+0.003}_{-0.003}$). We note that the Ly$\alpha$ escape fraction would still be small $0.033^{+0.004}_{-0.003}$ if we instead assume the intrinsic Lyα/Hγ ratio (56) found in more typical H II region conditions ($T_e = 10^4$ K and $n_e = 10^3$ cm^{-3}). Our value is broadly consistent with that reported by A. J. Bunker et al. (2023) (0.038 ± 0.004); the small differences reflect differences in the assumed gas conditions and a Lyα flux measurement 1σ lower than theirs.

While we expect that some fraction of the intrinsic Lyα emission may be extended beyond the aperture of the NIRSpec shutter ($0.2'' \times 0.46''$), we note that even if we adopt the integrated Lyα flux as measured from the NIRSpec IFU observations of GN-z11 (Central+NE as reported in Table 1 of J. Scholtz et al. 2024), the resulting Lyα escape fraction is still low ($f_{\rm esc,Ly\alpha} = 0.081^{+0.014}_{-0.013}$ assuming the temperature and density derived in Section 5.3 and 5.4).

5.3. *Electron Density*

We compute the electron densities by jointly fitting the density-sensitive ratios using the `Python` package `PyNeb` (V. Luridiana et al. 2015). We first investigate the density implied by the C III] emission, which has an ionization potential of 24.4 eV and thus constrains the density of gas traced by other ions of similar ionization state, such as [O III]. In the right panel of Figure 13, we plot the ratio–density relation calculated using `PyNeb`. We measure a C III]λ1909/[C III]λ1907 flux ratio of $1.0^{+0.2}_{-0.2}$, which corresponds to an electron density of $2.5^{+0.7}_{-0.9} \times 10^4\,{\rm cm}^{-3}$ for the C III]-emitting gas. This C III]-based electron density we infer appears to be lower than those measured in other strong N IV] emitters (e.g., M. W. Topping et al. 2024, 2025a), but it remains $\sim 1.8\times$ larger compared to what is typically inferred in C III] emitting galaxies (e.g., L. Christensen et al. 2012; B. L. James et al. 2014; M. V. Maseda et al. 2017; D. A. Berg et al. 2021; M. Mingozzi et al. 2022; R. Mainali et al. 2023; M. W. Topping et al. 2025b). Similar values

have also been seen in those with very large Hβ EW, as would be expected if densities are higher in the strongest bursts of star formation (M. W. Topping et al. 2025a).

The N IV]$\lambda\lambda$1483,1486 doublet (ionization potential 47.4 eV) probes gas of considerably higher ionization than C III], providing a constraint on the density of the nitrogen-emitting gas. As discussed in § 3.2, we detect both a broad and a narrow component in N IV]λ1486, and we constrain their densities separately. As shown in the left panel of Figure 13, the narrow N IV]λ1486/[N IV]λ1483 flux ratio (> 7.7) implies an extremely large electron density of $> 7.9 \times 10^5\,\mathrm{cm}^{-3}$ (3σ lower limit) for the narrow-line-emitting gas. The broad component likewise indicates a very high density, with its flux ratio (> 3.0) implying $> 2.5 \times 10^5\,\mathrm{cm}^{-3}$ for the broad-line-emitting gas. Both values are lower limits because, even with data 6× deeper than the previous analysis of GN-z11, the blue component of the doublet, [N IV]λ1483, remains challenging to detect unambiguously. These densities are more than an order of magnitude above the value inferred from C III], and also exceed those found in other known N IV]-emitting galaxies at high redshift ($z > 5$; X. Ji et al. 2024; R. Marques-Chaves et al. 2024; M. W. Topping et al. 2024, 2025a). Both the narrow and broad N IV] lines therefore arise in far denser gas than C III], either because they occupy the densest, innermost zones near the ionizing sources, or because N IV] traces a physically distinct component of the ionized gas.

The final density diagnostic we consider is the N III] multiplet, which traces gas of intermediate ionization (29.6 eV) between that probed by C III] and N IV]. Previous analysis of GN-z11, based on the shallower JADES spectrum, inferred an extremely high density ($> 10^9\,\mathrm{cm}^{-3}$) from the N III] ratio, as expected for a broad-line region (BLR; R. Maiolino et al. 2024). We revisit this possibility using the improved constraints on the N III] ratios afforded by the stacked SPURS+JADES spectrum. We first consider N III] λ1750/N III] λ1752, shown in the middle panel of Figure 13. The observed flux ratio ($1.6^{+0.3}_{-0.3}$) falls close to a region where the density varies rapidly with line ratio, so that its 1σ range maps onto a broad range of densities ($n_e = 1.1 \times 10^3$–$1.1 \times 10^8\,\mathrm{cm}^{-3}$). This ratio nonetheless rules out at $> 3\sigma$ the most extreme densities ($\sim 10^9\,\mathrm{cm}^{-3}$) expected for a BLR. We also examine the N III] λ1754/N III]$_{\mathrm{total}}$ ratio adopted by R. Maiolino et al. (2024), for which we measure $0.11^{+0.02}_{-0.02}$. As this ratio is double-branched in the line-ratio–density relation, our measured value corresponds to either a low density of $\simeq 10^3\,\mathrm{cm}^{-3}$ or a very high density of $\simeq 10^8\,\mathrm{cm}^{-3}$. Given the high densities inferred from the C III] and N IV] ratios, the N III]-emitting gas is likely also dense ($\simeq 10^8\,\mathrm{cm}^{-3}$), yet still an order of magnitude below BLR densities.

In summary, both the C III] and N IV] line ratios indicate high densities for the ionized gas in GN-z11, as would be expected for galaxies undergoing intense bursts of star formation at high redshift (e.g., E. Vanzella et al. 2023; A. Adamo et al. 2024; M. W. Topping et al. 2025a). The nitrogen line ratios point to higher densities, indicating that the nitrogen-emitting gas traces a denser phase that is not necessarily the same component dominating the C III] emission. However, we do not find the extreme densities expected for BLRs are required to explain the measured line ratios.

5.4. *Electron Temperature and Gas-Phase Metallicity*

We detect two auroral lines in the stacked spectrum of GN-z11 (O III]$\lambda\lambda$1661,1666, [O III]λ4363). To derive the electron temperature and gas-phase oxygen abundances, we combine the auroral line measurements with rest-optical emission line fluxes ([O III] λ5007) measured from MIRI reported in J. Álvarez-Márquez et al. (2025). The MIRI [O III] and Hα fluxes were extracted from spatial apertures with radii of $0''.25$ and $0''.3$, respectively, corresponding to 1.5× the FWHM of the MIRI MRS channel 1 ([O III]) and channel 2 (Hα) PSF. Additionally, J. Álvarez-Márquez et al. (2025) performed an aperture correction to account for lost flux, with a computed aperture-correction factor of 1.64×. Because GN-z11 is spatially unresolved in both NIRCam imaging and the MIRI MRS IFU spectra, and the absolute flux calibration of MIRI and NIRCam agrees to within 5%[14] (D. R. Law et al. 2025), the aperture-corrected MIRI fluxes and our NIRSpec fluxes, which we matched to the NIRCam photometry, share a common flux scale. Following J. Álvarez-Márquez et al. (2025), we therefore adopt these fluxes directly in the analysis below, without any additional correction between instruments.

We first consider the electron temperature. Based on the O III] λ1666/[O III] λ5007 ratio, we derive a temperature of $1.3^{+0.1}_{-0.1} \times 10^4$ K (assuming the C III]-based density and zero dust correction). If we use [O III]4363/[O III]5007 ratio, we find a similar temperature of $1.4^{+0.1}_{-0.1} \times 10^4$ K. Because O III]1666 has a higher SNR, we will use the temperature derived from the O III]1666/[O III]5007 flux ratio below.

Using the electron temperatures and densities, we compute the gas-phase oxygen abundance of GN-z11 with the `PyNeb` code. We follow the methodology presented in Y. I. Izotov et al. (2006) and calculate the oxygen abundance as $\mathrm{O/H} \simeq \mathrm{O^{2+}/H} + \mathrm{O^{+}/H}$. The abun-

[14] https://jwst-docs.stsci.edu/jwst-calibration-status/.

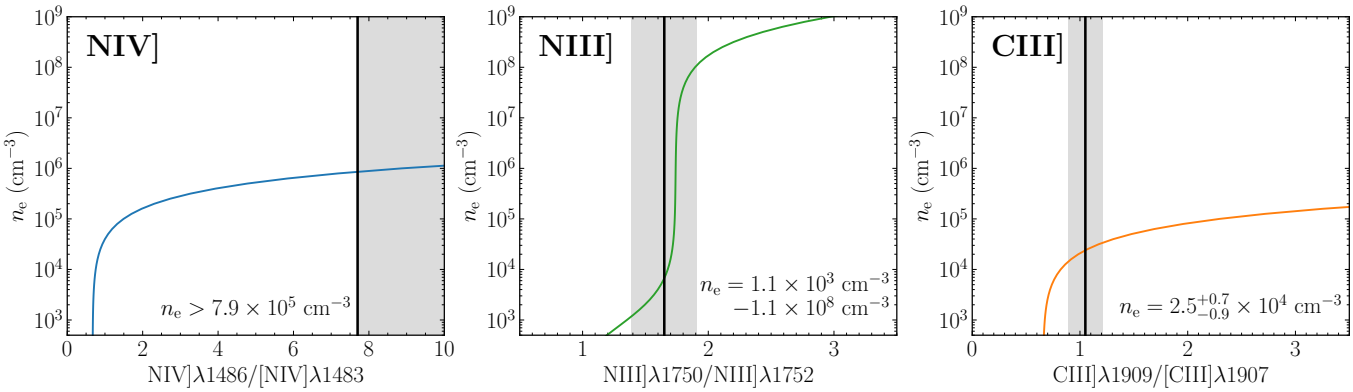

Figure 13. Electron densities of GN-z11 derived from density-sensitive line ratios N IV] λ1486/[N IV] λ1483 (left; narrow line only), N III] λ1750/N III] λ1752 (middle), and C III] λ1909/[C III] λ1907 (right). The colored solid curve in each panel shows the relation between each line ratio and electron density assuming $T = 1.3 \times 10^4$ K (see § 5.4), which is calculated using `PyNeb`. The black solid vertical line and grey shaded region present the observed line ratio and 1σ confidence interval. For N IV] density, we give the 3σ lower limit of the narrow N IV] λ1486/[N IV] λ1483 ratio.

dance of doubly ionized oxygen (O^{2+}/H) is inferred from the [O III] λ5007/Hβ flux ratio. We use the [O III] λ5007 measured in J. Álvarez-Márquez et al. (2025) and Hβ flux derived from Hγ flux assuming case B recombination (Hγ/Hβ = 0.47). For the O^+ zone, the temperature and density are likely different from that of the O^{2+} zone. Since we do not detect [O II] λλ7320, 7330 auroral lines, we derive the O^+ zone temperature following A. Campbell et al. (1986): $T(O^+) = 0.7 \times T(O^{2+}) + 3000$ K. For the O^+ zone density, since we are not able to deblend the [O II] λλ3727, 3729 doublet due to the resolution of the spectra and directly infer the density, we assume a typical value of the low-ionization zone ($n_e \simeq 300$ cm^{-3}) derived in literature (e.g., R. L. Sanders et al. 2024; M. W. Topping et al. 2025b). The singly ionized oxygen abundances (O^+/H) are inferred from the [O II]/Hβ flux ratios based on the above O^+ zone densities and temperatures.

Following this approach, we compute a gas-phase oxygen abundance of $12 + \log(O/H) = 7.94^{+0.14}_{-0.14}$. This corresponds to a moderately low metallicity of $0.18^{+0.07}_{-0.05}$ $Z_\odot$ (assuming the solar oxygen abundance is $12 + \log(O/H) = 8.69$; M. Asplund et al. 2021). This updated measurement is also consistent with the previous works based on the earlier JADES spectrum (and the same MIRI fluxes) (A. J. Bunker et al. 2023; J. Álvarez-Márquez et al. 2025), suggesting that GN-z11 is somewhat chemically enriched.

5.5. *N/O Ratio*

The N/O ratio of GN-z11 was computed using the JADES discovery spectrum. Here we update the measurement of N/O for our deeper spectrum, while considering the impact of the broad N IV] component. We first compute the (N^{3+}+N^{2+})/O^{2+} abundance ratio with `PyNeb` using the narrow (N IV]+N III])/O III] flux ratio based on the derived electron densities and temperatures. To convert (N^{3+}+N^{2+})/O^{2+} into N/O, we apply an ionization correction factor (ICF), which can be computed as a function of gas-phase metallicity and the narrow N IV]/N III] flux ratio (Z. Martinez et al. 2025). As the N IV doublet ratio implies a density of $> 7.9 \times 10^5$ cm^{-3}, and N/O is insensitive to density up to 1×10^9 cm^{-3}, we will assume a density of 7.9×10^5 cm^{-3} and an O^{2+} temperature of $T = 1.3 \times 10^4$ K. We confirm that the N/O does not change if we assume a higher density. Using the above methods, we derive a N/O ratio of $0.54^{+0.10}_{-0.08}$ for the narrow-line-emitting gas in GN-z11. Adopting the solar N/O ratio ($\log(N/O)_\odot = -0.86$; M. Asplund et al. 2021), this corresponds to a super-solar N/O ratio of $3.9^{+0.8}_{-0.5}$ N/O$_\odot$. Compared to earlier measurements based on the JADES spectrum, our narrow-line N/O ratio is consistent with the lower limits reported in A. J. Bunker et al. (2023); A. J. Cameron et al. (2023) (N/O $> 0.43 - 0.56$) in uncertainties, and is in agreement with the measurements of P. Senchyna et al. (2024). Owing to our ability to detect [O III] and resolve the broad component of N IV], we now show cleanly that the narrow N IV] line emitting gas has an N/O abundance enhanced relative to solar.

5.6. *Gas Properties from Photoionization Modeling*

We perform photoionization modeling with BEAGLE to constrain the ionized gas properties and the bulk stellar population properties. Our approach broadly follows that adopted in Z. Chen et al. (2026), where we fit the strong rest-frame optical emission line fluxes ([O II] λ3728, [Ne III] λ3869, Hδ, Hγ, and [O III] λ4363 from the NIRSpec spectra, and [O III] λ5007 from MIRI) along with the pseudo-NIRCam spectral energy distribution

(SED), which is constructed by integrating the full NIRSpec grating spectrum over the standard NIRCam filter set of F150W, F200W, F277W, F356W, F410M, and F444W. We assume a constant star formation history, allowing the age to vary between 1 Myr and the age of the Universe at the source redshift with a log-uniform prior. We keep the remaining assumptions and parameter priors identical to those described in Z. Chen et al. (2026), including the G. Chabrier (2003) stellar initial mass function with mass limits of 0.1–300 $M_\odot$ and the Y. C. Pei (1992) SMC dust attenuation curve.

The BEAGLE J. Gutkin et al. (2016) models successfully reproduce the input rest-frame optical emission line fluxes and their corresponding ratios, with most line fluxes agreeing within 1σ uncertainties. As expected from the large O32 and Ne3O2 values, the models prefer a very high ionization parameter of $\log U = -1.82^{+0.08}_{-0.09}$. The observed Balmer decrements, along with constraints from the continuum slopes of the pseudo-photometry, suggest little to no dust attenuation, yielding a V-band optical depth of $\tau_{\rm V} = 0.01^{+0.01}_{-0.01}$ for GN-z11. To reproduce the full set of emission line ratios, particularly those involving the [O III] λ4363 auroral line, the models require low metallicities with $Z_* = Z_{\rm ISM} = 0.15^{+0.03}_{-0.02}\ Z_\odot$ in GN-z11. At the fitted dust-to-metal ratio ($\xi_d = 0.18^{+0.11}_{-0.05}$), these ISM metallicities also translate to a low gas-phase oxygen abundance of $12 + \log({\rm O/H}) = 7.92^{+0.10}_{-0.09}$, consistent with the value directly inferred from emission lines using the direct-T_e method in § 5.4.

6. STELLAR CONTINUUM MODELING

The deep rest-UV spectrum for GN-z11 provides us with the rare opportunity to compare the latest stellar population models with observations at $z > 10$, offering us a window into the massive star populations in this source. In particular, we seek to test whether the observed continuum together with the stellar wind profiles can be reproduced by the models that include modern treatments of very massive star atmospheres, and its implications for their presence in GN-z11. We first introduce these stellar population models in § 6.1, review the stellar wind features predicted by these models in § 6.2, discuss the impact of the IGM damping wing on our N V modeling in § 6.3, and compare the models to the observed spectrum in § 6.4.

6.1. *Stellar Population Models*

We make use of recent stellar population models presented in F. Martins et al. (2025) and updated versions of the G. Bruzual & S. Charlot (2003) (Charlot & Bruzual, in preparation) models, as described in several recent studies (J. Gutkin et al. 2016; A. Vidal-García et al. 2017). The models incorporate developments in the modeling of massive-star populations, including updates to evolutionary tracks, mass-loss prescriptions, and atmosphere modeling. Below we briefly summarize the stellar population models, and then we describe the addition of nebular continuum emission.

The CB models used here are described in A. Plat et al. (2019) (hereafter referred to as CB19), updating those presented in J. Gutkin et al. (2016); A. Vidal-García et al. (2017), and the reader is directed to these studies for a complete description. The CB19 models use updated evolutionary tracks for very massive stars (VMS) up to 300 $M_\odot$, computed with the PARSEC code (Y. Chen et al. 2015). The models adopt a revised stellar mass-loss prescription that accounts for enhanced mass loss at higher stellar Eddington factors (J. S. Vink et al. 2011). Compared to the previous mass-loss treatments (e.g., J. S. Vink et al. 2001) used by older stellar population models, this recipe produces stronger, more optically thick winds at the highest stellar luminosities, even at low metallicity. These models use updated spectra for hot massive stars calculated with the WM-basic code (A. Pauldrach et al. 1986) from Y. Chen et al. (2015). Emission from Wolf-Rayet (WR) stars is included using the line-blanketed, non-LTE, spherically expanding models from the Potsdam Wolf-Rayet (PoWR) group, spanning stellar effective temperatures of $10^{4.4}$–$10^{5.3}$ K and metallicities $Z = 0.001$–0.014. These updates have been shown to provide better agreement with the observed strength of stellar wind lines, particularly broad He II, in low-metallicity $z \sim 0$ galaxies (e.g., P. Senchyna et al. 2021; A. Wofford et al. 2023). We generate a grid of simple stellar population (SSP) CB19 models using the BEAGLE tool (J. Chevallard & S. Charlot 2016) to create SSP spectra as a function of age and metallicity, assuming the G. Chabrier (2003) IMF with the upper mass cutoff of 300 $M_\odot$.

We also use the F. Martins et al. (2025) stellar population models (hereafter M25), which also adopt updated prescriptions for the evolution and spectroscopic appearance of massive stars. Here, spectra for VMS with masses up to 300 $M_\odot$ are derived from evolutionary tracks computed with the STAREVOL code, using mass-loss recipes thought to be appropriate at these masses (G. Gräfener 2021). Compared to the J. S. Vink et al. (2011) prescription used by the CB19 models, the G. Gräfener (2021) recipe has a steeper scaling of mass-loss rate with Eddington factor, producing stronger winds at fixed stellar mass and metallicity (e.g., 0.3 dex higher for a 250 $M_\odot$ track at 0.4 $Z_\odot$; F. Martins & A. Palacios 2022). The models consider two treatments of the metallicity dependence of the op-

tically thick winds, motivated by differing results from the still-limited observations of individual massive stars below LMC metallicity. The first one assumes the metallicity scaling of the mass loss rate for optically thick winds which decreases towards lower stellar metallicity ($\log \dot{M}_{\rm thick} \propto Z$) as found for classical WR stars (R. Hainich et al. 2015), while the second one adopts no such scaling, where the mass loss rate of optically thick winds $\dot{M}_{\rm thick}$ is held fixed at its value at $Z_{\rm LMC}$ so the winds remain strong down to very low metallicity (e.g., L. J. Smith et al. 2023). We will refer to these models as $\rm M25_{\dot{M}\propto Z}$ and $\rm M25_{\dot{M},LMC}$, respectively.

In both M25 cases, the atmosphere models and synthetic spectra are computed self-consistently with CMFGEN (D. J. Hillier & D. L. Miller 1998), using the evolutionary models' surface properties at ages of 0–2.5 Myr in steps of 0.5 Myr, for initial masses of 150–300 $M_\odot$ in steps of 50 $M_\odot$. The SSP spectra from F. Martins et al. (2025) are synthesized by combining the VMS spectra described above (corresponding to stars with mass $> 100\ M_\odot$) with those of normal stars below 100 $M_\odot$ from the BPASS single star models (J. J. Eldridge et al. 2017), normalized to the initial mass function with an upper initial mass function slope of -2.35 above 0.5 $M_\odot$. Since the F. Martins et al. (2025) models are available only at three metallicities (0.01, 0.1, and 0.2 $Z_\odot$ [15]), we interpolate between these grid points in logarithmic space to obtain models at intermediate metallicities.

To compare with the observed GN-z11 spectrum, we must also add the nebular continuum, which can contribute significantly to the total continuum in the far-UV at the youngest stellar population ages (e.g., M. W. Topping et al. 2022; H. Katz et al. 2025). Specifically, we compute the nebular continuum with PyNeb (V. Luridiana et al. 2015) from the ionizing photon production rate of the stellar emission, assuming $n_{\rm H} = 2.5 \times 10^4$ cm^{-3} and $T_e = 1.3 \times 10^4$ K, consistent with what we measured from the spectrum (see § 5.3 and 5.4). We then add this component to each CB19 and M25 template. In addition to these models, we also use the models without very massive stars to investigate the impact of the IMF. For CB19 models, we will compare to the version synthesized with BEAGLE assuming an IMF upper mass cutoff of 100 $M_\odot$. For M25 models, we will directly use the BPASS models for single stars with the same upper mass cutoff of 100 $M_\odot$, assuming the same initial mass function slope of -2.35 above 0.5 $M_\odot$ as used in constructing the M25 population synthesis model. We use these SSP models to explore the expected stellar wind features as a function of age and metallicity, and to compare with the observed UV continuum.

[15] We note that the F. Martins et al. (2025) models assume a solar metallicity of $Z_\odot = 0.013446$, which is slightly different from the value ($Z_\odot = 0.01524$) adopted in C&B models and BEAGLE. As the difference is small, and in order to avoid interpolation when possible, we chose to use the M25 models directly following their own solar metallicity definition.

6.2. *Model Expectations for Stellar Wind Lines*

To guide understanding of our spectral fitting results (§ 6.4), we first quantify the predicted stellar wind features from the models described in the previous subsection. We explore the strength of these stellar wind features (in terms of the EW) as a function of stellar population age and metallicity. We assume a constant star formation history, but note that the true star formation histories inferred will be a combination of different age SSPs. This investigation will help understand how the free parameters in our fit (i.e., metallicity, age, IMF) can be adjusted to reproduce the observed spectrum.

Our choice of model stellar metallicity (sensitive primarily to the iron abundance in the O/B photospheres) is informed by the oxygen-based gas-phase metallicity (0.18 $Z_\odot$) derived in § 5.4. Given the delay in iron production (dominated by Type Ia supernovae) relative to oxygen (dominated by Type II supernovae), we expect high-redshift galaxies to be α/Fe-enhanced. Indeed, among $z \simeq 2-3$ galaxies, stellar metallicities are typically found to be a factor of 5 lower than gas-phase metallicities (e.g., C. C. Steidel et al. 2016; R. L. Sanders et al. 2020; M. W. Topping et al. 2020; J. N. Runco et al. 2021). This value approaches that expected from Type II supernova yields alone ($\simeq$0.2 $(\rm O/Fe)_\odot$, K. Nomoto et al. 2006). As a result, we adopt models with $Z_* = 0.04\ Z_\odot$ as those most likely to represent the stellar metallicity of GN-z11. We additionally consider models with stellar metallicity 0.1 $Z_\odot$ and $Z_* = 0.2\ Z_\odot$, but consider these unlikely for GN-z11.

We measure the strength of rest-UV stellar wind features in the models described in §6.1, focusing here on those features covered by our NIRSpec observations including N v, Si iv, and C iv P-Cygni profiles and the broad He ii λ1640 emission. We measure equivalent widths by normalizing the model spectrum with a linear fit to the line-free continuum windows given below, then integrating the normalized profile over a velocity interval chosen to span the full blueshifted P-Cygni absorption trough or the broad He II emission. For both N v, and C iv P-Cygni features, we integrate the blueshifted absorption trough over $[-3000, 0]$ km s^{-1} relative to N v λ1238 and C iv λ1548, respectively, with continuum windows $[1260, 1320]$ Å (N v) and $[1500, 1510]$

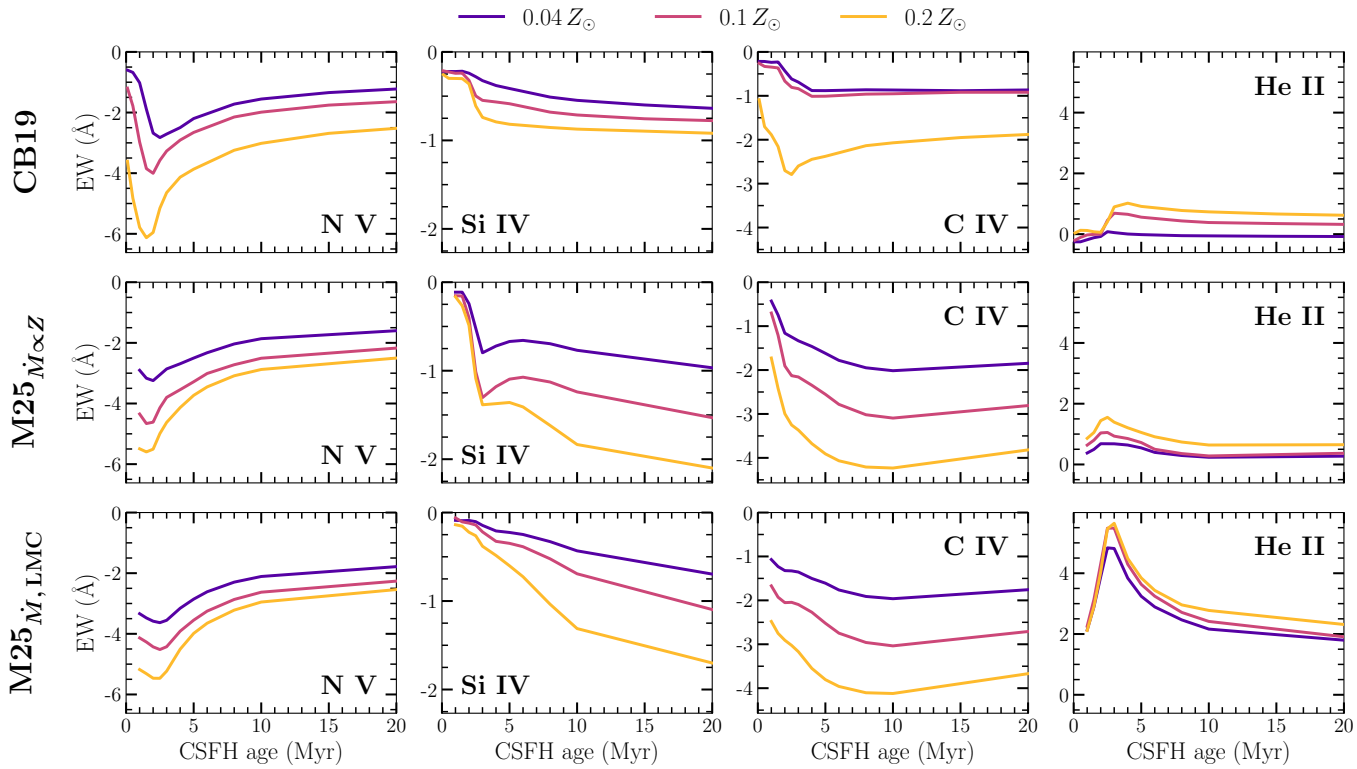

Figure 14. Strengths of the N V, Si IV, and C IV P-Cygni absorption features, and the broad stellar He II emission feature, as a function of stellar population age assuming a constant star formation history (CSFH). We show three sets of models: the CB19 stellar population models (top), the F. Martins et al. (2025) models with metallicity scaling of optically thick mass-loss rates ($M25_{\dot{M}\propto Z}$, middle), and those without such scaling ($M25_{\dot{M},LMC}$, bottom). Different colors show three stellar metallicities relevant to this work, $Z = 0.04$, 0.1, and 0.2 $Z_\odot$, noting that $Z = 0.04$ is the metallicity we would expect for GN-z11 from its gas-phase metallicity assuming Type II SNe yields ($\simeq 0.2$ (O/Fe)$_\odot$).

and [1570, 1580] Å (C IV). For Si IV P-Cygni, we integrate the absorption of each component of the doublet over [−2000, 500] km s^{-1} and sum the two, using continuum windows [1340, 1360] and [1400, 1450] Å. For the broad He II emission, we integrate the full profile over [−2000, 2000] km s^{-1}, with continuum windows of [1600, 1620] and [1670, 1690] Å.

We summarize the range of EWs and their dependence on simple stellar population age and stellar metallicity for three sets of models in Figure 14. Because the N V P-Cygni profile is limited to the hottest stars, we expect the feature to be a signpost of very young stellar populations (e.g., N. R. Walborn et al. 1985; C. Leitherer et al. 1995, 2010; P. A. Crowther et al. 2016). Indeed, as shown in the left panels of Figure 14, the strongest N V P-Cygni absorption is seen in stellar populations with CSFH ages of 2–3 Myr. The age dependence of N V will appear even more pronounced with SSP models, given the rapid disappearance of the most massive stars from the stellar population. We also see that N V wind line is mildly metallicity-sensitive, with the peak absorption EW increasing by a factor of 1.5–2.2 across the three model sets, from the lowest to the largest metallicity we consider (0.04–0.2 $Z_\odot$). The Si IV and C IV P-Cygni absorption are well-known to trace the stellar metallicity (e.g. S. A. Rix et al. 2004; C. Leitherer et al. 2010, 2011; A. Vidal-García et al. 2017; J. Chisholm et al. 2019), with stronger winds as metallicity increases, driving an increase in the median absorption EW by a factor of 2.0–2.3 for Si IV and 2.4–2.5 for C IV over the same metallicity range. As broad He II emission traces the optically thick winds from the most massive O stars near the Eddington limit or from WR stars (e.g., D. Schaerer 1996; P. A. Crowther 2007; J. Brinchmann et al. 2008; P. Senchyna et al. 2021), the emission peaks over the first 3–4 Myr after star formation begins. For composite star formation histories, the age dependence can be more complicated, and indeed, we see broad He II remaining visible at slightly older CSFH ages in Figure 14. As has been found in many works (e.g., P. A. Crowther et al. 2016; A. Wofford et al. 2023; A. Upadhyaya et al. 2024), the strength of these features depends on the initial mass function, and including VMS as we consider here leads to stronger P-Cygni profiles and broad He II

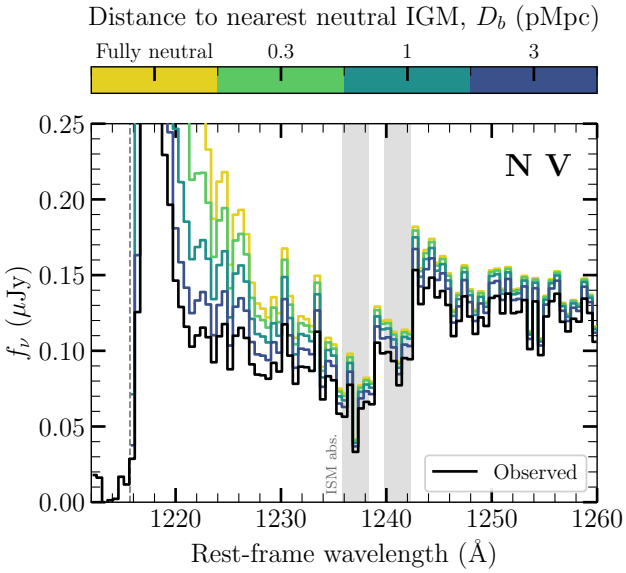

Figure 15. Impact of IGM damping-wing absorption on the N V stellar-wind profile. We show the spectrum corrected for the IGM transmission expected across a range of distances, D_b, to the nearest neutral IGM. In the case where the IGM is fully ionized, the corrected spectrum is identical to the observed one.

emission relative to models without them. Comparing the M25 and CB19 models, we find differences in the strength of these features at fixed metallicity and age, with the M25 models showing $\approx 2\times$ stronger Si IV and C IV P-Cygni absorption. We also see differences between the two M25 models, with $\mathrm{M25}_{\dot{\mathrm{M}},\mathrm{LMC}}$ reaching significantly larger ($\approx 3\times$) He II EW than $\mathrm{M25}_{\dot{\mathrm{M}}\propto\mathrm{Z}}$, a result expected from the enhanced optically thick winds at low metallicity in that model. This variation emphasizes how sensitive the wind lines are to the specific physics in the models, much of which remains poorly constrained.

6.3. *Impact of IGM Damping Wing on N V*

At the redshift of GN-z11, where the intergalactic medium (IGM) is expected to be largely neutral, strong damping wing absorption may suppress the continuum flux at wavelengths redward of Lyα, including across the N V stellar wind region (e.g., J. Miralda-Escudé 1998). Therefore, to interpret the observed N V P-Cygni profile and compare it with models, we must account for the damping wing. To do so, we first investigate how the intrinsic spectrum would appear considering a range of sizes for the ionized bubble in which GN-z11 resides.

We derive the expected transmission as a function of observed wavelength by integrating the damping wing component of the Lyα optical depth arising from neutral hydrogen along the line of sight, adopting the approach of C. A. Mason & M. Gronke (2020); C. A. Mason et al. (2026). We assume the galaxy sits within an ionized bubble at a distance D_b to the nearest neutral IGM patch, beyond which the IGM is assumed to be fully neutral (which is a reasonable approximation in the early stages of reionization, e.g., A. Mesinger & S. R. Furlanetto 2008). We integrate the damping wing optical depth from the edge of the ionized region to the redshift at the end of reionization. We adopt a reionization end redshift of $z_{\mathrm{reion}} = 5.5$, but note this has little impact on the resulting transmission, since the optical depth is dominated by neutral hydrogen within $\lesssim 100$ cMpc of the galaxy.

In Figure 15 we present the spectrum corrected for IGM transmission considering a range of distances from GN-z11 to the nearest neutral IGM, D_b. As expected, the intrinsic N V P-Cygni profile can deviate from the observed spectrum significantly if GN-z11 resides in very small ionized regions. In the most extreme case corresponding to a fully neutral IGM ($D_b = 0$ pMpc), the expected transmission at rest-frame 1238 Å (wavelength of the blue component of N V doublet) is only 81%. If we correct the observed spectrum by this transmission, the corresponding intrinsic N V P-Cygni absorption becomes much weaker, with the resulting absorption EW $\approx 2\times$ lower than what is directly measured from the observed spectrum. When D_b is small, the broad N V redshifted emission also becomes stronger in the corrected (intrinsic) spectrum. The IGM impact on N V decreases for increasing distances to the neutral IGM, with the corrected spectrum approaching the observed spectrum when $D_b \geq 3$ pMpc. We note that if D_b is small, the intrinsic flux between Lyα and N V also increases. This could reflect a larger continuum flux, and potentially contribution from broad Lyα emission – beyond what is seen in the observed spectrum. In the next subsection we discuss the implications for the Lyα profile given our best-fit continuum models. While a full, joint fit of the damping wing and stellar populations is left to future work, combining the N V emission with the other stellar-wind features and the strength of Lyα emission should enable a more precise separation of the IGM attenuation and the intrinsic strength of N V absorption.

We consider the range of bubble sizes GN-z11 likely resides in, and the resulting implications for our UV continuum modeling, based on recent theoretical work and observational constraints on the IGM at $z > 9$. The sizes of ionized bubbles depend on the IGM neutral fraction, such that galaxies at the earliest stage of reionization are expected to reside in small ionized bubbles (e.g., M. McQuinn et al. 2007). *JWST* observations have demon-

strated strong Lyα emission becomes very rare with increasing redshift at $z > 8$, indicating decreasing ionized bubble sizes and that the IGM is likely highly neutral at $z = 10.6$. Recent estimates based on Lyα visibility suggest the IGM is $\approx 90 \pm 10\%$ neutral at $z > 10$ (M. Tang et al. 2024a; Y. Kageura et al. 2025). For such high neutral fractions, reionization simulations predict small median bubble radii of $0.1 - 0.3$ pMpc (T.-Y. Lu et al. 2024; M. Neyer et al. 2024). UV-bright galaxies, such as GN-z11, are expected to trace overdense regions at these redshifts, which may ionize early and host larger bubbles. We therefore consider the models of T.-Y. Lu et al. (2024) and M. Neyer et al. (2024) which estimate bubble sizes around $M_{\rm UV} < -21$ galaxies, accounting for their environments. Both models predict UV-bright galaxies sit at a median distance $D_b \approx 0.3$ pMpc from the neutral IGM, with the T.-Y. Lu et al. (2024) models finding a 68% range of $0.2 - 0.5$ pMpc. This is also consistent with our Lyα measurement, where the small EW and low escape fraction ($f_{\rm esc,Ly\alpha} = 0.027^{+0.003}_{-0.003}$) suggest a large bubble is unlikely: assuming $D_b = 0.2 - 0.5$ pMpc, the IGM transmission at the Lyα wavelength is 0.3–7%. However, for very small bubbles with $D_b < 0.1$ pMpc, we find the IGM transmission correction factor at the observed Lyα peak wavelength will be very large, leading to an unphysically high value of Lyα escape fraction above unity. Therefore, in our modeling, we will adopt $D_b = 0.5$ pMpc as the most likely distance to the neutral IGM, but we will also discuss the impact if the bubble is smaller (down to 0.1 pMpc) or larger.

The weak low-ionization absorption lines (§ 4) imply either the total HI column density in front of the UV continuum is lowWe also consider damped Lyα absorption (DLA) from high-column-density neutral hydrogen in the vicinity of the stars, finding a DLA is unlikely to significantly affect the continuum near N V of GN-z11. The weak low-ionization absorption lines (§ 4) imply either the total HI column density in front of the UV continuum is low, or, if present, a very metal-poor DLA. Low-to-moderate HI column densities have little effect on the continuum near N V, because the DLA optical depth declines more steeply with wavelength offset from Lyα than the IGM damping wing ($\tau_{\lambda,\rm DLA} \propto 1/(\Delta\lambda)^2$ versus $\tau_{\lambda,\rm IGM} \propto 1/\Delta\lambda$, M. McQuinn et al. 2008): a $N_{\rm HI} = 10^{20.5}(10^{21.0})$ cm^{-2} DLA still transmits 97%(92%) of the flux at rest-frame 1238 Å (wavelength of the blue component of the N V doublet). While larger column densities ($N_{\rm HI} \gtrsim 10^{22}$ cm^{-2}) could suppress the N V flux, we find this would imply an unphysical intrinsic spectrum: producing both an unrealistically large continuum flux between Lyα and N V and an extremely high N V emission flux. Together, this suggests a strong DLA is unlikely in GN-z11 and that the continuum near N V is mainly modulated by the stellar P-Cygni profile and the IGM damping wing, which we focus our modeling on below.

6.4. *Fitting the GN-z11 Rest-UV Spectrum*

Using the models described above, we now fit the observed UV continuum spectrum of GN-z11, building on our previous work with the $z = 9.3$ galaxy SPURS-A2744-7 (Z. Chen et al. 2026). In this study, we use the FiCUS code (A. Saldana-Lopez et al. 2023), modeling the UV continuum as a linear combination of simple stellar populations (J. Chisholm et al. 2019). We consider several stellar population models (see § 6.1) and fit the data assuming a range of stellar metallicities (0.04–0.2 $Z_\odot$; see §6.2), bubble sizes (see § 6.3), and two upper mass IMF cutoffs (100 and 300 $M_\odot$). In each case, we fit over an SSP age grid of 1, 2, 3, 4, 5, 8, 10, 15, 20, and 40 Myr. Our goals are twofold. First, we seek to determine whether the current generation of stellar population models are capable of reproducing the UV spectrum of GN-z11. Second, we want to know what the model fits suggest about the properties of the massive star populations in GN-z11, in particular whether the wind lines are best reproduced with the inclusion of VMS as implemented in the CB19 and M25 models.

We fit the rest-frame continuum from 1228 to 1920 Å, where the blue cutoff is chosen to avoid contamination from the red wing of Lyα. We mask nebular emission lines using windows matched to the width of each line. Specifically, we mask -3500 to 3500 km s^{-1} around the N IV] doublet and N III] multiplet, -200 to 200 km s^{-1} at the core of He II line that may have a significant contribution from nebular emission, and -500 to 500 km s^{-1} for the remaining lines (including the nebular C IV). We likewise mask the interstellar absorption, using a -500 to 500 km s^{-1} window around each absorption centroid identified in Section 4. We account for dust attenuation, assuming the SMC attenuation curve (K. D. Gordon et al. 2003). FiCUS finds the best-fit model by χ^2 minimization with the LMFIT package (M. Newville et al. 2016), and estimates uncertainties with a Monte Carlo approach that perturbs the spectrum according to the error array and refits the perturbed spectrum 100 times, adopting the standard deviation of the resulting parameter distributions.

We first consider the results from fits to the GN-z11 spectrum with CB19 and M25$_{\dot{\rm M}\propto {\rm Z}}$ models that assume our preferred low stellar metallicity (0.04 $Z_\odot$, §6.2), a small bubble size (0.5 pMpc, §6.3) and an IMF that extends up to 300 $M_\odot$. We define these as our fiducial model set. As shown in Figure 16 and 17, we find that

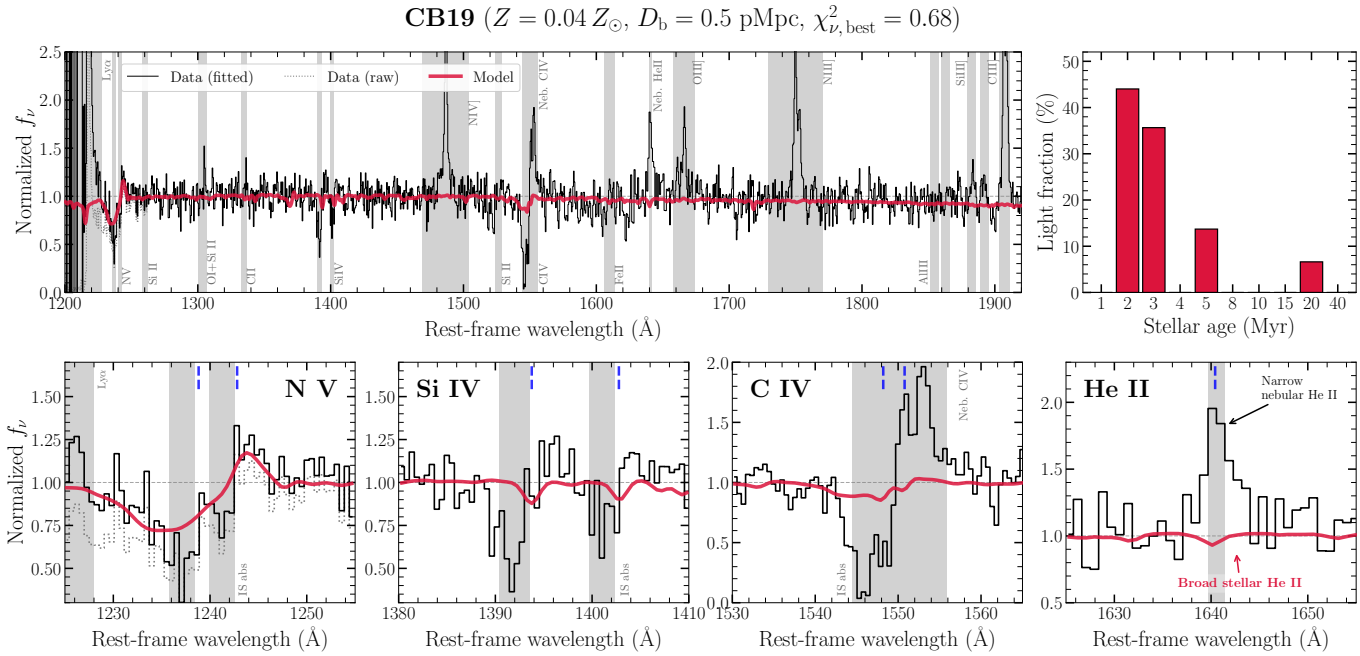

Figure 16. FiCUS fit to the UV continuum of GN-z11 using linear combinations of CB19 SSP models with an IMF upper mass cutoff of 300 $M_\odot$. Shown are the fits to the observed spectrum corrected for IGM transmission, assuming a distance to the nearest neutral HI of 0.5 pMpc, and our preferred low metallicity of $Z_* = 0.04\ Z_\odot$. **Top left**: The full UV continuum used for fit (black), the original observed spectrum before applying the correction for IGM transmission (dotted blue), and the best-fit model (red). Nebular emission lines and interstellar absorption lines are masked during the fit, which are shaded in gray. **Top right**: The star formation history corresponding to the best-fit model, parameterized as the light fractions of the UV continuum at 1360 Å as a function of SSP age. **Bottom**: Zoomed-in views of the FiCUS fits to the N V, Si IV, and C IV P-Cygni profiles, and broad stellar He II emission.

both of these fiducial models provide satisfactory fits to the spectrum ($\chi^2_\nu = 0.68$ and 0.66, respectively). As expected, the strong N V P-Cygni profile in GN-z11 forces the models to a very young stellar population. In particular, we find that best-fitting SFH is dominated by two SSPs at 2 and 3 Myr in both the CB19 and the $\mathrm{M25}_{\dot{\mathrm{M}}\propto\mathrm{Z}}$ fits. At such young ages, the N V wind absorption EW is strong (-2.5 Å in CB19 and -2.2 Å in $\mathrm{M25}_{\dot{\mathrm{M}}\propto\mathrm{Z}}$), providing a good match to the data. Importantly both models also match the N V P-Cygni emission component. At the low stellar metallicity of these models, the Si IV and C IV P-Cygni profiles are weak but not negligible. We find that the C IV absorption EW in our best fitting models is larger in the $\mathrm{M25}_{\dot{\mathrm{M}}\propto\mathrm{Z}}$ (-1.8 Å) than CB19 (-1.1 Å) models. Both stellar wind profiles are consistent with the observations, easily accommodated within the deep interstellar absorption profile. We also find that the broad He II emission is different between the two models: the $\mathrm{M25}_{\dot{\mathrm{M}}\propto\mathrm{Z}}$ best fit has a modest stellar He II EW (0.7 Å) while that from the fiducial CB19 fit is negligible. The observed He II profile is formally consistent with both models since the blend of stellar and nebular emission at $R = 1000$ results in ambiguity to the true stellar He II EW. Overall, these fiducial fits confirm that two different VMS models are able to reproduce the GN-z11 continuum and wind features with a physically-motivated stellar metallicity and bubble size. Finally, we note that the $\mathrm{M25}_{\dot{\mathrm{M}},\mathrm{LMC}}$ models perform similarly as $\mathrm{M25}_{\dot{\mathrm{M}}\propto\mathrm{Z}}$ in reproducing the GN-z11 spectrum (Figure B1). The key difference is that the broad He II emission component is stronger (EW = 2.2 Å) than in the $\mathrm{M25}_{\dot{\mathrm{M}}\propto\mathrm{Z}}$ models (EW = 0.7 Å), as expected from the enhanced optically thick winds in the $\mathrm{M25}_{\dot{\mathrm{M}},\mathrm{LMC}}$ models at low metallicity. We note that our current measurement of He II is consistent with both values.

We now explore a wider range of stellar metallicities, with the goal of understanding how our choice of metallicity impacts our ability to reproduce the spectrum. We first consider CB19 models with a stellar metallicity of 0.1 $Z_\odot$ and 0.2 $Z_\odot$, 3-5 times larger than our fiducial model. We find that we are able to reproduce the spectrum at these metallicities with a goodness of fit (both with $\chi^2_\nu = 0.67$) comparable to our fiducial model. The key change of the larger stellar metallicity is stronger wind lines (see Figure B2 and B3). To reproduce the spectrum, the best-fitting model shifts slightly in its mixture of SSPs, with a single dominant age now at 3

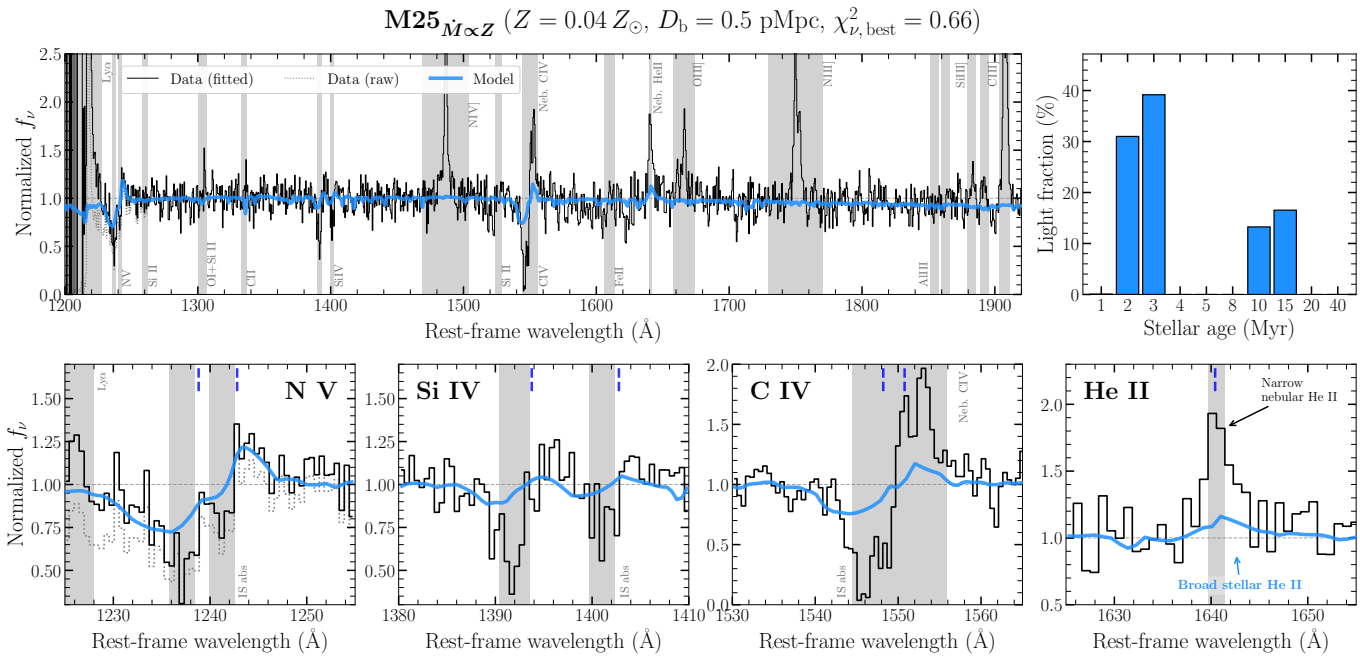

Figure 17. FiCUS fit to the UV continuum of GN-z11 using linear combinations of M25$_{\dot{\rm M}\propto{\rm Z}}$ SSP models. Shown are the fits to the observed spectrum corrected for IGM transmission, assuming a distance to the nearest neutral HI of 0.5 pMpc, and at a low metallicity of $Z* = 0.04\ Z_\odot$. **Top left**: The full UV continuum used for fit (black), the original observed spectrum before applying the correction for IGM transmission (dotted blue), and the best-fit model (red). Nebular emission lines and interstellar absorption lines are masked during the fit, which are shaded in gray. **Top right**: The star formation history corresponding to the best-fit model, parameterized as the light fractions of the UV continuum at 1360 Å as a function of SSP age. **Bottom**: Zoomed-in views of the FiCUS fits to the N V, Si IV, and C IV P-Cygni profiles, and broad stellar He II emission.

Myr. At these higher metallicities, the C IV absorption EW ranges from comparable to enhanced relative to the fiducial value (-0.8 Å at $0.1\,Z_\odot$ and -1.8 Å at $0.2\,Z_\odot$) given the additional age dependence, while stellar He II EW (1.5 Å at $0.1\,Z_\odot$ and 2.0 Å at $0.2\,Z_\odot$) is larger than in the fiducial models described above. Both remain consistent with the observed profiles. We find similar results when we fit the M25$_{\dot{\rm M}\propto{\rm Z}}$ models at larger metallicities. We conclude that the VMS models at stellar metallicity approaching that of the ionized gas are still consistent with the current GN-z11 spectrum.

We now explicitly consider how the fits are impacted by the assumed bubble size. While we expect small bubbles to be the norm at $z \simeq 10.6$ (see §6.3), it is possible that GN-z11 may be situated in an atypically large ionized region of the universe. As the assumed distance to the neutral IGM increases, the damping wing correction we apply is reduced, resulting in a stronger observed N V absorption profile. For example, to fit the spectrum with D_b=2 pMpc (instead of our fiducial 0.5 pMpc), we find a slight increase in the fraction of light from young SSPs in both CB19 and M25$_{\dot{\rm M}\propto{\rm Z}}$, specifically at ages $\lesssim$ 2 Myr for CB19 and $\lesssim$ 3 Myr for M25$_{\dot{\rm M}\propto{\rm Z}}$. And moving to bubble sizes smaller than our fiducial value shifts the age of the population toward slightly older SSPs. As a limiting case, we consider a highly neutral IGM with a very small ionized bubble (D_b=0.1 pMpc) around GN-z11. For both models, the stellar population shifts very slightly to older populations to fit the weaker observed N V absorption, but the best-fitting models are unable to reproduce the N V emission profile at a stellar metallicity of 0.04 $Z_\odot$. Increasing the stellar metallicity (0.1–0.2 $Z_\odot$) helps to match N V emission at D_b=0.1 pMpc, by shifting the stellar population to slightly older ages (now dominated by the SSP at 3 Myr), though we consider these metallicities are unlikely. Additionally, after correcting for the IGM damping wing, we recover excess flux in the data relative to the best-fit model from Lyα up to $\approx$ 1228 Å. This excess flux is suggestive of very broad Lyα emission. For both the CB19 and M25$_{\dot{\rm M}\propto{\rm Z}}$ models considered (assuming 0.04 $Z_\odot$ and $D_b = 0.5$ pMpc), we measure a total EW of 0.8–1.0 Å for this flux at $v > 2000$ km s^{-1}, increasing to 1.3–1.5 Å in the limiting case of a smaller bubble ($D_b = 0.1$ pMpc).

We also investigate the role of the upper end of the IMF on the quality of our fit to the spectrum of GN-z11. The models shown above assume an IMF including VMS extending up to 300 M$_\odot$. We now consider both CB19 and M25$_{\dot{\rm M}\propto{\rm Z}}$ models with IMFs that only include stars up to 100 M$_\odot$. In the case of the latter, the non-

VMS models are the BPASS single star models with an initial mass function slope of -2.35 above 0.5 $M_\odot$ as used in constructing the M25 population synthesis models (see § 6.1; J. J. Eldridge et al. 2017). Without VMS in the models, the stellar wind lines are generally weaker at fixed age and metallicity, and hence the metallicity, ages, and bubble sizes must be adjusted to fit the spectrum. For our fiducial stellar metallicity (0.04 $Z_\odot$) and bubble size (0.5 pMpc), the fits to the stellar wind lines are considerably worse without VMS for both CB19 and $\mathrm{M25}_{\check{\mathrm{M}}\propto\mathrm{Z}}$, with the N V emission component significantly underpredicted in both models (see Figure B4 and B5). The non-VMS models with stellar metallicity approaching that of the gas-phase still poorly fit the N V profile assuming our preferred small bubble size (0.5 pMpc). Only with very large bubble sizes ($\mathrm{D}_b > 2$ pMpc), which we consider unlikely, can the wind lines be reproduced with the non-VMS models we consider.

To summarize, we find that the rest-UV continuum and stellar wind lines in the SPURS GN-z11 spectrum can be simultaneously reproduced with stellar population models that have low stellar metallicities (0.04 $Z_\odot$) and small bubble sizes (0.5 pMpc) that we consider most likely. We find that the inclusion of VMS is very important and that the models we consider without stars more massive than 100 $\mathrm{M}_\odot$ struggle to fit the observed spectrum without very large bubble sizes and large stellar metallicities that we deem unlikely. However, we note that even among VMS models, there is a range of possible wind strengths that are accommodated by our data. Higher spectral resolution observations ($R = 2700$) should help distinguish between these scenarios, which in turn should better isolate the physics of the massive stars present in early nitrogen-enriched galaxy populations. Additionally, it is possible that the VMS included in current models may not appropriately capture the wind properties of the stars that form at low metallicity in dense environments like GN-z11. In the following section, we will consider whether the broad NIV] emission we have detected in GN-z11 may be a spectroscopic signature of such a population without clear precedent in population synthesis models or lower-redshift galaxy samples.

7. DISCUSSION

The depth of the SPURS spectrum provides new insight into two of the most surprising properties of GN-z11: its detectable Lyα emission at $z > 10$ and its extreme nitrogen enhancement. In this section, we first discuss what the resolved Lyα profile and interstellar absorption lines reveal about the escape of Lyα photons through the ISM, CGM, and neutral IGM (§7.1). We then turn to the physical origin of GN-z11's broad N IV] (§7.2) before concluding with a broader discussion about the role of massive stars and a possible AGN in shaping its properties (§7.3).

7.1. *Lyα Escape in $z > 10$ Galaxies*

GN-z11 is one of only two galaxies detected with Lyα emission at $z > 10$ (A. J. Bunker et al. 2023; J. Witstok et al. 2025). Prior to the launch of *JWST*, the IGM was expected to be almost fully neutral at $z > 10$ (e.g., C. A. Mason et al. 2018a; I. Jung et al. 2020; P. Bolan et al. 2022). At such high neutral fractions, ionized regions in the intergalactic medium are predicted to be small ($\lesssim 0.3$ pMpc, e.g., M. McQuinn et al. 2007; T.-Y. Lu et al. 2024; M. Neyer et al. 2024), strongly suppressing Lyα flux emerging from galaxies and making these detections surprising. It has not been clear whether these sources signpost early large ionized bubbles or reflect Lyα emission properties that facilitate transmission through the neutral IGM (e.g., S. Bruton et al. 2023; T.-Y. Lu et al. 2024; C. Cain et al. 2025; Y. Qin & J. S. B. Wyithe 2025; J. Cohon et al. 2026).

The SPURS spectrum provides new insights into what may boost the visibility of Lyα in GN-z11. The high SNR Lyα detection reveals a broad red wing, with 44% of the flux emerging at $> 500\,\mathrm{km\,s^{-1}}$ from line center. This red wing likely facilitates the transmission of Lyα flux through the neutral IGM. Due to the strong wavelength dependence of the Lyα damping wing optical depth from the neutral IGM, flux close to line center should be severely suppressed, while Lyα photons emerging from the galaxy at redder wavelengths experience much higher transmission (M. Dijkstra et al. 2011; C. A. Mason et al. 2018b; R. Endsley et al. 2022; Y. Yuan et al. 2025). Assuming typical distances of UV-bright galaxies to the neutral IGM at $z > 10$ from reionization simulations ($D_b \approx 0.2 - 0.5$ pMpc, T.-Y. Lu et al. 2024; M. Neyer et al. 2024, see § 6.3), the IGM damping wing transmission at $500\,\mathrm{km\,s^{-1}}$ is 16–32%, relative to just 0.3–7% at Lyα line center. Given GN-z11's minimal dust attenuation (§ 5.1) and strong UV and optical emission lines (§ 3), based on $z \sim 5-6$ samples with similar properties, we would expect strong emergent Lyα emission[16] (EW $\gtrsim 25$ Å, $f_{\mathrm{esc,Ly}\alpha} > 0.2$, e.g., M. Tang et al. 2024b). However, we observe a low Lyα EW ($5.6^{+0.2}_{-0.2}$ Å) and very low Lyα escape fraction ($f_{\mathrm{esc,Ly}\alpha} = 0.027^{+0.003}_{-0.003}$; § 5.2), indicating a large fraction of the emergent Lyα flux may be attenuated by the

[16] Here we define 'emergent' as the emission emerging from the galaxy if it resided in the ionized IGM, excluding the IGM damping wing attenuation.

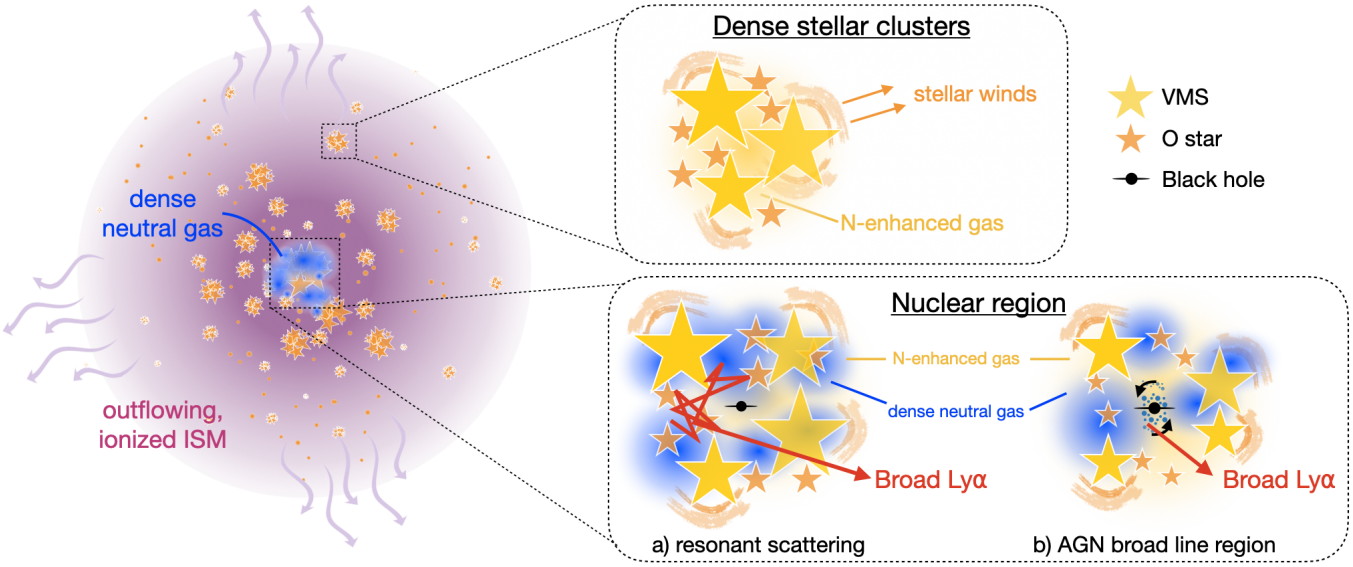

Figure 18. Schematic illustrating a potential qualitative geometry of GN-z11 that reconciles the observed Lyα emission tail at $> 500\,\mathrm{km\ s^{-1}}$ and OI* fluorescent emission with the weak low-ionization absorption lines (§ 7.1). We propose GN-z11 is composed of multiple dense stellar clusters, hosting young, massive stars, potentially including VMS (§ 7.3). The weak LIS absorption implies the dense neutral gas that is optically thick to Lyα and Lyβ is concentrated close to ionizing sources in a small volume of GN-z11, potentially around the innermost stellar clusters. In this nuclear region, Lyα may be broadened by a) resonant scattering in neutral gas with $N_{\rm HI} \gtrsim 10^{21}\,\mathrm{cm^{-2}}$. b) Keplerian motions in an AGN broad line region, if one is present. Meanwhile, the majority of the UV continuum is produced in stellar clusters at larger radii that have a low covering fraction of neutral gas.

IGM. This suggests that GN-z11 need not reside in a very large ($\gtrsim 1$ pMpc) ionized bubble, despite its potential location within an overdensity (S. Tacchella et al. 2023), but that its Lyα may be detectable in part due to a fraction of its flux emerging from the galaxy at $> 500\,\mathrm{km\,s^{-1}}$.

The presence of the red Lyα wing is, however, puzzling given the non-detection of low-ionization absorption lines in GN-z11 (§ 4). Producing significant Lyα flux at $>500\,\mathrm{km\ s^{-1}}$ via resonant scattering requires HI column densities $N_{\rm HI} \gtrsim 10^{21}\,\mathrm{cm^{-2}}$ (e.g., D. A. Neufeld 1990; A. Verhamme et al. 2006). If gas with this high column density covers a large fraction of the UV continuum emitting regions we should also expect metal absorption lines, given these lines are typically optically thick in star-forming galaxies (e.g., T. A. Jones et al. 2013; N. A. Reddy et al. 2016, 2022). If instead the metal lines are optically thin, this would imply significantly lower metallicities than the gas-phase metallicity we measure from the emission lines (based on the O I λ1302 EW lower limit implies $[\mathrm{O/H}] \lesssim -2.3$, or $12 + \log(O/H) \lesssim 6.39$, assuming a turbulent Doppler parameter of $b \gtrsim 20\ \mathrm{km\,s^{-1}}$), and is therefore unlikely unless the dense neutral gas is far from the H II regions. A key challenge is therefore reconciling the evidence for dense neutral gas in GN-z11 with the weak low ionization absorption lines.

The detection of O I*λ1304 emission in GN-z11 (Section 3) offers an important new insight into where this dense gas is located. We find the O I* emission is most plausibly explained via fluorescent excitation of neutral oxygen atoms by Lyβ, as suggested in AGN (J. Kwan & J. H. Krolik 1981; Y. Matsuoka et al. 2007) and LRDs (R. Tripodi et al. 2025a; M. Tang et al. 2026; X. Ji et al. 2026). Producing a high O I* flux requires both neutral gas which is very optically thick to Lyβ ($N_{\rm HI} > 10^{21}$, Y. Matsuoka et al. 2007) – consistent with the column densities required to produce the Lyα red wing – and a high Lyβ flux (J. Kwan & J. H. Krolik 1981). This suggests the presence of dense neutral gas very close to at least some of the ionizing sources in GN-z11.

One possibility is that only the nuclear star forming region is enshrouded in dense neutral gas, which we illustrate qualitatively in Figure 18. While we leave a detailed radiative transfer treatment to future work, Lyα photons produced in the nuclear region could resonantly scatter to $> 500\,\mathrm{km\ s^{-1}}$ in the high column density neutral gas, and Lyβ photons could excite a large enough population of OI atoms to produce significant fluorescent emission. If the majority of the far-UV emission arises from star forming regions exterior to the nuclear region, then the fraction of sightlines passing through the dense neutral gas would be low. This could explain the non-detection of low ionization absorption lines

in the UV continuum, and also contribute to Lyα flux closer to line center. A broad-line region (BLR) associated with an AGN in this region could also provide an explanation for the Lyα flux at $> 500\,\mathrm{km\,s^{-1}}$. In a BLR Ly$\alpha$ can be broadened to large velocities due to the Keplerian motion of gas. We discuss the potential origins of this geometry and presence of an AGN in GN-z11 further below (§ 7.3).

The deep GN-z11 spectrum thus provides critical context for understanding Lyα visibility at $z > 10$, including the most distant known Lyα detection, GS-z13-1-LA at $z \simeq 13$ (J. Witstok et al. 2025). GS-z13-1-LA is also expected to have a broad Lyα profile (FWHM$> 500\,\mathrm{km\ s^{-1}}$, J. Witstok et al. 2025, 2026), based on its detection in the low-resolution prism, but non-detection in current grating spectra. Our results suggest that these detections of Lyα emission at $z > 10$ are likely enhanced by a contribution from broad Lyα. We argue that the origin of this broadened Lyα emission is linked to the extreme nature of $z > 10$ galaxies: a consequence of star formation and evolution in very high density environments, and the potential presence of AGN. This has important implications for using Lyα to infer the onset of reionization. If such extreme conditions are common in $z > 10$ galaxies, the Lyα emerging from the ISM/CGM may be significantly different from that in the baseline $z \sim 5-6$ samples used to infer IGM attenuation (e.g., M. Tang et al. 2024b; G. Prieto-Lyon et al. 2025). Accurately inferring the properties of the IGM at the highest redshifts therefore requires a better understanding of the nature of $z > 10$ sources. Progress will require both detailed spectroscopy of analogs in the mostly ionized IGM at $z < 6$ (see e.g., S. Gagnon-Hartman et al. 2026, for an example), and larger samples of $z > 10$ sources with deep rest-UV spectroscopy to reveal their detailed gas conditions and obtain a census of Lyα at the highest redshifts.

7.2. *The Origin of Broad N IV] in GN-z11*

The physics responsible for nitrogen-enhancements in a subset of early galaxies remains unclear. Some have argued the strong winds of very massive stars (e.g., J. S. Vink 2023; Y. Shi et al. 2026) or supermassive stars (e.g., C. Charbonnel et al. 2023; C. Nagele & H. Umeda 2023; M. Gieles et al. 2025) may drive nitrogen-enhanced material into the ISM prior to supernovae, but other explanations exist (e.g., C. Kobayashi & A. Ferrara 2024; W. McClymont et al. 2026). Distinguishing between these pictures will require direct constraints on the stellar populations in nitrogen-enriched galaxies. A first step in this direction was provided by D. A. Berg et al. (2026), with a deep rest-optical spectroscopy revealing strong winds in broad He II λ4687 together with strong N III λ4642 emission, attributed to a population of WN stars formed following a strong burst of star formation.

The spectrum of GN-z11 provides another opportunity to study the massive star populations associated with nitrogen emitters. SPURS observations reveal a broad N IV]λ1486 component which may be related to the physics driving the nitrogen-enhancements. In addition to GN-z11, we identify broad N IV] emission in two other $z > 8$ galaxies known to have strong narrow N IV] emission: EGSY8p7 ($M_{\mathrm{UV}} = -22.1$, $z = 8.687$; R. L. Larson et al. 2023; Y. Isobe et al. 2023; R. Marques-Chaves et al. 2024; M. W. Topping et al. 2025a; L. Whitler et al. 2026), and GNz9p4 ($M_{\mathrm{UV}} = -21.0$, $z = 9.380$; D. Schaerer et al. 2024; M. W. Topping et al. 2025a). In Figure 19, we show their resolved N IV] profiles based on the SPURS data (Chen et al. in prep, Owens et al. in prep), along with the stacked N V profile based on all three sources, highlighting their similarities. We find a broad N IV] λ1486 component ($1265^{+69}_{-69}\,\mathrm{km\,s^{-1}}$ in EGSY8p7 and $1078^{+236}_{-236}\,\mathrm{km\,s^{-1}}$ in GN-z9p4).

The discovery of this broad NIV] component in the first three nitrogen emitters with ultra-deep rest-UV spectroscopy suggests its origin may be somewhat common in strong N IV]-emitting galaxies, motivating a closer investigation of the physics driving this line. N IV] λ1486 is routinely powered in broad Wolf-Rayet emission in dense stellar winds, most prominently in atmospheres of the WN sequence — from very massive stars on the hydrogen-burning main sequence (and so with significant residual hydrogen; WNh) to hydrogen poor, fully stripped WNE stars. Its strength is generally a complex function of wind density, ionization structure, and composition. This line and the permitted N IV λ1719 are the two strongest stellar lines from triply-ionized nitrogen in the UV. While λ1719 is permitted, it is a transition between the excited $2p$ up to the $2p^2$ configuration; whereas while λ1486 is semi-forbidden, it is connected to the $2s^2$ ground state of N IV. Both lines are prominent in nitrogen-rich and moderately hot WR atmospheres, at effective temperatures ranging from $\sim$ 40–80 kK (above and below this range, N V and N III become dominant, respectively; though the resonant N V $\lambda\lambda 1238, 1242$ is prominent throughout this range as well).

For many WR atmospheres, N IV λ1719 is stronger than N IV] λ1486 (e.g. P. A. Crowther et al. 1995; P. A. Crowther & L. J. Smith 1997; R. Hainich et al. 2014). However, this is not uniformly true, with the ratio between these lines varying substantially across different atmospheres. In the PoWR WN grids for example, at-

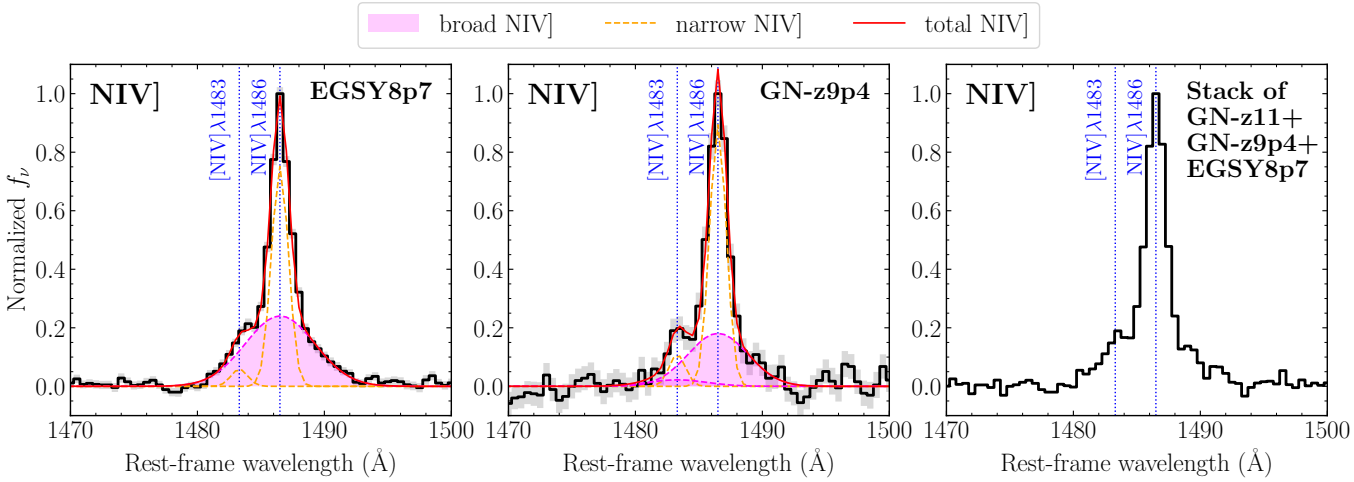

Figure 19. N IV] emission line profiles of EGSY8p7 (left), GN-z9p4 (middle), and the stacked N IV] spectrum of GN-z11, EGSY8p7, and GN-z9p4 (right). We also show the best-fit models to the N IV] profiles of EGSY8p7 and GN-z9p4. Similarly to the N IV] profile of GN-z11, the N IV] lines of both EGSY8p7 and GN-z9p4 are best-fitted by narrow N IV] components (orange dashed lines) plus broad N IV] components (magenta shaded regions).

mospheres at fixed $T_{\rm eff}$ and smaller transformed radii R_t (corresponding in turn to some combination of denser, higher $\dot{M}$, and slower winds) tend to have larger λ1486 relative to λ1719 features (up to a limit above which both N IV features disappear); with λ1486 actually becoming dominant for some models at $\sim$ 40–60 kK and $R_t \sim$ 5–10 $R_\odot$. To understand why this ratio varies with wind properties at fixed temperature, it is important to first understand how these lines are excited in detail. The N IV] λ1486 line is directly connected to the ground state and is relatively low-lying, and its emission is predominantly powered by collisional excitation in typical WN atmospheres (and thus also serves as an important coolant, e.g. D. J. Hillier 1988, 1989; J. G. Rivero González et al. 2012). It is typically formed at densities near or above its critical density of $10^{10.5}$ cm^{-3} within WN atmospheres (and near where emission in C IV originates). In contrast, N IV λ1719 begins at an upper level significantly above ground ($\sim$ 23.4 eV) and has a weak collisional coupling to the $2s^2\,{}^1S$ ground state; and thus while collisional excitation from other levels does likely contribute to and in many cases dominate the population of its upper level, other effects including continuum fluorescence and potentially dielectric recombination also likely contribute to its formation depending on temperature, density, and the radiation field (D. J. Hillier 1988). Crucially, these differences mean that the relative strength of these lines can be sensitive to differences in the radial density and temperature structure of flows in which they are formed.

As a simple experiment, we show in the top panel of Figure 20 the effect of adding an additional WN atmosphere with particularly prominent N IV] λ1486 to the fiducial stellar population synthesis model presented in Section 6.4. The additional WN contribution is a single atmosphere chosen from the PoWR grids specifically as a visually close approximation of the observed line strengths at relatively low metallicity: an SMC WNe star at $T_\star = 40$ kK and $\dot{M} = 10^{-4.5}$ M$_\odot$/yr, with transformed radius $R_t = 10\ R_\odot$ near to the upper end of the wind strength distribution for the SMC grid (G. Gräfener et al. 2002; W.-R. Hamann & G. Gräfener 2004; A. Sander et al. 2015; H. Todt et al. 2015). Note that similar models can be found at higher metallicities and could likely be found at lower-Z as well at sufficiently high mass loss rates and wind densities; we plan to more fully explore this parameter space with dedicated modeling in future work. This is added to the CB19 composite fit by fitting simple scaling factors for the two models and a separate extinction correction for the WN atmosphere, and compared to the IGM-corrected restframe spectrum (assuming the fiducial 0.5 pMpc bubble). The addition of this atmosphere at a $\sim$ 35% flux contribution in the UV introduces significant broad emission in N IV] λ1486 which matches the observed pedestal closely. This likewise significantly strengthens the model profiles of N V, C IV, and He II, bringing the emission components of each and the deepest absorption in the latter two into closer agreement with the data. This is particularly striking for N V, where the resolved components of the doublet in absorption are reasonably well approximated by the addition of this atmosphere. Indeed, this wind (even for an essentially fully stripped atmosphere) does also produce some flux in Lyα with similar profile to the observed red wing; though at lower total flux than observed. The

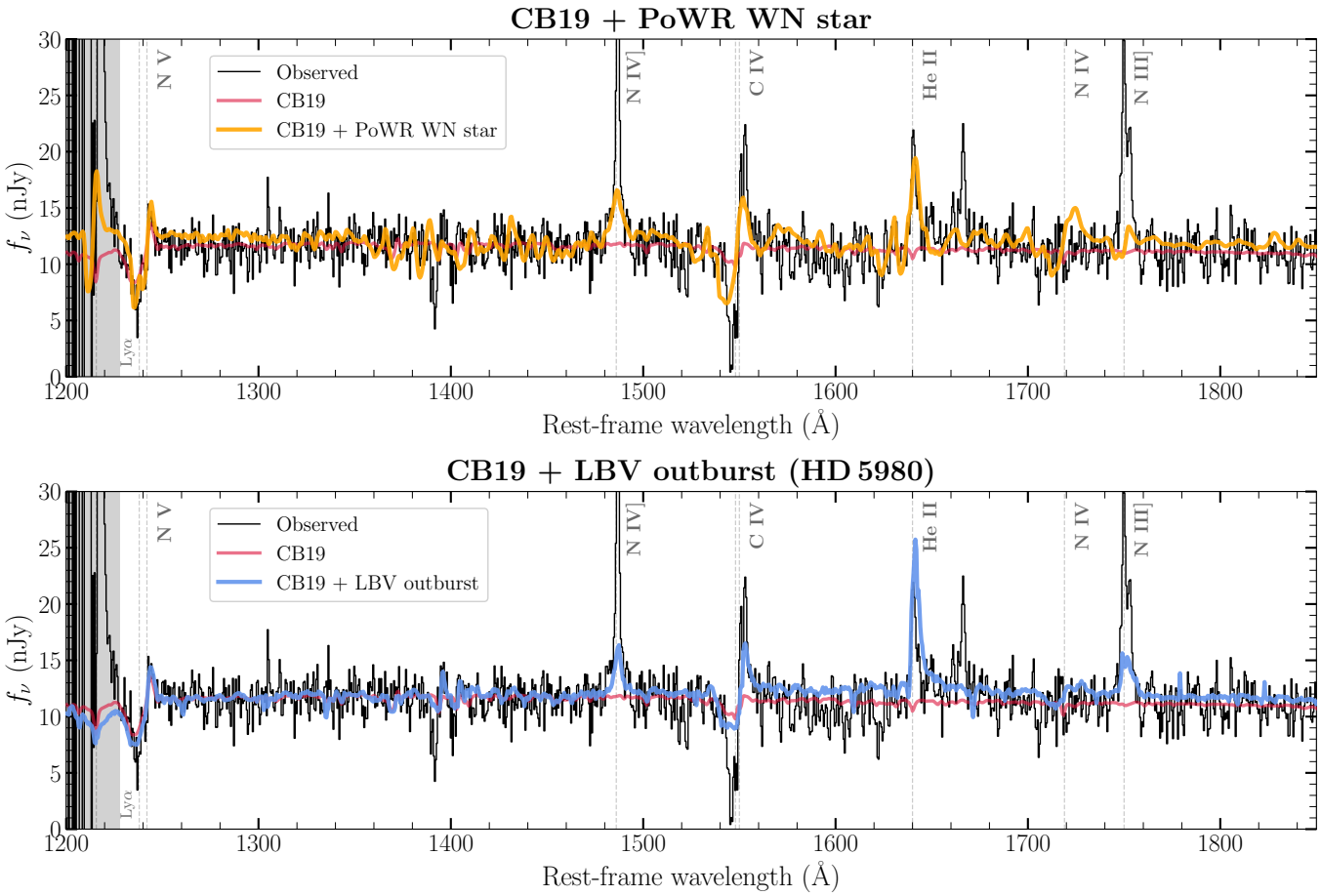

Figure 20. Similarities between the observed GN-z11 spectrum and models adding a WN atmosphere with a particularly prominent N IV] λ1486 (top panel), or the outburst of the SMC LBV HD 5980 (bottom panel) to the UV continuum. In each panel, we show the GN-z11 spectrum after correcting for damping-wing transmission assuming an ionized bubble of $D_b = 0.5$ pMpc in black, and the fiducial CB19 stellar continuum model ($Z_* = 0.04 Z_\odot$) from § 6.4 in red. The top panel also shows, in an orange line, a composite model adding to the CB19 model a WN atmosphere (a single atmosphere from the PoWR grids at 40 kK; see text) renormalized to contribute 35% of the UV continuum. The bottom panel presents a second composite model, in a blue line, where we add the UV spectrum of HD 5980 in April 1995, an unusually hot LBV outburst from a massive WN star in a WN+WN+O triple in the SMC, renormalized to contribute 13% of the UV continuum. The addition of either the WN atmosphere or the LBV outburst spectrum produces a prominent broad N IV] λ1486 emission in agreement with the data, while the N IV λ1719 emission remains weaker than N IV] λ1486.

N IV λ1719 in this model is the largest source of tension; while minimal, the predicted P-Cygni does still rise just above the noise in the continuum.

The reasonably good agreement between this very simplified model combination and the data is suggestive of an unusual stellar population. This model suggests that a strong contribution to the UV from a population of WR atmospheres with particularly dense and relatively low-temperature winds could potentially help explain the broad N IV], the broad He II, and the narrower P-Cygni components of N V. Such WN atmospheres are broadly expected as products of a variety of processes of stripping and spin-up (particularly in binaries or other interacting systems) which can expose a hydrogen or helium burning core, rich in nitrogen and luminous enough to drive a dense enriched wind. However, this would require a substantial number of such stars. The total luminosity of this added component is of-order 10^{10}–10^{11} $L_\odot$: thus requiring of-order 10^4–10^5 'ordinary' ($\lesssim 10^6$ $L_\odot$) massive stars in this phase to explain. In addition, the winds of these stars would need to be fairly self-similar to produce a composite spectrum with such strong N IV] and coherent low-velocity features in the other lines; as implied by the discussion of the PoWR grid above, much deviation from a fairly narrow temperature and mass loss range and the spectrum would change substantially, weakening N IV] λ1486 and/or strengthening the contribution of other lines. It is possible that this is the prod-

uct of catching a VMS population in a common phase, perhaps stripped by a very high rate of interactions in a dense cluster or spun-up to evolve in a chemically homogeneous manner, and that the winds such stars are capable of driving at low metallicity might be confined to relatively low velocities and high densities. Especially at very low metallicities where strong stellar winds in general require stars close to the Eddington limit, we are increasingly likely to see the impact of the most massive stars (with the highest L/M) present in these lines; and models for the evolution and atmospheres of these stars at low metallicity with or without binary interaction remain highly uncertain (e.g. K. Köhler et al. 2015; A. A. C. Sander & J. S. Vink 2020; D. Szécsi et al. 2025).

Atmospheres like this model are not common in the Local Group; but interestingly, there is a singular object in the SMC with some remarkable spectral similarities worth drawing attention to. HD 5980 is an (at least) triple system consisting of two emission-line early WN stars in a close orbit with an O-type tertiary; one of the most luminous systems in the SMC and situated on the outskirts of the standout young star forming region NGC 346 (G. Koenigsberger et al. 2014; T. Shenar et al. 2016). In 1994–1995 one of the WN components of this eclipsing system underwent a luminous outburst generally considered to be a Luminous Blue Variable (LBV) giant eruption, but unusual in both its high luminosity and its exceptionally high temperature (∼WN7–11 at visual maximum, 20-40 kK, much hotter than typical LBV temperatures in-outburst which rarely exceed ~ 8000 K; and with estimated luminosity $\sim 10^{6.5}$–10^{7} $L_{\odot}$; G. Koenigsberger et al. 1994; G. Koenigsberger et al. 1995; G. Koenigsberger & E. Moreno 1997; A. F. J. Moffat et al. 1998; L. Drissen et al. 2001; L. Georgiev et al. 2011; J. S. Vink 2012; K. Weis & D. J. Bomans 2020). The resulting UV spectrum near peak outburst taken by IUE (April 1995; IUE PID:WRRGK, PI:Koenigsberger) shows some striking similarities to the UV spectrum of GN-z11 (as also noted by Nakane et al. 2026): with very prominent N IV] λ1486 (and N III] $\lambda\lambda$1750), weak λ1719, and low-velocity absorption in N V, C IV, and Si IV (G. Koenigsberger et al. 1995; L. Georgiev et al. 2011). Following the same procedure as for the PoWR atmospheres, we add this spectrum, renormalized to contribute 13% of the UV continuum, to the composite CB spectrum in the bottom panel of Fig. 20 to highlight these similarities. While its properties stand out in the pantheon of LBVs and the precise nature of its outburst cycle remains enigmatic, it is likely that the close binary plays a crucial role; potentially involved in the triggering of the outburst in the first place (e.g. J. S. Gallagher 1989; N. Smith et al. 2011; S. Justham et al. 2014), and perhaps responsible for shaping the typically dense and cold outer layers of the outflowing ejecta and explaining its high $T_{\rm eff}$ (e.g. G. Koenigsberger & E. Moreno 1997; A. F. J. Moffat et al. 1998; G. Koenigsberger et al. 2010). While our observations and understanding of LBVs at low metallicity and in close binaries are limited, HD 5980 could reasonably be considered a prototype for LBV-like near Eddington mass eruptions for multiple systems of very massive stars in dense and low metallicity environments, which like 'classical' LBV events might be expected to be broadly self-similar (interestingly, arguably the closest analogs to HD 5980 are two events in M33 at sub-LMC metallicity: O. Maryeva et al. 2019; N. Smith et al. 2020). It is suggestive then that spectral features approximated by this event might appear underlying the N-rich nebular spectrum in these high-redshift galaxies; a large number of such luminous eruptive mass loss events, if somehow triggered at very low-Z (potentially aided or driven by interactions with close companions in hardened binaries), would naturally eject very large quantities of N-rich material from CNO cycle hydrogen burning into the ISM at low velocities and temperatures where it might rapidly be integrated into the nebular phase.

Another possibility is that rather than a population of stars with similar winds, we are observing a small number or even a single dense outflow against an extraordinarily luminous central object. This would need to be an extremely compact system; a simple estimate of an effective radius from the 40 kK effective temperature and implied total luminosity of this component suggests $R_{\rm eff} \simeq 10$–30 AU scales (10^{-5}–10^{-4} pc), two orders of magnitude smaller than those implied in LRDs (while their luminosities are comparable, the high effective temperature required here necessitates a substantially smaller size; e.g. J. Chisholm et al. 2026) and an order of magnitude smaller than even small measured BLR sizes (of-order light-days or larger; e.g. S. Kaspi et al. 2005; M. C. Bentz et al. 2013; GRAVITY Collaboration et al. 2024; J.-H. Woo et al. 2026). This is qualitatively consistent with the fact that this broad N IV] emission is superimposed by a very narrow component, which is likely associated given the rarity of the required N/O-enhanced gas; in that case, this narrow component must reside outside this optically thick outflow, and larger extended geometries introduce some tension with the implied kinematics of this near stationary narrow line gas. Any central engine near the Eddington luminosity would require a mass of at least 10^{5}–10^{6} $M_{\odot}$, or substantially more luminous N IV] emission than achieved by these stellar models. It would also naturally require a very high N/C and N/O ratio to explain

the observed line ratios. An extended atmosphere as potentially allowed by such an extreme scenario may also resolve some tension with lines like N IV λ1719, which are likely to be further suppressed in atmospheres where the incident photon density and gas density is further reduced (as is likely the case for HD 5980). At the implied scales, such a central engine is suggestive of a luminous accretion disk or supermassive star, surrounded by gas which it is driving away in an LBV-like near-Eddington state.

Despite the suggestive compatibility of their velocities, the broad N IV] λ1486 emission may also be unrelated to the broad absorption component of N V and C IV and the emission in He II, and instead emerge separately from a highly enriched broad line region in emission. This would naturally explain the absence of strong N IV λ1719 which is not observed in AGN or generally outside of dense stellar atmospheres. While N IV] λ1486 is a prominent collisionally excited line in the rare subset of nitrogen loud quasars, these systems also typically show prominent broad emission in N V $\lambda\lambda$1238, 1242 and N III] $\lambda\lambda$1750; with the latter two lines comparably or significantly stronger than N IV] (J. A. Baldwin et al. 2003; L. Jiang et al. 2008; K. Matsuoka et al. 2017). While in this case the N V profile is complex, we don't see clear evidence for strong broad emission at similar FWHM on the red side of the P-Cygni profile in excess of the putatively stellar component; and N III] shows no clear evidence for a strong broad component. Such a N IV]-dominated BLR might be possible, but would likely require particular temperature and density conditions not achieved in the known nitrogen-loud quasar distribution; and if indeed not associated with the outflow lines, would necessitate even deeper absorption lines from the stellar component to compensate for the additional continuum contribution implied.

7.3. *New Insight into Physical Nature of GN-z11*

As the most luminous galaxy known at $z > 10$, GN-z11 provided our first indications of an extraordinary galaxy population at cosmic dawn already in the HST-era (P. A. Oesch et al. 2016). Its extreme luminosity makes it our best laboratory to understand the physical conditions in UV-bright galaxies at these redshifts. NIRCam imaging demonstrated its light is dominated by an extremely compact ($r_{1/2} = 64 \pm 20$ pc) component containing $\sim 10^{8.4}\,M_\odot$ of stars (S. Tacchella et al. 2023), hinting at an unusually dense mode of star formation. The discovery imaging and spectrum reveal a rising star formation history, with half of the stellar mass building up in the $\simeq 10$ Myr prior to observation (S. Tacchella et al. 2023; A. J. Bunker et al. 2023).

The SPURS spectrum sharpens this picture. Detection of multiple stellar P-Cygni wind features provides a direct view of the massive star populations present in GN-z11, with the strong NV feature in particular providing a higher definition view of the recent star formation history. We showed in §6.4 that reproducing the NV absorption and emission requires a significant fraction of the UV continuum ($\simeq 2-3$ Myr) arises from very young stellar populations. In the context of these models, the extreme UV continuum luminosity of GN-z11 is driven by the recent burst of star formation.

The nature of the massive stars in GN-z11 holds important clues as to the origin of the nitrogen-enhanced abundance pattern. In sufficiently dense, low-metallicity stellar systems, VMS are expected to assemble through runaway collisions and stellar mergers (e.g., S. F. Portegies Zwart & S. L. W. McMillan 2002; M. Freitag et al. 2006; S. Goswami et al. 2012; M. S. Fujii & S. Portegies Zwart 2013). Recent star-by-star simulations of hierarchical cluster assembly support this picture, following the formation of massive clusters through the merging of ~ 1000 sub-clusters and finding that VMS are efficiently assembled through repeated collisions of massive stars within them (A. Rantala et al. 2024, 2026). These simulations indicate that the channel operates for cluster half-mass surface densities above $\Sigma_{\rm h} \gtrsim 10^4 - 10^5\,M_\odot\,{\rm pc}^{-2}$ and metallicities below $Z \lesssim 0.2\,Z_\odot$. While we cannot constrain the densities of individual clusters in GN-z11, its extreme compactness ($r_{1/2} = 64$ pc) and low stellar metallicity place it plausibly within this regime. Our analysis in §6.4 suggests that VMS may be present in GN-z11, powering the stellar wind features observed in the UV spectrum. In §7.2, we demonstrated that the broad NIV]λ1486 emission may be powered by the winds of VMS or possibly LBV-like outbursts in GN-z11 and other nitrogen emitters, with the strength of this feature and other narrow wind lines and the absence of NIVλ1719 offering a first hint that we may be witnessing a stellar population without direct analog at later epochs, plausibly shaped by the lower-metallicity, denser conditions of the early universe.

If VMS are present in GN-z11 and other nitrogen emitters, simulations predict they may naturally seed IMBHs. In particular, simulations of hierarchically assembling star clusters predict that IMBHs form via stellar collisions in the centers of individual sub-clusters, and are subsequently carried toward the center of the host system as the sub-clusters themselves sink and merge (M. S. Fujii & S. Portegies Zwart 2013; A. Rantala et al. 2024, 2026). The collisionally grown stars collapse after $\simeq 2.5 - 5$ Myr, comparable to the age of the burst inferred in §6.4, so IMBH formation may plausibly be

underway in GN-z11; their assembly into a single nuclear black hole would follow on the longer timescale over which the cluster system merges. Independently, based on the O I*λ1304 and broad Lyα features (§7.1) we have suggested that GN-z11 may harbor a dense reservoir of neutral gas in its nuclear region. This is exactly the environment in which such a black hole would be expected to rapidly grow in mass (e.g., K. Inayoshi et al. 2020).

Previous work has hinted at the possibility that GN-z11 hosts an AGN (R. Maiolino et al. 2024). We can reconsider this evidence in light of the new observations. The SPURS data confirm the presence of fast ionized outflows in GN-z11, as also noted by R. Maiolino et al. (2024). While the high ionization absorption lines have contribution from stellar winds, we find that the troughs in the interstellar absorption lines are near $\approx 500\,\mathrm{km\,s^{-1}}$ (Section 4), at the extreme end of what is found in star-forming galaxies (e.g., J. Chisholm et al. 2015; T. M. Heckman & S. Borthakur 2016; X. Xu et al. 2022). In contrast, such high velocities are commonly seen in UV absorption lines of AGN (e.g., K. N. Hainline et al. 2011). However, the evidence in favor of an AGN is not conclusive. The electron densities inferred from N IV] and N III] do not require BLR-like densities, though uncertainties still permit high densities from the N III] ratios (Section 5.3). We do not detect the [Ne IV] emission that is present in the discovery spectrum (R. Maiolino et al. 2024; M. Tang et al. 2025), although we note that the absence of very high ionization lines is common in many AGN discovered by *JWST* at very high redshift (e.g., M. Tang et al. 2025; J. Scholtz et al. 2025; E. Lambrides et al. 2026). Most importantly, if GN-z11 hosts a broad-line AGN, we should see broad Balmer lines, which have not been detected in the current NIRSpec and MIRI spectroscopic observations. However, as discussed in § 3.10, if the broad-to-narrow Balmer ratio is similar to that in EGSY8p7, which does show broad rest-frame optical lines (R. L. Larson et al. 2023; S. Zamora et al. 2025) as well as broad N IV] (Figure 19), both the broad Hγ and broad Hα components would be below the sensitivity limit of current observations. Deeper rest-frame optical spectroscopy will thus be critical for providing further constraints on the presence of an AGN in GN-z11.

Finally, we consider how these results connect to the LRD population, which shares both nitrogen enhancement (e.g., I. Labbe et al. 2024; I. Morel et al. 2025; R. Tripodi et al. 2025b) and evidence for Lyβ-pumped O I emission with GN-z11 (e.g., R. Tripodi et al. 2025a; V. Kokorev et al. 2026; M. Tang et al. 2026). One explanation is simply that both are powered by dense stellar systems in which massive stars are efficiently assembled. But the same conditions may link the two populations more directly: if intense bursts build dense clusters that form VMS, and those VMS in turn seed IMBHs, then the star formation episodes producing objects like GN-z11 may also be efficient black hole seeding sites. Whether such a phase may precede an LRD phase, with the seeded black hole subsequently growing in the dense nuclear gas, or alternatively follow one, after feedback has cleared much of the obscuring material, is unclear. Regardless, the conditions required to seed a central black hole appear to be in place in GN-z11.

8. SUMMARY

We present new ultra-deep $R \sim 1000$ JWST/NIRSpec spectroscopy of GN-z11, the most UV-luminous galaxy confirmed at $z > 10$, obtained as part of the SPURS Cycle 4 Large Program. The observations provide the deepest rest-UV view yet obtained of a galaxy at $z > 10$, and offer new insight into two of GN-z11's most surprising properties: its extreme nitrogen enhancement and its detectable Lyα emission. The ultra-deep spectrum provides, for the first time, a direct view of the massive star population responsible for the nitrogen enrichment through stellar wind diagnostics, while the well-resolved Lyα profile sheds new light on how Lyα photons are able to be transmitted through a still largely neutral IGM at these redshifts. We note, an independent analysis of the SPURS spectrum is presented by Nakane et al. (2026). We summarize our findings as follows.

1. The deep medium-resolution G140M spectrum detects and resolves the Lyα velocity profile at high S/N. The Lyα profile is asymmetric, with the observed flux peak offset from systemic by $418^{+12}_{-14}\,\mathrm{km\,s^{-1}}$ and a broad wing at $> 500\,\mathrm{km\,s^{-1}}$ that contributes 44% of the total flux. We measure a small Lyα EW ($5.6^{+0.2}_{-0.2}$ Å) and a low escape fraction ($f_{\mathrm{esc,Ly\alpha}} = 0.027^{+0.003}_{-0.003}$). The broad red Ly$\alpha$ wing at $> 500\,\mathrm{km\,s^{-1}}$ likely boosts the transmission of Lyα flux through the IGM damping wing.

2. We detect the UV continuum at very high S/N (8.5 in G140M), allowing us to characterize interstellar absorption lines. We find strong blueshifted absorption from high-ionization lines (N V, Si IV, and C IV), suggesting fast ionized outflows with velocities centered at $\sim 500\,\mathrm{km\,s^{-1}}$. In contrast, the low-ionization absorption lines are not detected (typical EW limit of > -0.3 Å at 3σ), indicating a low covering fraction of neutral gas which should facilitate the escape of Lyα photons through the ISM/CGM.

3. The broad Lyα emission we detect may be crucial for understanding why Lyα is seen at all at $z > 10$. However, we point out that the observed flux at $> 500\,\mathrm{km\,s^{-1}}$ is difficult to reconcile with the weak low-ionization ab-

sorption lines, which suggest little neutral gas is available to scatter Lyα to these velocities. The SPURS spectrum detects the O I*λ1304 fine-structure emission line that offers a resolution. This line requires dense neutral gas close to a subset of the ionizing sources in GN-z11, that is both optically thick to Lyβ and exposed to a high Lyβ flux. Gas at such high column densities will also resonantly scatter Lyα to the large velocities we observe. Given the weak LIS absorption, we suggest this dense neutral gas is confined to a compact nuclear region, with the bulk of the UV continuum arising from surrounding star-forming regions. This demonstrates that a more detailed understanding of the gas conditions in early galaxies, and a larger census of $z > 10$ Lyα, will be important for more accurately inferring properties of the IGM at these redshifts.

4. We detect many emission lines throughout the UV (N IV], C IV, He II, O III], N III], Si III], C III]), providing constraints on electron density, temperature, and gas-phase abundance pattern. Our results are consistent with those inferred from the JADES discovery spectrum, indicating extreme conditions in the H II regions of GN-z11. We find that the ionized gas is characterized by very high electron densities (2.5×10^4 cm^{-3} up to $> 7.9 \times 10^5$ cm^{-3}), a hot electron temperature ($1.3^{+0.1}_{-0.1} \times 10^4$ K), and a low gas-phase oxygen abundance ($12 + \log(\mathrm{O/H}) = 7.94^{+0.14}_{-0.14}$), along with an enhanced N/O ratio relative to solar ($3.9^{+0.8}_{-0.5}$ $(\mathrm{N/O})_\odot$).

5. The rest-UV continuum spectrum constrains a suite of features (N V, Si IV, C IV, and He II) tracing winds from massive stars. In particular, we find the N-V P-Cygni feature is very strong, even after accounting for the contribution of IGM damping wing attenuation. We perform stellar continuum fitting with a variety of stellar population synthesis models, including those with updated treatments of VMS. We find that the far-UV continuum and stellar wind features can be reproduced by models that have the low stellar metallicity ($0.04\ Z_\odot$) and small ionized bubble sizes ($\lesssim 0.5$ pMpc) that we consider most likely for GN-z11. To reproduce the strong N-V feature, the models require a significant population of very young stars (≤ 3 Myr) contributing significantly to the UV continuum. We show that a population of VMS plays an important role in reproducing the observed spectrum.

6. We show that GN-z11 exhibits broad N IV] emission, with FWHM = 1670 km s^{-1} centered at the wavelength of the N IV] λ1486 component. We demonstrate that this broad NIV] component is seen in several other nitrogen emitters at $z \gtrsim 9$. Broad N IV] emission is often seen in WN stars, but usually alongside a stronger N IV λ1719 line, which is not seen in our data. We demonstrate that strong broad N IV] λ1486 with very weak N IV λ1719 may nonetheless arise from dense and relatively low-temperature WN winds or LBV-like outbursts plausibly associated with a population of VMS in a dense cluster environment. However, a wind driven by an AGN or supermassive star, potentially seeded by an earlier VMS population, cannot be excluded. This broad component may trace the mass outflows responsible for GN-z11's nitrogen enhancement.

While prism spectra provided our first indications of the extreme emission features of bright $z > 10$ galaxies, UV grating spectra of this depth provide our first direct view of the underlying massive star populations forming under the extreme conditions of the early universe. Spectra like this of GN-z11 open a unique window onto massive stars at the low metallicities and high densities characteristic of the earliest star-forming clusters, potentially shedding light onto otherwise challenging to constrain stellar astrophysics and providing a stress test for the next generation of stellar population synthesis models. Larger samples with deep rest-UV spectroscopy promise to reveal whether such stellar populations are common among $z > 10$ galaxies, and what physical conditions drive their emergence.

ACKNOWLEDGMENTS

The authors thank Andrew Bunker, Alex Cameron, Paul Crowther, and Max Gronke for helpful conversations, Stéphane Charlot and Jacopo Chevallard for providing access to the Beagle tool, and Fabrice Martins for sharing their population synthesis models. ZC acknowledges support by VILLUM FONDEN under grant 37459. CAM acknowledges support by the European Union ERC grant RISES (101163035), Carlsberg Foundation (CF22-1322), and VILLUM FONDEN (37459). MT acknowledges support by a Shanghai Jiao Tong University start-up grant. KVGC is supported by NASA through the STScI grants JWST-GO-03777, JWST-GO-04265, and JWST-GO-05974. LW acknowledges support from the Gavin Boyle Fellowship at the Kavli Institute for Cosmology, Cambridge and from the Kavli Foundation. VG acknowledges support by the Carlsberg Foundation (CF22-1322). The Cosmic Dawn Center (DAWN) is funded by the Danish National Research Foundation under grant DNRF140.

This work is based in part on observations made with the NASA/ESA/CSA JWST. The data were obtained from the Mikulski Archive for Space Telescopes at the Space Telescope Science Institute, which is operated by the Association of Universities for Research in Astronomy, Inc., under NASA contract NAS 5-03127 for

JWST. These observations are associated with program GTO 1181 (JADES; M. Rieke et al. 2023) and GO 9214 (SPURS). The authors acknowledge the JADES team for developing their observing program. The authors thank the GO 9214 program coordinator, Christian Soto, and NIRSpec reviewer, Diane Karakla. Some of the data products presented herein were retrieved from the Dawn JWST Archive (DJA). DJA is an initiative of the Cosmic Dawn Center (DAWN), which is funded by the Danish National Research Foundation under grant DNRF140. The Tycho supercomputer hosted at the SCIENCE HPC center at the University of Copenhagen was used for supporting this work.

Facilities: JWST(NIRSpec)

Software: ASTROPY:[17] a community-developed core Python package and an ecosystem of tools and resources for astronomy (Astropy Collaboration et al. 2013, 2018, 2022); BEAGLE (J. Chevallard & S. Charlot 2016); EMCEE (D. Foreman-Mackey et al. 2013); FICUS (A. Saldana-Lopez et al. 2023); JUPYTER (T. Kluyver et al. 2016); MATPLOTLIB (J. D. Hunter 2007); MSAEXP (G. Brammer 2023); NUMPY (C. R. Harris et al. 2020); SCIPY (P. Virtanen et al. 2020).

APPENDIX

A. BIC ANALYSIS OF EMISSION LINE FITTING

The N IV], N III], C III], and O III] emission lines of GN-z11 show complex profiles with multiple components. To interpret each of these lines, we fit the line profile with a few different models. We evaluate the goodness of fit of each model using the Bayesian Information Criterion (BIC; G. Schwarz 1978; A. R. Liddle 2007). According to A. R. Liddle (2007), the BIC of each model fit is defined as

$$\mathrm{BIC} \equiv -2\ln\mathcal{L} + k\ln N, \tag{A1}$$

where $\mathcal{L}$ is the maximum likelihood achievable by the model, k is the number of parameters of the model, and N is the number of data points used in the fit. To calculate the maximum likelihood, we assume independent Gaussian uncertainties, obtaining

$$\mathcal{L} = \prod_{i=1}^{N} \frac{1}{\sqrt{2\pi}\sigma_i} \cdot \exp\left[-\frac{(f_i - m_i)^2}{2\sigma_i^2}\right], \tag{A2}$$

where f_i and σ_i are the observed flux density and its uncertainty of the ith data point in the spectrum to fit, and m_i is the best-fit model value of the ith data point. When comparing between two models, we take ΔBIC > 10 as very strong evidence that the model with the lower BIC provides a better fit to the data than the other.

The SPURS deep G140M spectrum of GN-z11 reveals the detection of a broad N IV]λ1486 component. Motivated by this, we simultaneously fit the entire N IV] profile with two narrow Gaussians and one broad Gaussian. Here we fix the centroids of the two narrow Gaussians to the rest-frame wavelengths of [N IV]λ1483, N IV]λ1486, respectively. For the broad component, we fix the centroid to the rest-frame wavelength of N IV]λ1486. In this fitting, we allow the peak fluxes of three Gaussians and the widths of the narrow and broad lines to vary as free parameters, where we require the line widths of narrow [N IV]λ1483 and N IV]λ1486 to be the same. The fitting results are presented in Section 3.2. This model can well reproduce the observed N IV] profile with a reduced chi-square (χ^2_ν) value of 0.7 and a BIC of 49.

If we fit the N IV] profile by adding a second broad component with centroid fixed at the rest-frame wavelength of [N IV] λ1483, we will find a similar result ($\chi^2_\nu = 0.7$, BIC = 52). The derived broad [N IV] λ1483 line flux is negligible, and hence we place a 3σ limiting flux of $< 2.0 \times 10^{-19}$ erg s^{-1} cm^{-2}. This indicates a large N IV] λ1486/[N IV] λ1483 flux ratio to the broad line (> 3.0).

We also consider whether the N IV] profile of GN-z11 can be fitted by two narrow Gaussians only. With this model, we derive a χ^2_ν of 1.2 and a BIC of 66, both larger than that of fitting with a broad component. Notably, the difference between BIC values of these two fits is significant (ΔBIC = 17), indicating that the model including a broad component indeed provides a better fit to the N IV] profile. The N IV]/[N IV] flux ratio inferred from two narrow Gaussian model fitting is 8.2, consistent with that inferred from fitting with models including both narrow and broad Gaussians.

We consider whether the N III] multiplet profile shows a broad component. We simultaneously fit N III] with five narrow Gaussians and a broad Gaussian, where we fix the line width of the broad component to that of the broad N IV] (FWHM = 1670 km s^{-1}). This fit is statistically marginally worse than fitting with five narrow Gaussian model, with a larger BIC (ΔBIC = 4). The inferred broad N III] component has SNR < 3. The

[17] http://www.astropy.org

fitted N III]λ1750/N III]λ1752 ratio is similar to the narrow Gaussian fit, with $1.7^{+0.4}_{-0.4}$.

Given the presence of a broad N IV], we examine whether there is a broad component in C III] as well. To do so, we fit the C III] profile with two different models: a combination of two narrow Gaussians (centered on the rest-frame wavelengths of [C III]λ1907 and C III]λ1909), and a combination of two narrow Gaussians and two broad Gaussians. In the latter model, we fix the line width of each broad component to be the same as the broad N IV] (FWHM = 1670 km s^{-1}). We then perform the same BIC and reduced chi-square test as for N IV]. When fitting the C III] profile with two narrow Gaussians, we find a BIC of 53 and $\chi^2_\nu = 1.0$. By adding broad components, the fitting is almost equal to two narrow Gaussian fitting with ΔBIC = 2 and a similar χ^2_ν (= 0.9). Both the inferred broad [C III] and C III] components have SNRs below 3. This demonstrates that we do not clearly detect a broad component underlying C III].

We similarly test whether there is a broad component in O III]λ1666. We fit the O III]λ1666 profile with two models: a single narrow Gaussian model and a combination of a narrow and a broad Gaussian, where the line width of the broad Gaussian is fixed to that of the broad N IV]. We then perform the BIC test for O III]. There is no significant difference between fitting O III] with both models (ΔBIC = 1), suggesting that there is no clear broad component underlying O III].

B. ADDITIONAL STELLAR CONTINUUM FITTING MODELS

We present the additional stellar continuum fitting models discussed in § 6.4. In Figure B1, we show the continuum fit based on the M25$_{\dot{\rm M},\rm LMC}$ models, assuming the fiducial low metallicity (0.04 $Z_\odot$) and small ionized bubble size (0.5 pMPc). In Figures B2 and B3, we show also the best-fit model with the CB19 models (0.1 and 0.2 $Z_\odot$) at higher metallicities than our fiducial value, though we consider such high metallicities are unlikely for GN-z11 (see § 6.2). In Figures B4 and B5, we show the best-fit model without very massive stars (i.e., assuming an IMF upper mass cutoff of 100 $M_\odot$) based on the CB19 and BPASS SSP models, respectively. For both models, the fit to N V is worse than the models including very massive stars (Figure 16 and 17), underpredicting the P-Cygni emission components.

REFERENCES

Adamo, A., Bradley, L. D., Vanzella, E., et al. 2024, Nature, 632, 513, doi: 10.1038/s41586-024-07703-7

Adams, N. J., Conselice, C. J., Ferreira, L., et al. 2023, MNRAS, 518, 4755, doi: 10.1093/mnras/stac3347

Álvarez-Márquez, J., Crespo Gómez, A., Colina, L., et al. 2025, A&A, 695, A250, doi: 10.1051/0004-6361/202451731

Asplund, M., Amarsi, A. M., & Grevesse, N. 2021, A&A, 653, A141, doi: 10.1051/0004-6361/202140445

Astropy Collaboration, Robitaille, T. P., Tollerud, E. J., et al. 2013, A&A, 558, A33, doi: 10.1051/0004-6361/201322068

Astropy Collaboration, Price-Whelan, A. M., Sipőcz, B. M., et al. 2018, AJ, 156, 123, doi: 10.3847/1538-3881/aabc4f

Astropy Collaboration, Price-Whelan, A. M., Lim, P. L., et al. 2022, apj, 935, 167, doi: 10.3847/1538-4357/ac7c74

Baldwin, J. A., Hamann, F., Korista, K. T., et al. 2003, The Astrophysical Journal, 583, 649, doi: 10.1086/345449

Bentz, M. C., Denney, K. D., Grier, C. J., et al. 2013, ApJ, 767, 149, doi: 10.1088/0004-637X/767/2/149

Berg, D. A., Chisholm, J., Erb, D. K., et al. 2021, ApJ, 922, 170, doi: 10.3847/1538-4357/ac141b

Berg, D. A., James, B. L., King, T., et al. 2022, ApJS, 261, 31, doi: 10.3847/1538-4365/ac6c03

Berg, D. A., Naidu, R. P., Chisholm, J., et al. 2026, ApJ, 1003, 112, doi: 10.3847/1538-4357/ae5e4c

Bolan, P., Lemaux, B. C., Mason, C., et al. 2022, MNRAS, 517, 3263, doi: 10.1093/mnras/stac1963

Bouwens, R. J., Illingworth, G. D., Oesch, P. A., et al. 2015, ApJ, 803, 34, doi: 10.1088/0004-637X/803/1/34

Bouwens, R. J., Oesch, P. A., Stefanon, M., et al. 2021, AJ, 162, 47, doi: 10.3847/1538-3881/abf83e

Bowler, R. A. A., Jarvis, M. J., Dunlop, J. S., et al. 2020, MNRAS, 493, 2059, doi: 10.1093/mnras/staa313

Boyett, K., Trenti, M., Leethochawalit, N., et al. 2024, Nature Astronomy, 8, 657, doi: 10.1038/s41550-024-02218-7

Brammer, G. 2023, msaexp: NIRSpec analyis tools, 0.9.18 Zenodo, doi: 10.5281/zenodo.7299500

Brinchmann, J., Pettini, M., & Charlot, S. 2008, MNRAS, 385, 769, doi: 10.1111/j.1365-2966.2008.12914.x

Bruton, S., Lin, Y.-H., Scarlata, C., & Hayes, M. J. 2023, ApJL, 949, L40, doi: 10.3847/2041-8213/acd5d0

Bruzual, G., & Charlot, S. 2003, MNRAS, 344, 1000, doi: 10.1046/j.1365-8711.2003.06897.x

Bunker, A. J., Saxena, A., Cameron, A. J., et al. 2023, A&A, 677, A88, doi: 10.1051/0004-6361/202346159

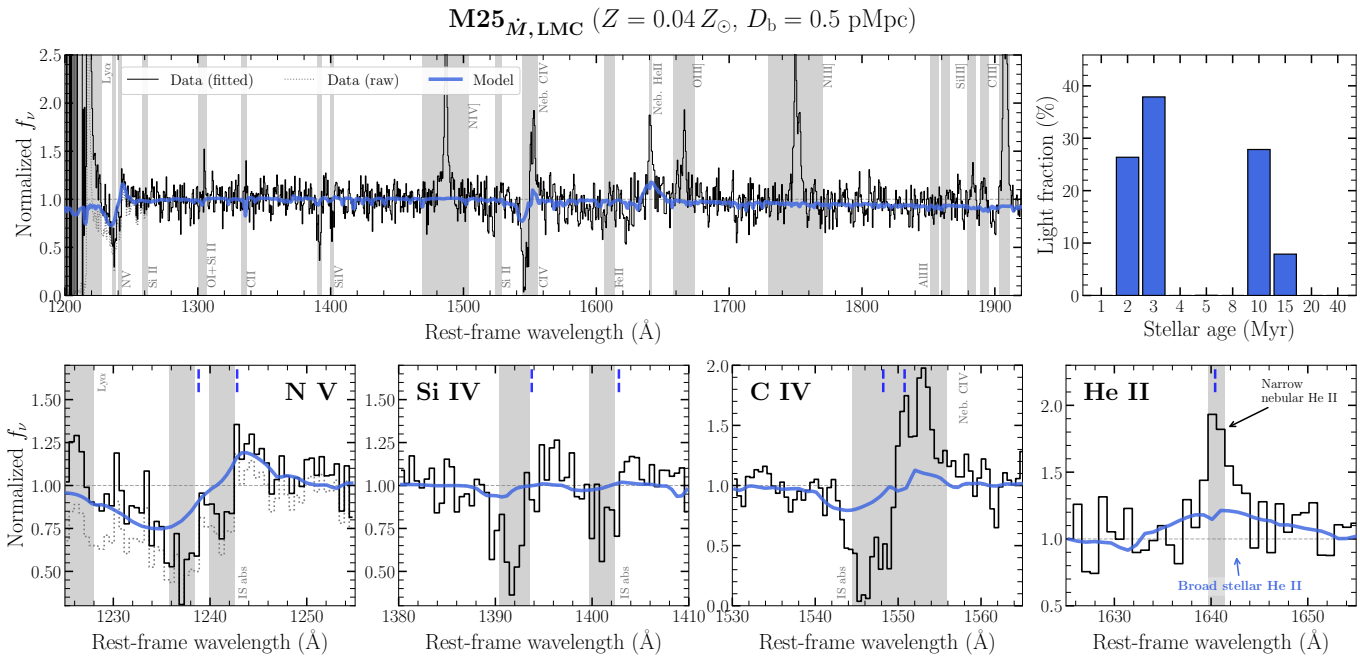

Figure B1. FiCUS fit to the UV continuum of GN-z11 using linear combinations of M25$_{\dot{\mathrm{M}},\mathrm{LMC}}$ SSP models, assuming the fiducial low metallicity (0.04 $Z_\odot$) and a smaller ionized bubble ($D_b = 0.5$ pMpc). As in Figure 16, we show the fit to the full UV continuum (**Top left**), the best-fit star formation history (**Top right**), and zoomed-in views of the N V, Si IV, C IV, and He II regions (**Bottom** panels).

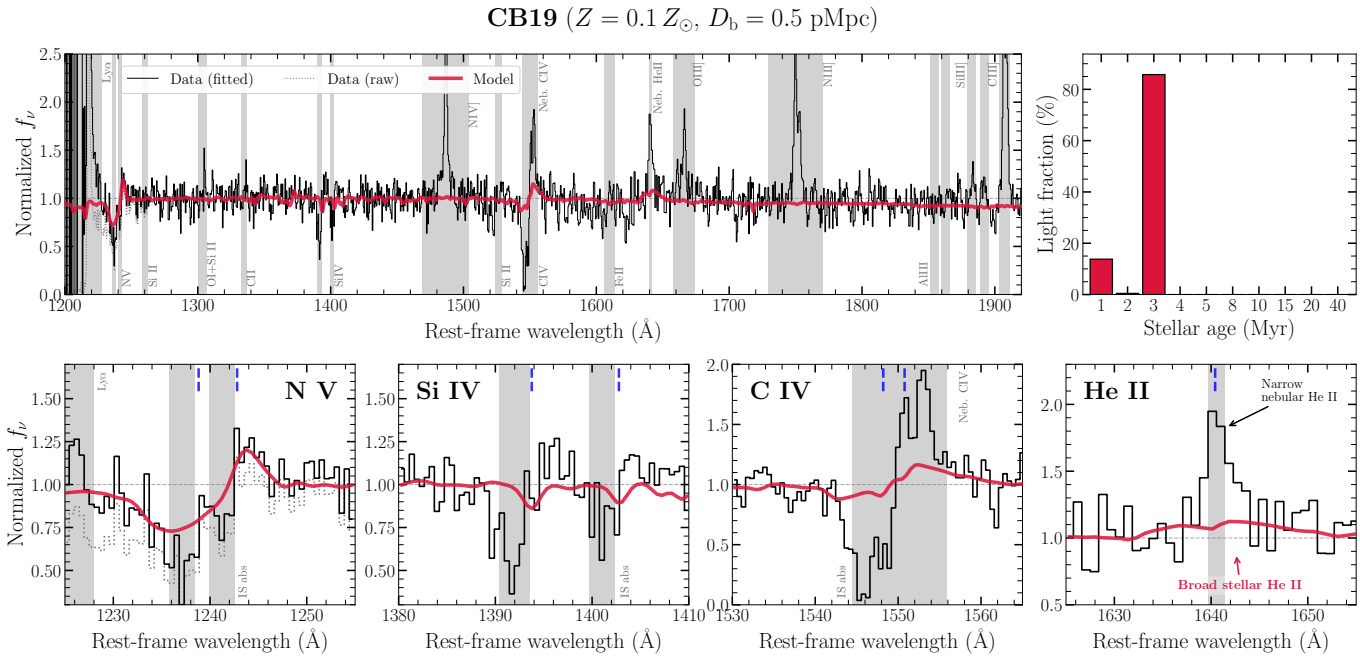

Figure B2. FiCUS fit to the UV continuum of GN-z11 using linear combinations of CB19 SSP models with a higher metallicity of 0.1 $Z_\odot$ than the fiducial CB19 model in Figure 16, plotted in the same format. Such a high stellar metallicity is 2.5× higher than what we expect, and we consider it unlikely.

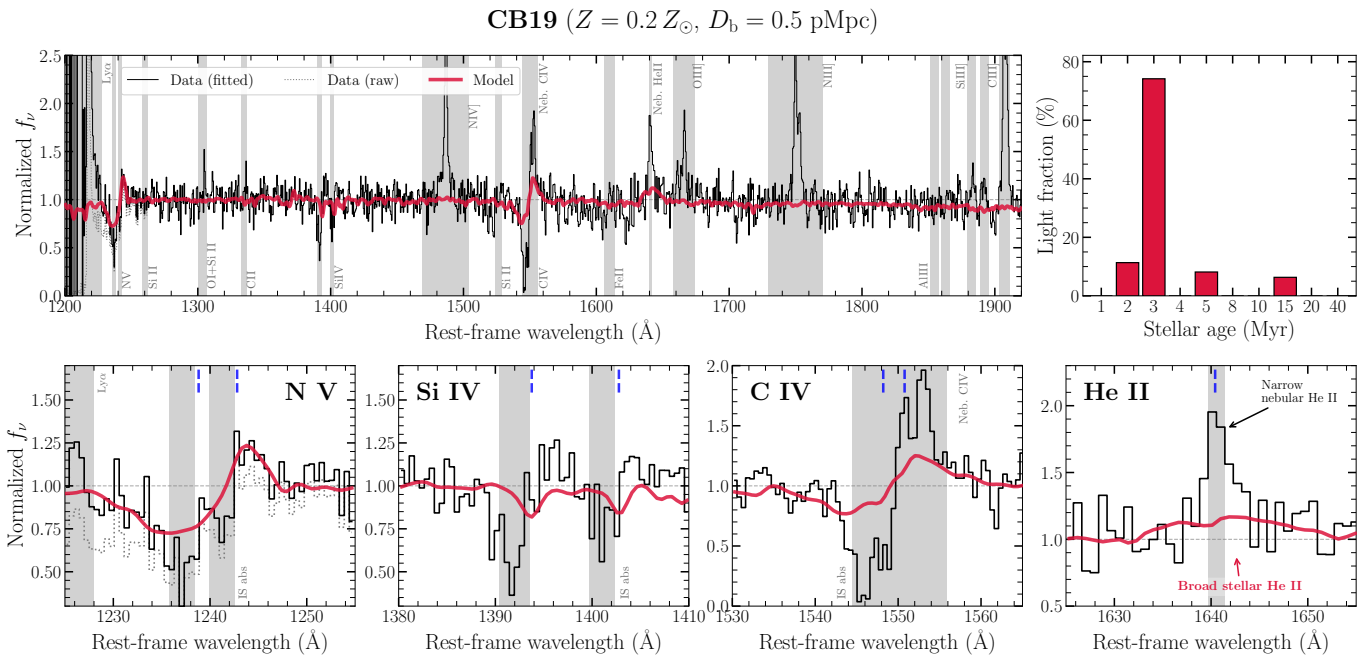

Figure B3. FiCUS fit to the UV continuum of GN-z11 using linear combinations of CB19 SSP models with a higher metallicity of 0.2 $Z_\odot$ than the fiducial CB19 model in Figure 16, plotted in the same format. As in Figure 16, we show the fit to the full UV continuum (**Top left**), the best-fit star formation history (**Top right**), and zoomed-in views of the N V, Si IV, C IV, and He II regions (**Bottom** panels). However, we note such a high stellar metallicity is unlikely.

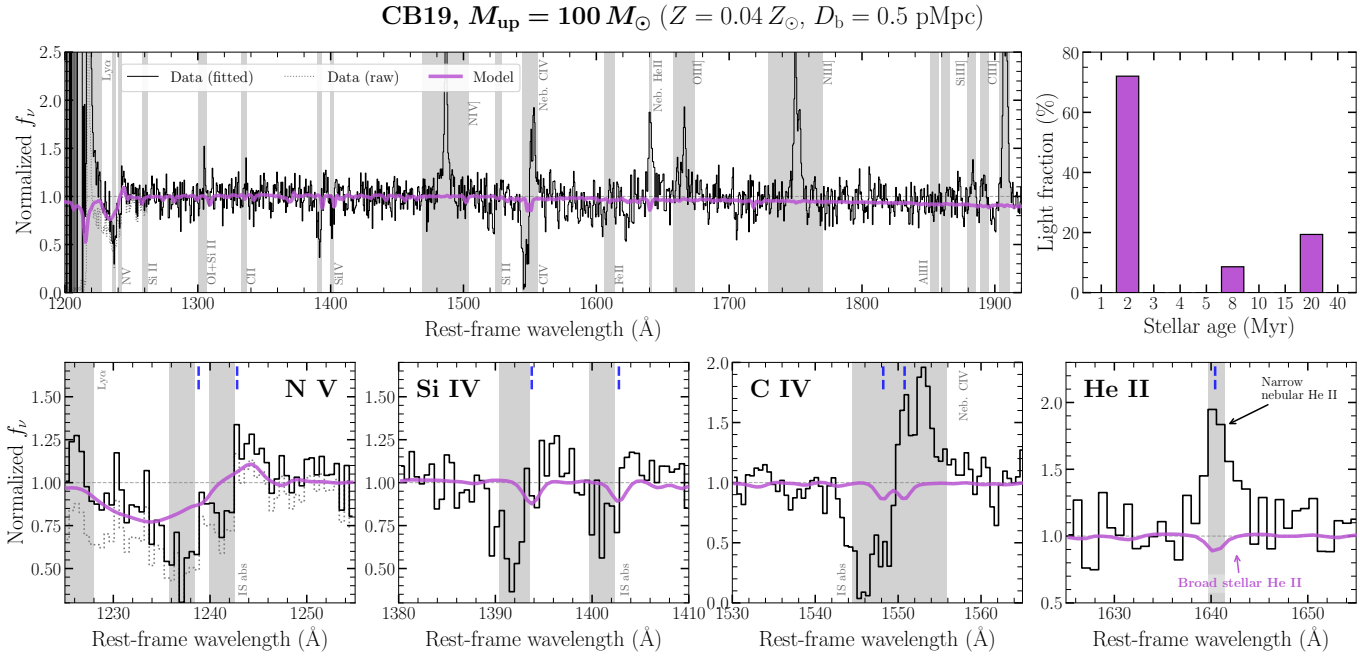

Figure B4. FiCUS fit to the UV continuum of GN-z11 using linear combinations of CB19 SSP models with an upper mass cutoff of 100 $M_\odot$, plotted in the same format as Figure 16. For the fiducial low metallicity (0.04 $Z_\odot$) and a small ionized bubble ($D_b = 0.5$ pMpc), the model underpredicts the P-Cygni emission components compared to the CB19 models that include very massive stars (Figure 16).

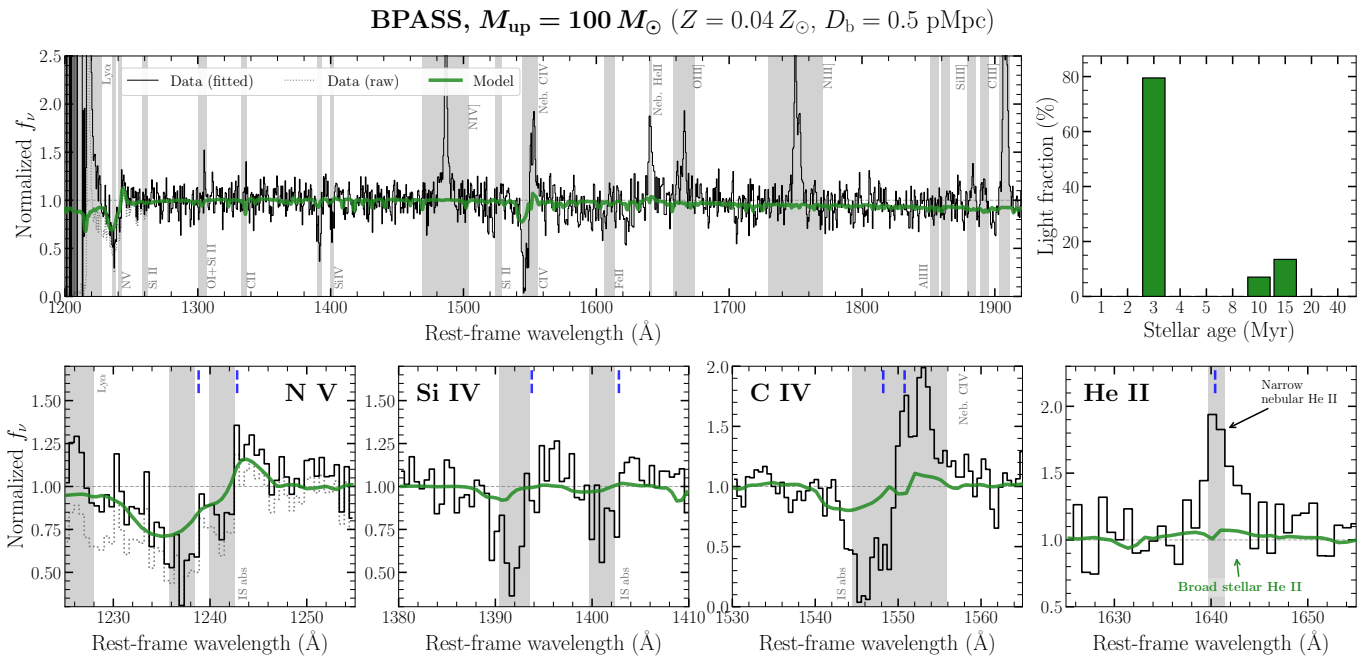

Figure B5. FiCUS fit to the UV continuum of GN-z11 using linear combinations of BPASS SSP models with an upper mass cutoff of 100 $M_\odot$, plotted in the same format as Figure B4. Compared to the M25 models that include very massive stars (Figure 17), this model underpredicts the P-Cygni emission component for the fiducial low metallicity (0.04 $Z_\odot$) and a small ionized bubble ($D_b = 0.5$ pMpc).

Cain, C., Lopez, G., D'Aloisio, A., et al. 2025, ApJ, 980, 83, doi: 10.3847/1538-4357/ada152

Cameron, A. J., Katz, H., Rey, M. P., & Saxena, A. 2023, MNRAS, 523, 3516, doi: 10.1093/mnras/stad1579

Campbell, A., Terlevich, R., & Melnick, J. 1986, MNRAS, 223, 811, doi: 10.1093/mnras/223.4.811

Carniani, S., Hainline, K., D'Eugenio, F., et al. 2024, Nature, 633, 318, doi: 10.1038/s41586-024-07860-9

Castellano, M., Fontana, A., Treu, T., et al. 2022, ApJL, 938, L15, doi: 10.3847/2041-8213/ac94d0

Castellano, M., Napolitano, L., Fontana, A., et al. 2024, ApJ, 972, 143, doi: 10.3847/1538-4357/ad5f88

Chabrier, G. 2003, PASP, 115, 763, doi: 10.1086/376392

Chandar, R., Leitherer, C., & Tremonti, C. A. 2004, ApJ, 604, 153, doi: 10.1086/381723

Chang, S.-J., & Gronke, M. 2024, MNRAS, 532, 3526, doi: 10.1093/mnras/stae1664

Charbonnel, C., Schaerer, D., Prantzos, N., et al. 2023, A&A, 673, L7, doi: 10.1051/0004-6361/202346410

Chen, Y., Bressan, A., Girardi, L., et al. 2015, MNRAS, 452, 1068, doi: 10.1093/mnras/stv1281

Chen, Z., Stark, D. P., Mason, C. A., et al. 2026, arXiv e-prints, arXiv:2604.21516, doi: 10.48550/arXiv.2604.21516

Chevallard, J., & Charlot, S. 2016, MNRAS, 462, 1415, doi: 10.1093/mnras/stw1756

Chisholm, J., Prochaska, J. X., Schaerer, D., Gazagnes, S., & Henry, A. 2020, MNRAS, 498, 2554, doi: 10.1093/mnras/staa2470

Chisholm, J., Rigby, J. R., Bayliss, M., et al. 2019, ApJ, 882, 182, doi: 10.3847/1538-4357/ab3104

Chisholm, J., Tremonti, C. A., Leitherer, C., et al. 2015, ApJ, 811, 149, doi: 10.1088/0004-637X/811/2/149

Chisholm, J., Berg, D. A., Boylan-Kolchin, M., et al. 2026, The Astrophysical Journal Letters, 1004, L4, doi: 10.3847/2041-8213/ae6dae

Choe, S., Emil Rivera-Thorsen, T., Dahle, H., et al. 2025, A&A, 698, A16, doi: 10.1051/0004-6361/202450685

Chon, S., Ono, H., Omukai, K., & Schneider, R. 2022, MNRAS, 514, 4639, doi: 10.1093/mnras/stac1549

Christensen, L., Richard, J., Hjorth, J., et al. 2012, MNRAS, 427, 1953, doi: 10.1111/j.1365-2966.2012.22006.x

Cohon, J., Cain, C., Windhorst, R., et al. 2026, PASA, 43, e046, doi: 10.1017/pasa.2026.10166

Crespo Gómez, A., Colina, L., Pérez-González, P. G., et al. 2026, A&A, 706, A46, doi: 10.1051/0004-6361/202556814

Crowther, P. A. 2007, ARA&A, 45, 177, doi: 10.1146/annurev.astro.45.051806.110615

Crowther, P. A., & Smith, L. J. 1997, Astronomy and Astrophysics, 320, 500

Crowther, P. A., Smith, L. J., & Hillier, D. J. 1995, Astronomy and Astrophysics, 302, 457

Crowther, P. A., Caballero-Nieves, S. M., Bostroem, K. A., et al. 2016, MNRAS, 458, 624, doi: 10.1093/mnras/stw273

de Graaff, A., Rix, H.-W., Carniani, S., et al. 2024, A&A, 684, A87, doi: 10.1051/0004-6361/202347755

de Graaff, A., Brammer, G., Weibel, A., et al. 2025, A&A, 697, A189, doi: 10.1051/0004-6361/202452186

Dekel, A., Sarkar, K. C., Birnboim, Y., Mandelker, N., & Li, Z. 2023, MNRAS, 523, 3201, doi: 10.1093/mnras/stad1557

Dijkstra, M., Mesinger, A., & Wyithe, J. S. B. 2011, MNRAS, 414, 2139, doi: 10.1111/j.1365-2966.2011.18530.x

Donnan, C. T., McLure, R. J., Dunlop, J. S., et al. 2024, MNRAS, 533, 3222, doi: 10.1093/mnras/stae2037

Donnan, C. T., McLeod, D. J., McLure, R. J., et al. 2026, doi: 10.48550/ARXIV.2601.11515

Drissen, L., Crowther, P. A., Smith, L. J., et al. 2001, The Astrophysical Journal, Volume 546, Issue 1, pp. 484-495., 546, 484, doi: 10.1086/318264

Du, X., Shapley, A. E., Reddy, N. A., et al. 2018, ApJ, 860, 75, doi: 10.3847/1538-4357/aabfcf

Eldridge, J. J., Stanway, E. R., Xiao, L., et al. 2017, PASA, 34, e058, doi: 10.1017/pasa.2017.51

Ellis, R. S. 2025, Galaxies and Black Holes in the First Billion Years, arXiv, doi: 10.48550/ARXIV.2508.16948

Endsley, R., & Stark, D. P. 2022, MNRAS, 511, 6042, doi: 10.1093/mnras/stac524

Endsley, R., Stark, D. P., Bouwens, R. J., et al. 2022, MNRAS, 517, 5642, doi: 10.1093/mnras/stac3064

Erb, D. K., Quider, A. M., Henry, A. L., & Martin, C. L. 2012, ApJ, 759, 26, doi: 10.1088/0004-637X/759/1/26

Feldmann, R., Boylan-Kolchin, M., Bullock, J. S., et al. 2025, MNRAS, 536, 988, doi: 10.1093/mnras/stae2633

Ferrara, A., Pallottini, A., & Sommovigo, L. 2025, A&A, 694, A286, doi: 10.1051/0004-6361/202452707

Finkelstein, S. L., Ryan, Jr., R. E., Papovich, C., et al. 2015, ApJ, 810, 71, doi: 10.1088/0004-637X/810/1/71

Finkelstein, S. L., Bagley, M. B., Ferguson, H. C., et al. 2023, ApJL, 946, L13, doi: 10.3847/2041-8213/acade4

Foreman-Mackey, D., Hogg, D. W., Lang, D., & Goodman, J. 2013, PASP, 125, 306, doi: 10.1086/670067

Freitag, M., Gürkan, M. A., & Rasio, F. A. 2006, MNRAS, 368, 141, doi: 10.1111/j.1365-2966.2006.10096.x

Froese Fischer, C., & Saha, H. P. 1985, PhyS, 32, 181, doi: 10.1088/0031-8949/32/3/004

Fujii, M. S., & Portegies Zwart, S. 2013, MNRAS, 430, 1018, doi: 10.1093/mnras/sts673

Gagnon-Hartman, S., Mesinger, A., Nikolić, I., Parlanti, E., & Venturi, G. 2026, arXiv e-prints, arXiv:2602.13389, doi: 10.48550/arXiv.2602.13389

Gallagher, J. S. 1989, in Astrophysics and Space Science Library, Vol. 157, IAU Colloquium 113: Physics of Luminous Blue Variables, ed. K. Davidson, A. F. J. Moffat, & H. J. G. L. M. Lamers, 185, doi: 10.1007/978-94-009-1031-7_22

Gardner, J. P., Mather, J. C., Abbott, R., et al. 2023, PASP, 135, 068001, doi: 10.1088/1538-3873/acd1b5

Gelli, V., Mason, C., & Hayward, C. C. 2024, ApJ, 975, 192, doi: 10.3847/1538-4357/ad7b36

Georgiev, L., Koenigsberger, G., Hillier, D. J., et al. 2011, The Astronomical Journal, 142, 191, doi: 10.1088/0004-6256/142/6/191

Gieles, M., Padoan, P., Charbonnel, C., Vink, J. S., & Ramírez-Galeano, L. 2025, MNRAS, 544, 483, doi: 10.1093/mnras/staf1314

Glazer, K. S., Jones, T., Chen, Y., et al. 2025, ApJ, 992, 191, doi: 10.3847/1538-4357/ae0194

Gordon, K. D., Clayton, G. C., Misselt, K. A., Landolt, A. U., & Wolff, M. J. 2003, ApJ, 594, 279, doi: 10.1086/376774

Goswami, S., Umbreit, S., Bierbaum, M., & Rasio, F. A. 2012, ApJ, 752, 43, doi: 10.1088/0004-637X/752/1/43

Gräfener, G. 2021, A&A, 647, A13, doi: 10.1051/0004-6361/202040037

GRAVITY Collaboration, Amorim, A., Bourdarot, G., et al. 2024, A&A, 684, A167, doi: 10.1051/0004-6361/202348167

Gräfener, G., Koesterke, L., & Hamann, W. R. 2002, A&A, 387, 244, doi: 10.1051/0004-6361:20020269

Gutkin, J., Charlot, S., & Bruzual, G. 2016, MNRAS, 462, 1757, doi: 10.1093/mnras/stw1716

Hainich, R., Pasemann, D., Todt, H., et al. 2015, A&A, 581, A21, doi: 10.1051/0004-6361/201526241

Hainich, R., Rühling, U., Todt, H., et al. 2014, A&A, 565, A27, doi: 10.1051/0004-6361/201322696

Hainline, K. N., Shapley, A. E., Greene, J. E., & Steidel, C. C. 2011, ApJ, 733, 31, doi: 10.1088/0004-637X/733/1/31

Hamann, W.-R., & Gräfener, G. 2004, Astronomy and Astrophysics, 427, 697, doi: 10.1051/0004-6361:20040506

Harikane, Y., Ouchi, M., Oguri, M., et al. 2023a, ApJS, 265, 5, doi: 10.3847/1538-4365/acaaa9

Harikane, Y., Zhang, Y., Nakajima, K., et al. 2023b, ApJ, 959, 39, doi: 10.3847/1538-4357/ad029e

Harris, C. R., Millman, K. J., van der Walt, S. J., et al. 2020, Nature, 585, 357, doi: 10.1038/s41586-020-2649-2

Hayes, M. J., Runnholm, A., Gronke, M., & Scarlata, C. 2021, ApJ, 908, 36, doi: 10.3847/1538-4357/abd246
Heckman, T. M., & Borthakur, S. 2016, ApJ, 822, 9, doi: 10.3847/0004-637X/822/1/9
Hegde, S., Wyatt, M. M., & Furlanetto, S. R. 2024, JCAP, 2024, 025, doi: 10.1088/1475-7516/2024/08/025
Heintz, K. E., Brammer, G. B., Watson, D., et al. 2025, A&A, 693, A60, doi: 10.1051/0004-6361/202450243
Henry, A., Berg, D. A., Scarlata, C., Verhamme, A., & Erb, D. 2018, ApJ, 855, 96, doi: 10.3847/1538-4357/aab099
Hillier, D. J. 1988, ApJ, 327, 822, doi: 10.1086/166240
Hillier, D. J. 1989, ApJ, 347, 392, doi: 10.1086/168127
Hillier, D. J., & Miller, D. L. 1998, ApJ, 496, 407, doi: 10.1086/305350
Hunter, J. D. 2007, Computing in Science & Engineering, 9, 90, doi: 10.1109/MCSE.2007.55
Hutter, A., Cueto, E. R., Dayal, P., et al. 2025, A&A, 694, A254, doi: 10.1051/0004-6361/202452460
Inayoshi, K., Visbal, E., & Haiman, Z. 2020, ARA&A, 58, 27, doi: 10.1146/annurev-astro-120419-014455
Isobe, Y., Ouchi, M., Tominaga, N., et al. 2023, ApJ, 959, 100, doi: 10.3847/1538-4357/ad09be
Izotov, Y. I., Stasińska, G., Meynet, G., Guseva, N. G., & Thuan, T. X. 2006, A&A, 448, 955, doi: 10.1051/0004-6361:20053763
James, B. L., Pettini, M., Christensen, L., et al. 2014, MNRAS, 440, 1794, doi: 10.1093/mnras/stu287
Ji, X., Übler, H., Maiolino, R., et al. 2024, MNRAS, 535, 881, doi: 10.1093/mnras/stae2375
Ji, X., Maiolino, R., Ferland, G., et al. 2025, MNRAS, 541, 2134, doi: 10.1093/mnras/staf1083
Ji, X., Pezzulli, G., D'Eugenio, F., et al. 2026, arXiv e-prints, arXiv:2604.03370, doi: 10.48550/arXiv.2604.03370
Jiang, L., Fan, X., & Vestergaard, M. 2008, The Astrophysical Journal, 679, 962, doi: 10.1086/587868
Jones, T. A., Ellis, R. S., Schenker, M. A., & Stark, D. P. 2013, ApJ, 779, 52, doi: 10.1088/0004-637X/779/1/52
Jung, I., Finkelstein, S. L., Dickinson, M., et al. 2020, ApJ, 904, 144, doi: 10.3847/1538-4357/abbd44
Justham, S., Podsiadlowski, P., & Vink, J. S. 2014, ApJ, 796, 121, doi: 10.1088/0004-637X/796/2/121
Kageura, Y., Ouchi, M., Nakane, M., et al. 2025, ApJS, 278, 33, doi: 10.3847/1538-4365/adc690
Kaspi, S., Maoz, D., Netzer, H., et al. 2005, The Astrophysical Journal, Volume 629, Issue 1, pp. 61-71., 629, 61, doi: 10.1086/431275
Katz, H., Cameron, A. J., Saxena, A., et al. 2025, The Open Journal of Astrophysics, 8, 104, doi: 10.33232/001c.142570
Keating, L. C., Bolton, J. S., Cullen, F., et al. 2024, MNRAS, 532, 1646, doi: 10.1093/mnras/stae1530
Kewley, L. J., Nicholls, D. C., & Sutherland, R. S. 2019, ARA&A, 57, 511, doi: 10.1146/annurev-astro-081817-051832
Kluyver, T., Ragan-Kelley, B., Pérez, F., et al. 2016, in IOS Press, 87–90, doi: 10.3233/978-1-61499-649-1-87
Kobayashi, C., & Ferrara, A. 2024, ApJL, 962, L6, doi: 10.3847/2041-8213/ad1de1
Koenigsberger, G., Georgiev, L., Hillier, D. J., et al. 2010, The Astronomical Journal, 139, 2600, doi: 10.1088/0004-6256/139/6/2600
Koenigsberger, G., Guinan, E., Auer, L., & Georgiev, L. 1995, ApJL, 452, L107, doi: 10.1086/309719
Koenigsberger, G., Moffat, A. F. J., St-Louis, N., et al. 1994, The Astrophysical Journal, 436, 301, doi: 10.1086/174905
Koenigsberger, G., & Moreno, E. 1997, Luminous Blue Variables: Massive Stars in Transition, 120, 233
Koenigsberger, G., Morrell, N., Hillier, D. J., et al. 2014, The Astronomical Journal, Volume 148, Issue 4, article id. 62, <NUMPAGES>13</NUMPAGES> pp. (2014)., 148, 62, doi: 10.1088/0004-6256/148/4/62
Köhler, K., Langer, N., de Koter, A., et al. 2015, Astronomy and Astrophysics, 573, A71, doi: 10.1051/0004-6361/201424356
Kokorev, V., Chisholm, J., Naidu, R. P., et al. 2026, ApJ, 1004, 153, doi: 10.3847/1538-4357/ae4ed7
Kornei, K. A., Shapley, A. E., Martin, C. L., et al. 2013, ApJ, 774, 50, doi: 10.1088/0004-637X/774/1/50
Kravtsov, A., & Belokurov, V. 2024, arXiv e-prints, arXiv:2405.04578, doi: 10.48550/arXiv.2405.04578
Kwan, J., & Krolik, J. H. 1981, ApJ, 250, 478, doi: 10.1086/159395
Labbe, I., Greene, J. E., Matthee, J., et al. 2024, arXiv e-prints, arXiv:2412.04557, doi: 10.48550/arXiv.2412.04557
Lambrides, E., Larson, R. L., Garofali, K., et al. 2026, Nature Astronomy, 10, 868, doi: 10.1038/s41550-026-02813-w
Larson, R. L., Finkelstein, S. L., Kocevski, D. D., et al. 2023, ApJL, 953, L29, doi: 10.3847/2041-8213/ace619
Law, D. R., Argyriou, I., Gordon, K. D., et al. 2025, AJ, 169, 67, doi: 10.3847/1538-3881/ad9685
Leitherer, C., Ortiz Otálvaro, P. A., Bresolin, F., et al. 2010, ApJS, 189, 309, doi: 10.1088/0067-0049/189/2/309
Leitherer, C., Robert, C., & Heckman, T. M. 1995, ApJS, 99, 173, doi: 10.1086/192183
Leitherer, C., Tremonti, C. A., Heckman, T. M., & Calzetti, D. 2011, AJ, 141, 37, doi: 10.1088/0004-6256/141/2/37

Liddle, A. R. 2007, MNRAS, 377, L74, doi: 10.1111/j.1745-3933.2007.00306.x
Lu, T.-Y., Mason, C. A., Hutter, A., et al. 2024, MNRAS, 528, 4872, doi: 10.1093/mnras/stae266
Luridiana, V., Morisset, C., & Shaw, R. A. 2015, A&A, 573, A42, doi: 10.1051/0004-6361/201323152
Mainali, R., Stark, D. P., Jones, T., et al. 2023, MNRAS, 520, 4037, doi: 10.1093/mnras/stad387
Maiolino, R., Scholtz, J., Witstok, J., et al. 2024, Nature, 627, 59, doi: 10.1038/s41586-024-07052-5
Marques-Chaves, R., Schaerer, D., Kuruvanthodi, A., et al. 2024, A&A, 681, A30, doi: 10.1051/0004-6361/202347411
Martinez, Z., Berg, D. A., James, B. L., et al. 2025, ApJ, 995, 204, doi: 10.3847/1538-4357/ae17c6
Martins, F., & Palacios, A. 2022, A&A, 659, A163, doi: 10.1051/0004-6361/202243048
Martins, F., Palacios, A., Schaerer, D., & Marques-Chaves, R. 2025, A&A, 698, A262, doi: 10.1051/0004-6361/202554421
Maryeva, O., Viotti, R. F., Koenigsberger, G., et al. 2019, Galaxies, 7, 79, doi: 10.3390/galaxies7030079
Maseda, M. V., Brinchmann, J., Franx, M., et al. 2017, A&A, 608, A4, doi: 10.1051/0004-6361/201730985
Mason, C. A., Chen, Z., Stark, D. P., et al. 2026, A&A, 705, A114, doi: 10.1051/0004-6361/202553820
Mason, C. A., & Gronke, M. 2020, MNRAS, 499, 1395, doi: 10.1093/mnras/staa2910
Mason, C. A., Trenti, M., & Treu, T. 2023, MNRAS, 521, 497, doi: 10.1093/mnras/stad035
Mason, C. A., Treu, T., Dijkstra, M., et al. 2018a, ApJ, 856, 2, doi: 10.3847/1538-4357/aab0a7
Mason, C. A., Treu, T., de Barros, S., et al. 2018b, ApJL, 857, L11, doi: 10.3847/2041-8213/aabbab
Matsuoka, K., Nagao, T., Maiolino, R., et al. 2017, Astronomy and Astrophysics, 608, A90, doi: 10.1051/0004-6361/201629878
Matsuoka, Y., Oyabu, S., Tsuzuki, Y., & Kawara, K. 2007, ApJ, 663, 781, doi: 10.1086/518399
Matthee, J. 2025, Contemporary Physics, 66, 116, doi: 10.1080/00107514.2025.2586370
McClymont, W., Tacchella, S., Smith, A., et al. 2026, MNRAS, 548, stag016, doi: 10.1093/mnras/stag016
McQuinn, M., Lidz, A., Zahn, O., et al. 2007, MNRAS, 377, 1043, doi: 10.1111/j.1365-2966.2007.11489.x
McQuinn, M., Lidz, A., Zaldarriaga, M., Hernquist, L., & Dutta, S. 2008, MNRAS, 388, 1101, doi: 10.1111/j.1365-2966.2008.13271.x
Mesinger, A., & Furlanetto, S. R. 2008, MNRAS, 385, 1348, doi: 10.1111/j.1365-2966.2007.12836.x
Mingozzi, M., James, B. L., Arellano-Córdova, K. Z., et al. 2022, ApJ, 939, 110, doi: 10.3847/1538-4357/ac952c
Miralda-Escudé, J. 1998, ApJ, 501, 15, doi: 10.1086/305799
Mirocha, J., & Furlanetto, S. R. 2023, MNRAS, 519, 843, doi: 10.1093/mnras/stac3578
Moffat, A. F. J., Marchenko, S. V., Bartzakos, P., et al. 1998, The Astrophysical Journal, Volume 497, Issue 2, pp. 896-911., 497, 896, doi: 10.1086/305475
Morel, I., Schaerer, D., Marques-Chaves, R., et al. 2025, arXiv e-prints, arXiv:2511.20484, doi: 10.48550/arXiv.2511.20484
Nagele, C., & Umeda, H. 2023, ApJL, 949, L16, doi: 10.3847/2041-8213/acd550
Naidu, R. P., Oesch, P. A., van Dokkum, P., et al. 2022, ApJL, 940, L14, doi: 10.3847/2041-8213/ac9b22
Naidu, R. P., Oesch, P. A., Brammer, G., et al. 2026, The Open Journal of Astrophysics, 9, 56033, doi: 10.33232/001c.156033
Nanayakkara, T., Brinchmann, J., Boogaard, L., et al. 2019, A&A, 624, A89, doi: 10.1051/0004-6361/201834565
Neufeld, D. A. 1990, ApJ, 350, 216, doi: 10.1086/168375
Newville, M., Stensitzki, T., Allen, D. B., et al. 2016, Lmfit: Non-Linear Least-Square Minimization and Curve-Fitting for Python,, Astrophysics Source Code Library, record ascl:1606.014 http://ascl.net/1606.014
Neyer, M., Smith, A., Kannan, R., et al. 2024, MNRAS, 531, 2943, doi: 10.1093/mnras/stae1325
Nomoto, K., Tominaga, N., Umeda, H., Kobayashi, C., & Maeda, K. 2006, NuPhA, 777, 424, doi: 10.1016/j.nuclphysa.2006.05.008
Oesch, P. A., Bouwens, R. J., Illingworth, G. D., Labbé, I., & Stefanon, M. 2018, ApJ, 855, 105, doi: 10.3847/1538-4357/aab03f
Oesch, P. A., Brammer, G., van Dokkum, P. G., et al. 2016, ApJ, 819, 129, doi: 10.3847/0004-637X/819/2/129
Oke, J. B., & Gunn, J. E. 1983, ApJ, 266, 713, doi: 10.1086/160817
Osterbrock, D. E., & Ferland, G. J. 2006, Astrophysics of gaseous nebulae and active galactic nuclei
Pahl, A. J., Shapley, A., Faisst, A. L., et al. 2020, MNRAS, 493, 3194, doi: 10.1093/mnras/staa355
Park, H., Jung, I., Song, H., et al. 2021, ApJ, 922, 263, doi: 10.3847/1538-4357/ac2f4b
Pascale, M., & Dai, L. 2024, ApJ, 976, 166, doi: 10.3847/1538-4357/ad7732
Pauldrach, A., Puls, J., & Kudritzki, R. P. 1986, A&A, 164, 86
Pei, Y. C. 1992, ApJ, 395, 130, doi: 10.1086/171637
Pentericci, L., Vanzella, E., Fontana, A., et al. 2014, ApJ, 793, 113, doi: 10.1088/0004-637X/793/2/113

Pentericci, L., Vanzella, E., Castellano, M., et al. 2018, A&A, 619, A147, doi: 10.1051/0004-6361/201732465
Pettini, M., Rix, S. A., Steidel, C. C., et al. 2002, ApJ, 569, 742, doi: 10.1086/339355
Pettini, M., Steidel, C. C., Adelberger, K. L., Dickinson, M., & Giavalisco, M. 2000, ApJ, 528, 96, doi: 10.1086/308176
Plat, A., Charlot, S., Bruzual, G., et al. 2019, MNRAS, 490, 978, doi: 10.1093/mnras/stz2616
Portegies Zwart, S. F., & McMillan, S. L. W. 2002, ApJ, 576, 899, doi: 10.1086/341798
Prieto-Lyon, G., Mason, C. A., Strait, V., et al. 2025, arXiv e-prints, arXiv:2509.18302, doi: 10.48550/arXiv.2509.18302
Qin, Y., Balu, S., & Wyithe, J. S. B. 2023, MNRAS, 526, 1324, doi: 10.1093/mnras/stad2448
Qin, Y., & Wyithe, J. S. B. 2025, MNRAS, 538, L16, doi: 10.1093/mnrasl/slaf001
Rantala, A., Naab, T., & Lahén, N. 2024, MNRAS, 531, 3770, doi: 10.1093/mnras/stae1413
Rantala, A., Naab, T., Lahén, N., et al. 2026, MNRAS, 549, stag986, doi: 10.1093/mnras/stag986
Reddy, N. A., Steidel, C. C., Pettini, M., Bogosavljević, M., & Shapley, A. E. 2016, ApJ, 828, 108, doi: 10.3847/0004-637X/828/2/108
Reddy, N. A., Topping, M. W., Shapley, A. E., et al. 2022, ApJ, 926, 31, doi: 10.3847/1538-4357/ac3b4c
Rieke, M., Robertson, B., Tacchella, S., et al. 2023, Data from the JWST Advanced Deep Extragalactic Survey (JADES), STScI/MAST, doi: 10.17909/8tdj-8n28
Rigby, J., Perrin, M., McElwain, M., et al. 2023, PASP, 135, 048001, doi: 10.1088/1538-3873/acb293
Rivero González, J. G., Puls, J., Massey, P., & Najarro, F. 2012, Astronomy and Astrophysics, 543, A95, doi: 10.1051/0004-6361/201218955
Rix, S. A., Pettini, M., Leitherer, C., et al. 2004, ApJ, 615, 98, doi: 10.1086/424031
Robertson, B., Johnson, B. D., Tacchella, S., et al. 2024, ApJ, 970, 31, doi: 10.3847/1538-4357/ad463d
Robertson, B. E., Johnson, B. D., Tacchella, S., et al. 2026, arXiv e-prints, arXiv:2601.15956, doi: 10.48550/arXiv.2601.15956
Runco, J. N., Shapley, A. E., Sanders, R. L., et al. 2021, Monthly Notices of the Royal Astronomical Society, 502, 2600, doi: 10.1093/mnras/stab119
Saldana-Lopez, A., Schaerer, D., Chisholm, J., et al. 2023, MNRAS, 522, 6295, doi: 10.1093/mnras/stad1283
Sander, A., Shenar, T., Hainich, R., et al. 2015, Astronomy and Astrophysics, 577, A13, doi: 10.1051/0004-6361/201425356
Sander, A. A. C., & Vink, J. S. 2020, Monthly Notices of the Royal Astronomical Society, 499, 873, doi: 10.1093/mnras/staa2712
Sanders, R. L., Shapley, A. E., Topping, M. W., Reddy, N. A., & Brammer, G. B. 2024, ApJ, 962, 24, doi: 10.3847/1538-4357/ad15fc
Sanders, R. L., Shapley, A. E., Reddy, N. A., et al. 2020, MNRAS, 491, 1427, doi: 10.1093/mnras/stz3032
Santos, M. R. 2004, MNRAS, 349, 1137, doi: 10.1111/j.1365-2966.2004.07594.x
Schaerer, D. 1996, A&A, 309, 129, doi: 10.48550/arXiv.astro-ph/9509079
Schaerer, D., Marques-Chaves, R., Xiao, M., & Korber, D. 2024, A&A, 687, L11, doi: 10.1051/0004-6361/202450721
Scholtz, J., Witten, C., Laporte, N., et al. 2024, A&A, 687, A283, doi: 10.1051/0004-6361/202347187
Scholtz, J., Maiolino, R., D'Eugenio, F., et al. 2025, A&A, 697, A175, doi: 10.1051/0004-6361/202348804
Schwarz, G. 1978, Annals of Statistics, 6, 461
Senchyna, P., Plat, A., Stark, D. P., et al. 2024, ApJ, 966, 92, doi: 10.3847/1538-4357/ad235e
Senchyna, P., Stark, D. P., Charlot, S., et al. 2021, MNRAS, 503, 6112, doi: 10.1093/mnras/stab884
Senchyna, P., Stark, D. P., Charlot, S., et al. 2022, ApJ, 930, 105, doi: 10.3847/1538-4357/ac5d38
Shajib, A. J., Treu, T., Melo, A., et al. 2025, A&A, 702, L12, doi: 10.1051/0004-6361/202556281
Shapley, A. E., Steidel, C. C., Pettini, M., & Adelberger, K. L. 2003, ApJ, 588, 65, doi: 10.1086/373922
Shen, X., Vogelsberger, M., Boylan-Kolchin, M., Tacchella, S., & Kannan, R. 2023, MNRAS, 525, 3254, doi: 10.1093/mnras/stad2508
Shenar, T., Hainich, R., Todt, H., et al. 2016, A&A, 591, A22, doi: 10.1051/0004-6361/201527916
Shi, Y., Dai, L., Murray, N., et al. 2026, ApJ, 997, 309, doi: 10.3847/1538-4357/ae3150
Smith, L. J., Oey, M. S., Hernandez, S., et al. 2023, ApJ, 958, 194, doi: 10.3847/1538-4357/ad00b4
Smith, N., Gehrz, R. D., Campbell, R., et al. 2011, MNRAS, 418, 1959, doi: 10.1111/j.1365-2966.2011.19614.x
Smith, N., E Andrews, J., Moe, M., et al. 2020, MNRAS, 492, 5897, doi: 10.1093/mnras/staa061
Somerville, R. S., Yung, L. Y. A., Lancaster, L., et al. 2025, MNRAS, 544, 3774, doi: 10.1093/mnras/staf1824
Stark, D. P., Ellis, R. S., Chiu, K., Ouchi, M., & Bunker, A. 2010, MNRAS, 408, 1628, doi: 10.1111/j.1365-2966.2010.17227.x
Stark, D. P., Ellis, R. S., & Ouchi, M. 2011, ApJL, 728, L2, doi: 10.1088/2041-8205/728/1/L2

Stark, D. P., Topping, M. W., Endsley, R., & Tang, M. 2026, in Encyclopedia of Astrophysics, Volume 4, Vol. 4, 453–499, doi: 10.1016/B978-0-443-21439-4.00128-0

Steidel, C. C., Erb, D. K., Shapley, A. E., et al. 2010, ApJ, 717, 289, doi: 10.1088/0004-637X/717/1/289

Steidel, C. C., Strom, A. L., Pettini, M., et al. 2016, ApJ, 826, 159, doi: 10.3847/0004-637X/826/2/159

Steinhardt, C. L., Kokorev, V., Rusakov, V., Garcia, E., & Sneppen, A. 2023, ApJL, 951, L40, doi: 10.3847/2041-8213/acdef6

Szécsi, D., Tramper, F., Kubátová, B., et al. 2025, Low-Metallicity Massive Single Stars with Rotation. III. Source of Ionization and C-IV Emission in I Zw 18, arXiv, doi: 10.48550/arXiv.2506.21442

Tacchella, S., Eisenstein, D. J., Hainline, K., et al. 2023, ApJ, 952, 74, doi: 10.3847/1538-4357/acdbc6

Tang, M., Stark, D. P., Topping, M. W., Mason, C., & Ellis, R. S. 2024a, ApJ, 975, 208, doi: 10.3847/1538-4357/ad7eb7

Tang, M., Stark, D. P., Ellis, R. S., et al. 2024b, MNRAS, 531, 2701, doi: 10.1093/mnras/stae1338

Tang, M., Stark, D. P., Plat, A., et al. 2025, ApJ, 991, 217, doi: 10.3847/1538-4357/adfd57

Tang, M., Stark, D. P., Mason, C. A., et al. 2026, arXiv e-prints, arXiv:2604.03563, doi: 10.48550/arXiv.2604.03563

Todt, H., Sander, A., Hainich, R., et al. 2015, A&A, 579, A75, doi: 10.1051/0004-6361/201526253

Topping, M. W., Shapley, A. E., Reddy, N. A., et al. 2020, MNRAS, 495, 4430, doi: 10.1093/mnras/staa1410

Topping, M. W., Stark, D. P., Endsley, R., et al. 2022, ApJ, 941, 153, doi: 10.3847/1538-4357/aca522

Topping, M. W., Stark, D. P., Senchyna, P., et al. 2024, MNRAS, 529, 3301, doi: 10.1093/mnras/stae682

Topping, M. W., Stark, D. P., Senchyna, P., et al. 2025a, ApJ, 980, 225, doi: 10.3847/1538-4357/ada95c

Topping, M. W., Sanders, R. L., Shapley, A. E., et al. 2025b, MNRAS, 541, 1707, doi: 10.1093/mnras/staf903

Trainor, R. F., Steidel, C. C., Strom, A. L., & Rudie, G. C. 2015, ApJ, 809, 89, doi: 10.1088/0004-637X/809/1/89

Trainor, R. F., Strom, A. L., Steidel, C. C., et al. 2019, ApJ, 887, 85, doi: 10.3847/1538-4357/ab4993

Treu, T., Trenti, M., Stiavelli, M., Auger, M. W., & Bradley, L. D. 2012, ApJ, 747, 27, doi: 10.1088/0004-637X/747/1/27

Tripodi, R., Bradač, M., D'Eugenio, F., et al. 2025a, ApJL, 994, L6, doi: 10.3847/2041-8213/ae13a9

Tripodi, R., Martis, N., Markov, V., et al. 2025b, Nature Communications, 16, 9830, doi: 10.1038/s41467-025-65070-x

Upadhyaya, A., Marques-Chaves, R., Schaerer, D., et al. 2024, A&A, 686, A185, doi: 10.1051/0004-6361/202449184

Valentino, F., Heintz, K. E., Brammer, G., et al. 2025, A&A, 699, A358, doi: 10.1051/0004-6361/202553908

Vanzella, E., Claeyssens, A., Welch, B., et al. 2023, ApJ, 945, 53, doi: 10.3847/1538-4357/acb59a

Vasan G. C., Senchyna, P., Mason, C. A., et al. 2026, arXiv e-prints, arXiv:2606.06609, doi: 10.48550/arXiv.2606.06609

Ventura, E. M., Qin, Y., Balu, S., & Wyithe, J. S. B. 2024, MNRAS, 529, 628, doi: 10.1093/mnras/stae567

Verhamme, A., Schaerer, D., Atek, H., & Tapken, C. 2008, A&A, 491, 89, doi: 10.1051/0004-6361:200809648

Verhamme, A., Schaerer, D., & Maselli, A. 2006, A&A, 460, 397, doi: 10.1051/0004-6361:20065554

Vidal-García, A., Charlot, S., Bruzual, G., & Hubeny, I. 2017, MNRAS, 470, 3532, doi: 10.1093/mnras/stx1324

Vink, J. S. 2012, Eta Carinae and the Supernova Impostors, Astrophysics and Space Science Library, Volume 384. ISBN 978-1-4614-2274-7. Springer Science+Business Media, LLC, 2012, p. 221, 384, 221, doi: 10.1007/978-1-4614-2275-4_10

Vink, J. S. 2023, A&A, 679, L9, doi: 10.1051/0004-6361/202347827

Vink, J. S., de Koter, A., & Lamers, H. J. G. L. M. 2001, A&A, 369, 574, doi: 10.1051/0004-6361:20010127

Vink, J. S., Muijres, L. E., Anthonisse, B., et al. 2011, A&A, 531, A132, doi: 10.1051/0004-6361/201116614

Virtanen, P., Gommers, R., Oliphant, T. E., et al. 2020, Nature Methods, 17, 261, doi: 10.1038/s41592-019-0686-2

Walborn, N. R., Nichols-Bohlin, J., & Panek, R. J. 1985, NASA Reference Publication, 1155

Wang, B., Heckman, T. M., Zhu, G., & Norman, C. A. 2020, ApJ, 894, 149, doi: 10.3847/1538-4357/ab88b4

Weis, K., & Bomans, D. J. 2020, Galaxies, 8, 20, doi: 10.3390/galaxies8010020

Whitler, L., Stark, D. P., Mason, C. A., et al. 2026, MNRAS, 548, stag639, doi: 10.1093/mnras/stag639

Whitler, L., Stark, D. P., Topping, M. W., et al. 2025, ApJ, 992, 63, doi: 10.3847/1538-4357/adfddc

Witstok, J., Jakobsen, P., Maiolino, R., et al. 2025, Nature, 639, 897, doi: 10.1038/s41586-025-08779-5

Witstok, J., Carniani, S., Jakobsen, P., et al. 2026, arXiv e-prints, arXiv:2603.18775, doi: 10.48550/arXiv.2603.18775

Wofford, A., Sixtos, A., Charlot, S., et al. 2023, MNRAS, 523, 3949, doi: 10.1093/mnras/stad1622

Woo, J.-H., Kim, J., Cho, H., & Wang, S. 2026, ApJ, 1003, 123, doi: 10.3847/1538-4357/ae6109

Xu, X., Heckman, T., Henry, A., et al. 2022, ApJ, 933, 222, doi: 10.3847/1538-4357/ac6d56

Xu, X., Henry, A., Heckman, T., et al. 2023, ApJ, 943, 94, doi: 10.3847/1538-4357/aca89a

Xu, Y., Ouchi, M., Yajima, H., et al. 2024, ApJ, 976, 142, doi: 10.3847/1538-4357/ad82dd

Yuan, Y., Martin-Alvarez, S., Haehnelt, M. G., et al. 2025, MNRAS, 542, 762, doi: 10.1093/mnras/staf1252

Zamora, S., Carniani, S., Bertola, E., et al. 2025, arXiv e-prints, arXiv:2512.09022, doi: 10.48550/arXiv.2512.09022